Title
Nanoscale interfacial structure for Novel Opto-electronic and Ion-trapping Devices

Author
Ulin-Avila, Erick

Publication Date
2013

Peer reviewed|Thesis/dissertation

Nanoscale interfacial structure for Novel Opto-electronic and Ion-trapping Devices

by

Erick Ulin-Avila

A dissertation submitted in partial satisfaction of the
requirements for the degree of
Doctor of Philosophy

in

Engineering - Mechanical Engineering

in the

Graduate Division

of the

University of California, Berkeley

Committee in charge:

Professor Xiang Zhang, Chair
Professor Kenneth T. Gustafson
Associate Professor Samuel Mao

Spring 2013

Nanoscale interfacial structure for Novel Opto-electronic and Ion-trapping Devices

Abstract

Nanoscale interfacial structure for Novel Opto-electronic and Ion-trapping Devices

by

Erick Ulin-Avila

Doctor of Philosophy in Engineering - Mechanical Engineering

University of California, Berkeley

Professor Xiang Zhang, Chair

In this dissertation, we present contributions to the nanoscale engineering of electronic and geometrical structure of dielectric-metal interfaces. Such structure is designed to support the interaction of light and matter for useful scientific and technological applications. Among our interests are electromagnetic subwavelength localization, propagation and storage; photonic manipulation, modulation, synchronization and its use in the confinement of atomic systems. The latter is directed towards a new generation of scalable devices for quantum information processing (QIP) and surface science studies.

Plasmonic devices use tightly confined EM excitations in metal-dielectric interfaces to provide for a collective electron "surface" mode. Device applications reported here are vast, from transport in active waveguides, High-Q resonant cavities, and light manipulation with atom-like responses using metamaterials. We attain negative index of refraction for visible wavelengths and design for deep-subwavelength surface states (Tamm and Shockley kind) with graphene-like band crossing (Diabolical or Dirac point). The latter is important for studying light propagation dynamics, plasmon manipulation and surface-related physical and chemical phenomena. Also, for understanding molecular dynamics and developing electron transport applications.

Ultrafast photonic addressing of plasmonic-lenses is attained by controlling time uncertainties using field programmable gate arrays (FPGA) based finite state machines (FSM), phase-locking and clock management techniques to signal multiple electro-optic modulators in synchronized fashion. Implemented to pattern media, but useful as well for controlling the interaction time with atomic systems using ultrashort pulses. Light is modulated by using electro optic modulators at high frequencies allowing for high speeds and throughput, however remaining the bulkiest part of the system.

Electronic structure modulation of graphene is used to conceive an interfacial electro-absorptive device for photonic wave modulation in the telecommunications window, compatible with complementary metal-oxide semiconductors (CMOS) fabrication methods and feasible as a tunable quantum interface. Compared to commercially available light modulators, this electro-absorptive device operates at higher frequencies, fit in smaller footprints

and consume less power. It is also useful for modifying the electronic structure of solid surfaces or optical interfaces due to its thickness and electronic properties.

Nanoscale engineering, information theory and quantum physics meet in an experimental attempt to process and store quantum information for practical purposes, currently challenged by decoherence and noise as technical barriers. In an attempt to understand such obstacles towards the scalable miniaturization of QIP devices, we study the quality of interactions between an ion and its trapping environment by spectroscopically measuring "heating rates". We designed a versatile trap to study surface science aspects by in-situ modifying its surface structure and using additional surface scientific tools to complement results. A massive array of robust quantum optics tools is used for the controlled preparation of an ion's initial state, its manipulation and high fidelity readout of the final state. We reduce the "anomalous" electric field noise from the surface even further by performing cleaning methods on the surface of our trap. Our trap is closer to the limiting Johnson noise than any other trap reported in literature, important not only to the ion trapping community but to the scientific community in general.

Deep underneath, these achievements embrace experimental foundations towards controlling interactions between atomic, molecular and optical systems. According to surface or interfacial structure design and time-control proven useful in the miniaturization of time-dependent interaction between classical and quantum systems.

To life

Contents

List of Figures

Acknowledgments

I thank all the people involved in the research reported in this dissertation. To the charming UC Berkeley community and its interaction which allows to be in multiple lab spaces in no-time, included the National Lab. Work in different experimental setups and collaborate with interdisciplinary groups formed by principal investigators, postdocs, other graduates, and the staff in the laboratories, specially at nanolab, the three available machine-shops, specially at the Mechanical Engineering one with all the people in there. Thanks to Mike, Gordon, Scott, Dennis, Pete and Alex who with I also shared Lab time with students. The electronic-shop staff in the physics department, now extinct. Administrative personnel in the mentioned departments, making our life smooth. I'd like to thank the whole Department of Mechanical Engineering which embraced me as one of the family and took care of me until I graduated. As I leave Berkeley, I leave part of my heart deposited in each one person that I shared an smile with or those serious and penetrating looks.

I'd like to thank Xiang Zhang for giving me the opportunity to start this journey at his Lab. Thanks for inspiring the never-resting critical thinking in my brain and letting me free-swim in this sea of fruitful and collaborative research. To professor Keneth Gustafson for his inspiring lectures, insightful comments during my career, encouragement to the researcher in me and sharing your passion for the good teaching manners. To professor Samuel Mao for his positive and cheering comments during the development of this work and during the qualifying presentation.

In the Xiang Zhang's group at Mechanical Engineering Department I thank all!, from Nga, Yuan and Xiaobo in the office, all postdocs, to the newest graduate student. Old friends who shared time with me: Werayut, Murli, Hyesog, Zhaowei, Yuan, Jason, Yi, Rupert, Atsushi, Dentcho, Lee, Peter P., Peter M., Chris G, Chris R., Avi!, Guy, Bumki, Li, Liang, Ze'ev, Daniel L., Daniel S., Haim, Ong, Annia, Jun, Volker, Bouba, Hu, Stefano and Kevin. I am sure I forgot adding one or few, cause I'm typing this to be done in few minutes

In the Department of Physics at UC Berkeley, the Department of Material Sciences and the Department of Electrical Engineering. I'd like to thank Hartmut Haffner's ion trappers of LeConte for trusting me inside Lab even when I was not returning tools to the right places. Tremendously thankful to all for your insights and advice. Specially to SQIP group for such an amazing performance, thanks Nikos for being so knowledgable, we need people like you to remain in academia. Thanks to Shane Cybart, Robert Dynes and John Clarke for letting me work on high-Tc superconductor research in your Labs at LBNL Advanced Materials and in Birge. Thanks to Feng Wang, Alex Zettl and Michael Crommie for allowing me to work in your Labs, using your equipment and sharing ideas with your postdoc and graduate students. Thanks Yuanbo Zhang for teaching me mechanical exfoliation of graphene and its characterization procedures. Thanks to Oscar Dubon for the help and inspiration to continue on this curiousity-driven living mode.

Thanks to my family and friends who stayed with me, believed in me since the start and never dropped my hand, even when I shacked it. You never left me alone and made me feel strong in my worst times. Thanks.

Chapter 1

Introduction

1.1 The big picture

The study of light and matter interaction at the nanoscale provides of a scientifically rich and an educational insightful playground for research and technological applications. It represents a source of technological revolution for future generations with a wide range on existent and novel phenomena across several fields of knowledge. Here, under the context of nano-scale optics, we engineer the experimental conditions to not only isolate and probe single interactions such as in ion-trap quantum experiments, but also for the confinement, propagation and coupling of surface electronic collective excitations. From all experiences, we recognize that at this scale, the design and integrity of the interface is of extreme importance in order to provide for the right boundary conditions to the electromagnetic fields present. We have entered the realm of surface science and thus enjoy from the not-so-well understood alien interactions provided by surfaces, which we end up studying as well. Whenever feasible, we pursue for the immediate implementation of our research into technological applications, as our highest motivational goal.

To tune system's response for the specific wavelength windows of light excitation, we are favored by the state of the art of micro and nano fabrication techniques. To mention few, material etching, thin film deposition, crystalline growth, and ultimately, the synthesis of monolayers from layered media. These thin cross-sections not only allow for cranking diverse material responses in reduced thicknesses but also the observation of responses which depart from those of the bulk. Both are useful in the design of unconventional material effective responses by coupling single-layer responses. Also, by coupling light to the motion of confined electron waves in monolayers, we could provide for the ultimate spatial-confinement of wave propagation down to a truly feasible interfacial layer between two optical media.

In order to motivate the introductory chapter we briefly present each one of the projects here described. Since most are aimed at solving a particular problem, we present a corresponding local introduction in the specific chapter, as an effort to keep each chapter self-sustained. Here, we deal with the general introduction, which embraces the need to go over

specifics of each which were not touched upon in respective chapters, but are useful in the interlinking of all to conceive a general end. Part of the concluding chapter also reveals its objective of concealing an specific title, fruit of all presented and projected into perspectives.

The first part of this dissertation focuses on interface-aided coupled interactions called surface plasmons (SPs) which are electron density surface waves coupled to an incident optical mode. These could be used as a possible replacement for both, electrons and photons in nanoscale devices due to its high spatial and temporal frequency propagating nature. We also study its interlayer coupling through thin dielectric layers as the number of them is increased. Supported effective electromagnetic responses are localized through spatial design of resonating cavities, thus a subwavelentgh engineering of optical responses is based on local subwavelength design, giving rise to the field of metamaterials from which we could create remarkably unconventional optical effective responses. Here we study two contributions to the field, the first is applied to the creation of Negative Index Metamaterials (NIMs), and the second is related to Surface states, optical analogues of solid state surface states.

Plasmonic lenses, designed for deep-subwavelength spatial confinement represent an alternative to achieve high resolution applications, however challenged due to high throughput and speed requirements. Here, we have the opportunity to link metamaterial research with time-effective digital systems and tribology research, which relates to the science and engineering of interacting surfaces in relative motion. We report time-dependent routines to generate electronic triggering signals to electro-optic modulators with controlled time-delay uncertainties. We implement finite state machines and digital (phase) lock loops on FPGA architectures to synchronize all the relevant clocks in the system. This is presented in Chapter 3 but understood applicable also for ion trapping purposes in Chapter 5 since thousands of ions are envisioned as trapped and probed with spatial and time accuracy. By using these architectures and the design described for the plasmonic lithography application, ion traps interactions could be ruled in phase to the other critical clocks in the system. This includes, the laser repetition pulses at 80MHz and even the 60Hz which feeds the systems around, interconnected through the power line in the room.

A new twist to typical layered bulk materials such as graphite is obtained by mechanical exfoliation. Graphene from graphite was found feasible and remarkable. Since then, many other materials such as MoS_2 are under extensive research. Most reported monolayers of old layered media provide extra-ordinary responses, different from thin films (already different from bulk). Some monolayers change their properties further when coupling with other layers, or due to electromagnetic effects such as is the case for absorption in graphene. Departed responses as the thickness is reduced complements our understanding of novel material's behavior as we are to interact with 2D crystalline lattices of atoms. Mechanical exfoliation and Chemical Vapor Deposition (CVD) techniques are not reviewed here, but recipes and relevant references are mentioned when needed in chapter 4 and chapter 5.

In this dissertation, an important use of graphene in the modulation of propagating infrared light in semiconductor waveguides is discussed in chapter 4. The realization of nanophotonic devices for light modulation in Silicon is integrated with an interfacial graphene absorptive layer, for telecommunication applications. In chapter 5, graphene chemical inert-

ness is proposed to reduce chemical activity at the surfaces of ion traps. However, technical difficulties intrinsic to its synthesis proves to be challenging for quantum interactions to be attained. This is due to the remaining carbon from the CVD process, part of a noisy environment for the trapped ion.

Typically, metal dielectric interfaces are used to trap ions for quantum information purposes. By spectroscopic studies of its exhibited fluorescence we can study the additional energy obtained as a decoherent process consequence of dissipation and heating provided the interaction with the surface. Surface electrode microtraps are the scalable version of a Linear Paul trap, produced by using the available micro and nano fabrication methods. However, noise near surfaces, in particular, electric field noise from the surface has been known to cause anomalous heating of the motional modes of a trapped ion. Here, phonons are used in the interaction with an ion to measure the quality of the trapping surface through the measurement of ion heating rates.

Complemented by other surface analytical tools, a complete picture of the ion-surface interaction is extracted to study surface treatment methods for cleaning traps. Since the ion is ultra sensitive to the surface, it could be used to detect certain surface properties as if it was another surface scientific tool. In this Chapter, we present information addressing the fundamentals behind the surface structure of materials, specifically those of metals and dielectrics, we also a review the relevant decoherent aspects of surface electrode microtraps.

To concretely introduce each of the fields of interest, we review key concepts from few references and merge areas as outlined above. This is not a unique flow, since time-related mechanisms could have been left until the end, however, since plasmonics lenses (a metamaterial) are involved and time-sensitive signaling is required for ion-interaction in Chapter 5 we stick with the following structure. In section 1, we start with the description of the field of nanophotonics. The Optical properties of metals and dielectrics are presented to support the field of plasmonics, the largest area of nanophotonics as feature size reduction is required for high-frequency EM wave propagation. We introduce surface plasmon polaritons and localized plasmon resonances to justify the promise of plasmonics. Active plasmonics is introduced for its application in the observation of surface plasmon stimulated emission important for the creation of a true surface plasmon stimulated emission of radiation (spaser) device capable of emitting coherent surface plasmons in nanoscale platforms. Then, we describe how atom-like behavior per layer is designed once the wavelength of incident light is larger than the corrugations provided by material thickness. We describe its respective use in metamaterials as designed subwavelength interlayer spatial coupling to obtain effective material responses when interacting with light.

After have reviewed plasmonics and metamaterials, as light interaction with novel engineered 3D systems, we focus on monolayered materials, specifically, graphene as the first conceived 2D expression of matter. We present its fascinating characteristics and important consequences in optical systems as an atom-thick material. The surface science behind Ion-trapping research comes last to wrap the use of surfaces in our research endeavors now interacting with point particles (atomic systems). For this, we introduce the surface structure and the quantum vibrational mode description for spectroscopic methods used in measuring

heating rates in Chapter 5.

1.2 Nanophotonics

By now, light applications are vast, used almost in every solution we have around; either as a source to excite responses, change system's conditions, probe state evolution, fabricate devices through lithographic processes, communicate information, or harvest energy from the sun efficiently. Applications are starting to change people's life and undoubtedly will continue to do so as we improve our understanding of light-matter interactions in deeper ways.

Nanophotonics is the field studying light behavior at nanometer scales. For our purposes, relevant phenomena exists in the ultraviolet (UV), visible (VIS) and infrared (IR) regions of the electromagnetic spectrum, corresponding roughly to wavelengths of approximately 300 to 1700 nanometers. In space-domain, it corresponds to the feasible resolution range allowed by current micro and nano fabrication methods. For larger wavelengths, it actually allows us to fabricate for light-matter interaction at deep sub-wavelength scales.

New technologies in the realm of nano-optics such as those of surface plasmon optics, changed the way we understand light-matter interaction in the surface of materials. Specifically, thickness reduction in materials such as metals or graphite, have interesting consequences when studied at this regime. In addition, artificially engineered materials with designed optical responses can be fabricated by tailoring and coupling different dynamical systems (diverse transfer functions) and tune the geometrical or electronic structure provided by subwavelength building blocks and or time-dependent perturbations.

The interaction of light with nanostructures can be used to confine electromagnetic fields to the optical near field of such a structure. The electromagnetic field adapts to the topography (shape and size) of the structure (boundary conditions). The optical near field can be seen as a surface bound optical oscillation depending on length scales smaller than the wavelength of the incident light. Since the field adapts to the structure, provides higher spatial resolution beyond the diffraction limit.

As the sizes are reduced (extrinsic size effect), novel optical properties appear. However, to completely define the material's optical response to incident light, the intrinsic electronic properties have to be defined as well. We could change this properties due to size reduction as well, just as is the case for semiconductor nanostructures and metals. By doing so, the confinement of the quantum mechanical wavefunction discretize available optical transitions.

Furthemore, due to its constitution, materials interact stronger or weaker with electromagnetic fields. Thus, by tuning the permittivity and permeability of materials, the electromagnetic response can be engineered in the nearfield. In metals, superlenses are designed by reducing the metal thickness and controlling the size of the corrugations. This size is correlated with the mean free path of the conduction electrons. To provide of a boundary contrast to conductive media and thus confine the effect to an interface, insulating materials are used.

The ultimate confinement in thickness is found in graphene, an atomically thin sheet of the a semimetal graphite with very interesting opto-electronic properties. This material has been adopted immediately in the fabrication of electronic and nanophotonic devices. Different from a metal or a semiconductor, it possesses a honey comb lattice which allows for confined electrons to move faster than those in conventional semiconducting materials. Interband transitions are tunable by external fields and thus could be used to provide for an electronic tunability of optical absorption contained in an atom-thick surface. As a result its electronic structure could be used to locally modify the interface among media or only the surface. Its obtention through CVD methods and post processing techniques allows for the possibility to place it in almost any substrate. Silicon and Quartz substrates are feasible materials and thus allows for integration in photonic interconnectors onto a microprocessor, the so called "exaflop light circuit era" of CMOS Integrated Silicon Nanophotonic technology.

In conclusion, nanophotonics is a very broad area with applications covering all areas of knowledge where light interacts with matter in the nearfield. We are capable of tailoring light interaction with nano structures if we modify the geometric and electronic structure of the surface of the material to interact. As thickness is reduced, different responses are attained, such as is the negative permitivity in thin metals, cause of surface plasmons. Dielectric materials are used to provide contrast for confinement, and so is possible to have them thin (in fact better, cause still metal ALD is not everywhere). Multilayer systems consisting of alternations of metal dielectric interfaces allows for effective response design through localization of electromagnetic modes, provided the space used is still smaller than the wavelentgh of incident light. The design is pretty much like filters or LCR circuit but for transmission or reflection of light. Combinations of reponses are used to compensate for effects or recreate others which are novel. In our case, electron transport associated with light excitation, or viceversa, is of interest. Also, we are interested in response changes as the thickness of the layer is modified. First, because we can do more effective or different metamaterials, to manipulate light. Thinner metamaterials in principle should work under the same rules for smaller wavelentghs. Second, for the control of electron confinement and optical response so that then effective responses for propagating light modes can be manipulated to obtain a characteristic behavior in the transmitted light or in the associated electronic states of the surface or interface they form. For this, we review metals, dielectrics, semimetals and different combinations, ie alloys for the obtention of crystalline forms for the best expression of metallic conductive characteristics. From thick (3D) to thin (2D) for electrons represents a drastic change with amazing physics and applications. Towards the best propagation and localization of light by carefully engineering the electronic and geometric structure of the surface, for in the second case, the interface.

1.3 Plasmonics

Plasmonics is a major area of nanophotonics, based on the interaction between electromagnetic waves and conduction electrons at metallic interfaces or geometrical structures

with sizes on the order, or less, of the wavelength of incident light. Since light is limited by diffraction, the subwavelength confinement provided by metallic nanostructures opens a broad area of studies. First, for applications where light is already used but can be optimized for subwavelength dimensions as is the case for photonics. Not only, it is possed to replace electronics in most of its applications due to the intrinsic confinement to the surface they exist upon. Second, in small particles plasmons find other applications such as for cancer research, provided light is enhanced in these metal nanoparticles.

The field is divided in many areas, but typically connected through the use of two solutions of the electromagnetic problem posted by geometrical boundary conditions and the available "free" electron sea. The electron sea is provided by metallic and semiconductors surfaces which are contrasted by using dielectrics to provide for an interface, otherwise either a far more dissipative or less conductive media would result in only less effective interfacial results. For now we think of this interface a sharp contrasting change in the spatial distribution of electrons just in the border. Excited by a wave polarized so that the electric field excites oscillations in the electron density is one of the solutions of the posed problem for propagating surface waves, called surface plasmon polaritons. Its main application is found in in optical communications due to the high frequencies and space confinement available. In fact plasmonic waveguides are the best of both expressions. Faster than electronic waves but slower than optical waves. However tougher to fracture in the channel as plasmonic waves consist of the metallic surface of bulky media, which in principle can be tougher. However, if thin, surface plasmons can be coupled by tunneling electrons as well. The other EM solution is used to describe what we call localized surface plasmons, which are of a non-propagating nature and due to that are used mostly in plasmon optics for imaging and patterning applications. Confinement of energy in subwavelentgh space is possible, and so is in the solution where most metamaterials base the use of coupled plasmonic effects in subwavelentgh regimes for an effective designed response.

A brief explanation of both kinds of plasmon waves will be described to serve as motivation and introduction to contributions presented in chapter 2 and chapter 3. While chapter 2 consist of purely plasmonic related topics, i.e. plasmonic devices and metamaterials, chapter 3 introduces time-related useful concepts for light manipulation in high frequency domains for triggering of electro-optic modulators. Also useful for electronic excitation in media, in principle metallic surfaces, which are used in FPGA devices. Chapter 3 discusses the plasmonic nanolithographic system using plasmonic lenses, but is also very useful to visualize chapter 5 electronics for the control of light interaction times and DC-electrode voltage tuning, multiplexing and logic manipulation of signals used to interact with the trapped ion.

The high density of free electrons in metals reduces electron energy level spacing so that thermal excitations (k_BT) at room temperature allow to describe plasmonics using classical electromagnetism. Certain plasmonic configurations do exhibit quantum behavior i.e. quantum plasmonics, is used to tailor strong coupling between surface plasmons and single quantum systems at deep subwavelegth scales of spatial and temporal interaction. Plasmonic circuits might allow for quantum information transport feasible to integrate with nano-scale semiconducting devices if in principle, the losses, which are of quantum nature

(as we are to describe) could be defeated. Associated with heating and dissipative effects, quantum processes for surface plasmons have been found difficult but not impossible to observe.

For the frequencies of interest UV, NIR, IR, field penetration in the metal is role factor supporting the good conductor approximation validation when solving Maxwell's equations. For low frequencies, up to the visible part of the electromagnetic spectrum, waves do not propagate through metals. Waveguides and resonators in microwave and far-infrared regions are fabricated based on negligible penetration into the metal. The good conductor approximation is still valid. At high frequencies, NIR and VIS increased field penetration leads to an increase in the dissipation of energy. In the UV most metals allow for the propagation of electromagnetic waves excluding noble metals which have strong interband transitions leading to strong absorption. Alkali metals exhibit UV transparency due to an almost free-electron like response. Dispersive properties are described by the complex dielectric function 1.1. Strong frequency dependence is understood as a consequence of changes in the phase of the induced currents with respect to the exciting field for electron relaxation times τ of the metal. Since fields are averaged over distances much larger than the microstructure, the rapidly varying microscopic fundamental interactions between charged particles inside media and electromagnetic fields, are not taken into account [1]. The relationship between the relative permittivity (dielectric function) and the conductivity of the metallic surface is described by the dielectric response equation :

$$\varepsilon(K,\omega) = 1 + \imath\frac{\sigma(K,\omega)}{\varepsilon_0\omega}) \tag{1.1}$$

A simplified spatially local response $\varepsilon(K=0,\omega) = \varepsilon(\omega)$ is valid as long as the wavelength is significantly longer than all characteristic dimensions such as unit cell size and electron mean free path in the metal. At low frequencies, ε is associated with bound charges responding to a driving field, while σ is related to the contribution of free charges into electric current flow. Also, permittivity and conductivity are complex functions of frequency ω: $\varepsilon(\omega) = \varepsilon_1(\omega) + \imath\varepsilon_2(\omega)$, $\sigma(\omega) = \sigma_1(\omega) + \imath\sigma_2(\omega)$. ε is associated with the complex refractive index $\tilde{n(\omega)} = n(\omega) + \imath\kappa(\omega)$ of the medium.

Surface Plasmon Polaritons

Surface Plasmon Polaritons (SPPs) are surface bounded electromagnetic waves coupled to electron density oscillations in metal-dielectric interfaces [2] [3] [4]. Spatial confinement of enhanced fields is useful in several applications [5] included nanolithography [12], microscopy [13] [14] [15] [16], plasmonic circuits [22] [23] [24] [25], metamaterials [18] [19] [20], solar cells [17] and bio-sensing [21]. Derivation of these surface waves as TM solution in the interface is reviewed in several texts included [6] starting from Maxwell equations and the dielectric function of the free electron system.

Plasmonic waveguides guiding two dimentional waves is reviewed here since its use its relevant in Chapter 2. A tradeoff between propagation losses and spatial confinement exists,

thus two kinds of waveguides are typically reported, thin metallic films in dielectric medium with long range propagation lengths and loosely confined mode or nano-particle/wire waveguides with a highly confined mode and shorter propagation lengths. The propagation losses are attributed to the metal thus the higher the confinement of the mode, the increased attenuation due to closer mode to metal surface interaction associated to ohmic heating, relevant in Chapter 5 for heating rates from a metallic surface.

Increase in interparticle coupling strength leads to enhanced propagation lengths for confined modes close to the light line [38]. As well, for flat interfaces there is an increase in propagation lengths and field localization [39] avoiding existing trade-off between confinement and loss, attributed to SPP field enhancement and propagation distance limits due to intrinsic electronic damping in metals. To compensate for such, the field of active plasmonics studies the interaction of surface plasmons with active media offering compensation as the possible solution for propagation losses allowing for applications such as [27] [28] [29] [30] [31] [32] [33]. Section 2.2 details our efforts towards achieving a surface plasmon waveguide in an active medium. While we are unable to compensate all propagating losses, we are able to observe stimulated emission process as reported in [150].

Localized Surface Plasmons

Localized surface plasmons are the second fundamental excitation, understood as the non propagating modes of the conduction electrons of metallic nanostructures coupling the incident electromagnetic field. These surface modes are solutions from the scattering problem of a particle of subwavelength-size in oscillating electromagnetic field. Driven electrons are attracted to the particle through an effective restoring force. Resonance leads to amplification in the nearfield inside and outside the particle. The nanoparticle acts as an electric dipole, resonantly absorbing and scattering electromagnetic fields. This resonance is called localized surface plasmon resonance, or localized plasmon resonance, which can be excited by direct illumination in contrast to the propagating modes where phase matching is required. This resonance is fundamental in optical applications of metal nanoparticles. This dipole particle plasmon resonance is only valid for particles below 10nnm for the visible and infrared regions of the spectrum of EM radiation.

The interaction of a nanoparticle with an electromagnetic field is typically treated under the quasistatic approximation provided the particle size is smaller than the wavelength of the driving field. For particles of larger dimensions, phase changes in the driving and responding field are treated using Mie theory [7]. First order corrections exist and are typically used.

The plasmon resonance is damped down by two competing processes, a radiative decay into photons, important in larger particles, and a nonradiative process due to absorption, which creates electron-hole pairs via either intraband transitions (within the conduction band) or interband transitions (from lower lying d-bands to the sp conduction band in noble metals). The physical model is detailed in reference [8]. Two-level model of the plasmon resonance is studied in reference [9]. The homogeneous linewidth of the plasmon resonance is related to an internal damping process via the introduction of a dephasing time. Analogue to

dielectric resonators, such as those of 2.4, the strength of the plasmon resonance is through the use of a quality factor Q, given in terms of the resonant energy. The coherent excitation dephases either due to energy decay or scattering events that change electron momentum. Reference [10] studies this dephasing time and relates it to a population relaxation time or decay time describing both energy loss processes (radiative and non-radiative), added to the dephasing time consequence of pure elastic collisions. For nanoparticles of noble metals, dephasing times are in the range of $\sim 5, 10fs$. Shifts in resonance frequency are designed by changing geometry and size. Coupling beween localized plasmon resonances shift the effective response due to electromagnetic interaction between the localized modes.

Since interactions are approximated of dipolar nature, the ensemble of particles is seen as a system of interacting dipoles. Interparticle junctions serve as hot-spots for field enhancement. Scattering is reduced if particles are packed so that fields are highly localized at intersticial sites. Plasmonic apertures are void plasmons sustained by an electromagnetic dipole resonance alike to that of the nanoparticle. In chapter 3, we describe plasmonic antennas in the context of plasmonic lenses for lithographic applications.

For particles smaller than 1nm, quantum effects might begin, depending on the number of electrons, the amount of energy gained by individual electron per incident photon could be significant compared to k_BT at room temperature. This problem becomes a multiple-particle problem, no longer a coherent electron oscillation[11].

1.4 Metamaterials

For noble metals, higher frequency excitation increases material permittivity significantly, so that the total electric field energy of the SPP mode inside the metal is reduced. Delocalized SPPs are due to negligible field penetration into the metal. The perfect conductor model is used when the internal fields are zero thus perfect metals can not support electromagnetic surface modes at the surface, included SPPs. However, in [34] bound electromagnetic waves mimicking SPPs are sustained by a perfect conductor provided a periodically corrugated surface. For real metals with finite conductivity with surface corrugations much smaller than the wavelength of the exciting field, the photonic response of the surface can be designed by tuning the dielectric function $\varepsilon(t)$ for the effective medium. The frequency $\omega(p)$ is tuned by designing the dispersion relations of the surface plasmon mode via surface geometry and electronic structure, for particular frequencies. In the effective medium model, the periodicity of surface corrugations allow for an average finite field penetration confining SPPs at visible frequencies. Materials with subwavelentgh geometrical structure exhibiting an effective photonic response is known as a metamaterial. Metamaterials designed for the purposes of light manipulation (refraction index tuning) and surface state engineering are presented in Chapter 2.

In perfect conductors, periodic corrugations in flat surfaces generate bound surface states. In [35], a one dimensional array of grooves of depth h and with a and periodicity d (lattice constant) is studied. The frequencies of the supported modes scale with the geometrical

size of the grooves in the perfect conductor approximation. The surface mode resonance is shown as a divergence in reflectivity and the dispersion relation for a surface mode is then determined by the poles of the reflection coefficients. For $\lambda > a, d$ the dispersion relations are closer to the light line. For finite hole depth h the existence of confined surface modes with low group velocity (coupled cavity modes) above the cutoff frequency $\omega(p)$ is supported by propagating modes inside the cavity holes, due to the excitation of cavity resonances [36]. Designer SPPs play an important role in enhanced transmission through arrays of hole sizes below the cut-off of the propagating mode [37]. Reference [40] studies extraordinary transmission through apertures related to a phase matching condition imposed by a grating. The bull's eye structure with concentric rings grating provides of both, a focusing and a coupling effect for enhanced transmission in the central aperture where both, propagating and localized surface plasmons contribute to the effect. Application of plasmonic lenses is further described in Chapter 3 for lithographic purposes.

1.5 Graphene nanophotonics

Insulators and semiconductors differ from semimetals and metals in their electrical conductivity dependance on temperature. Insulators or semiconductors have two types of charge carriers, holes and electrons. The conductivity of insulators and semiconductors increases with temperature since more electrons are shifted to the conduction band. A metal has one type of charge carrier only, the electron. Conductivity decreases with increases in temperature due to increasing interaction of electrons with phonons (lattice vibrations). Semimetals are alike metals but with both holes and electrons contributing to electrical conduction. Semimetal also differs from an insulator or semiconductor in that its conductivity is never zero, whereas a semiconductor has zero conductivity at zero temperature and insulators have zero conductivity even at room temperature, due to a wider band gap.

A particular kind of semimetal is a carbon allotrope, graphite, an electrical conductor. It is the most stable form of carbon under standard conditions [348]. Graphite is the bulk of low-dimensional allotropes such as Graphene, a 2-D single layer of graphite [44], 1-D carbon nanotubes (CNTs)[42] and 0-D fullerenes [43].

Graphene electronic structure and properties were theoretically described earlier to understand the physics of a single layer honeycomb carbon lattice [45]. Its exfoliation and CVD synthesis have been only quite recently possible. Graphene is the strongest material, even stronger than diamond stronger due to the nature of the sp2 bonding versus sp3 bonding [86]. Charge carrier densities are similar for electrons and holes with a very high current carrying capability, two orders of magnitude higher than in Cu [44], [71], [72].

Carbon nanomaterials provide long mean free paths at low bias due to weak acoustic phonon scattering and suppressed optical phonon scattering [82], [87]. Scattering mechanisms in 3-D occur even at small angles and required momentum is low, the backscattering in 1-D conductor requires much higher momentum, making the scattering weak, as a consequence, larger momentum relaxation times or mean free paths. Useful for our purposes in

the next-generation interconnects with enhanced electrical performance and reduced electromigration effects, existent in nanoscale Cu interconnects [88], [89]. Cu interconnects suffer of an increasing resistivity, current density, and temperature [90] [91] [92] when compared to carbon nanomaterials at the nanoscale. Due to this extraordinary physical properties, carbon nanomaterials are used for several applications in nanoelectronics [46], [47], spintronics [48], [49], optics [50] [99] [100] [101] [102], carbon nanotubes [103] [104], materials [51], mechanical systems [52] and biological systems[53], relativistic quantum mechanics and condensed matter physics [54], anomalous quantum Hall effect [44] [95] [96], Klein paradox [54] and coherent transport [98].

Carbon nanotubes (CNTs) and graphene nanoribbons (GNRs) have a wider range of applications, such as for energy storage [55], to convert energy using thermoelectric [56] and photovoltaic [57] devices. Field emission displays [58], nanometer semiconductor transistors [44] [59] [60] [61] [62], nanoelectromechanical systems (NEMS) [69], [64], interconnects [65] [66] [67] [68] passive devices [63], [83]. Due to electrical, thermal, and mechanical properties [94][4], [52], [71] [72] [73] [74] [75] [76] [77] [78] [79] [80] [81] [82] [83] [84] [85].

In reference [321] infrared (IR) spectroscopy is used to probe interband optical transitions in graphene mono and bilayers. Unlike conventional materials, optical transitions in graphene can be modified through electrical gate-induced changes, just as field-effectmodulated electrical conductivity, the basis of electronics. The behavior of graphene is attributed to both, its two-dimensional (2D) structure confining electrons in one atomic layer and its low density of states (DOS) near the Dirac point, causing the Fermi energy (EF) to shift with varying carrier density. The optical properties of graphene make it a promising material for IR optoelectronics due to superior carrier mobility, current carrying capability, and thermal conductivity, and can readily incorporate electrical coupling as in field-effect devices [44](12) and p-n junctions [105] [106].

Graphene growth using Chemical Vapor Deposition (CVD) is easily placed in several substrates, included Silicon and its oxide. Optical communication devices on a silicon platform [107] based on graphene should offer small footprint, high-speed, broadband, low-energy-consumption, easy-fabrication and tunable properties for a new generation of devices [111]. Graphene has been used in optical devices for bio-sensing applications [117][118][119], photo detectors [120][121][123], and waveguides [124]. Additional optical advantages include thin cross section, high carrier mobility, high thermal conductance, also a gapless energy structure. In addition, the linear conduction band meets the valence band at the Dirac point, leading to intraband and interband electronic transitions [110] [125] [126].

Its tunable conductivity σ can be written as $\sigma = \sigma^{'} + i\sigma^{''}$. For $\sigma^{''} > 0$, graphene behaves as an ultra-thin metal, thus able to support a highly confined TM mode plasma wave, thus graphene could become a good TM mode waveguide with proper doping [127] [128] [129]. Gated graphene near a silicon waveguide is applied to fabricate an optical modulator, reported in Chapter 4.

1.6 Surface microelectrode EM Ion-trapping for Scalable Quantum Information Processing (SQIP)

Important technological advances are consequence of scalable miniaturization of devices. Novel materials and physical phenomena are under extensive research for its eventual introduction to technology. One of such is the field of quantum computation, with its most notable architecture based on trapped ions. In such a setup, information is kept and transformed by coherent processes among a 2-level system (the ion) and a EM single mode field. Currently, ion traps are fabricated on flat surfaces so that familiar processes in standard microfabrication methods facilitate the scalable production of these devices. As well, it provides for an opportunity to use the trapped ion to probe the conditions of the interacting surface as an additional tool for surface science studies particularly important for quantum information processing but generally useful to all fields which dealing with similar structural aspects. Spectroscopic methods with trapped ions are used to measure heating rates, which detail the surface-ion interaction through the exchange of phonons. Few other adsorbates on the surface contribute to this phonon exchange at "anomalous" heating rates and thus disrupt quantum processes by decoherence effects.

Surfaces are of interest because when compared to the rest of the solid, they offer a unique chemistry since surface atoms react to satisfy bonding requirements. Modern surface science is particularly important in nanotechnology [133], specially if semiconductor processing is to continue reducing feature sizes down to molecular levels, expected with the rise of monolayered materials. Devices ruled by quantum effects such as single electron transistors, nanoelectromechanical systems NEMS could be manufactured by a etching an growth reactions which if controlled could perform the process one atomic layer at a time, thus structural changes can be tuned down to monolayer levels.

Interfacial effects are studied in tribology as well, applied here in Chapter 3 for flying heads. Effects of surface structure and composition, could eliminate limiting factors or tradeoffs in the design of tribological systems. Also, effective bonding of two surfaces in Chapter 2 and Chapter 5, protection of degradation (corrosion, oxidation, adsorption) due to the environment in Chapter 4, or fundamental processes happening at surfaces, still not well understood, such as the formation of other molecules [134] [135]. It is possible to reconfigure the surfaces so that different structural modifications could be studied, including Graphene, Aluminum alloys, Copper, Gold and Palladium, reported in Chapter 5.

To provide a better picture of the role of chemistry at our trap surfaces we use techniques widely recognized in surface science, included residual gas analyzers (RGA), Low energy electron diffraction (LEED), and Auger electron spectroscopy (AES) to complete the picture of the surface before and after any changes made on the surface. We modify the conditions of the surface by clearing or creating adsorbates from the surface by typical methods (UV radiation, Oxygen plasma, Argon bombardment), different athmospheres (N2, O2), and an integrated oven for insitu annealing of our surfaces.

To properly introduce our studies based on surface microfabricated ion traps and heating

rates, the important concepts of the field of surface science have to be reviewed. Reference [132] details surface structure and other useful concepts, from where we edit a brief summary aided by other sources, mentioned when used.

Surface structure

Chemistry at the surface is understood by recognizing differences between the structure of clean, partially full or fully adsorbate covered surfaces. The surface structure has two inherently coupled aspects, the electronic and geometric structure. Surface structure plays an important role in the study of the surface interaction with other systems, such as is the case of the trapped ion. In addition, as we have introduced for optical systems the interaction quality also relies on the geometrical and electronic aspects of both systems at the interface, specially as device size is reduced. A similar effect happens in plasmonic devices, where the frequency $\omega(p)$ is tuned by designing the dispersion relations of the surface plasmon mode via surface geometry and electronic structure, for particular frequencies. As well in metamaterials, where each layer can be treated as an atom-like entity in subwavelength regimes. Coupling is aided by atom-like models that aid for the design of effective media that can regreate surface states, such as our work reported in Chapter 2

One important aspect of thin film deposition is the phenomenon known as epitaxy, which happens when a material grows on top of a crystalline substrate with certain crystal orientation with respect to the substrate. Single crystal films can be of use in the investigation of solid state reactions such as alloy formation, and surface reactions. Most materials deposited with typical methods are amorphous, therefore post heat treatment (annealing) of surfaces is practiced to promote for polycrystalline films, where grains of certain crystalline orientation and size could be obtained. If they are to interact with the trapped ion, they should show a different behavior from that of neighboring (differently oriented) crystalline grains. Increase in the relative size of the grain makes for cleaner interaction simply because less grains will form part of the ion environment.

The ideal flat surface structure has a crystallographic description even when not perfectly isotropic. Stress on the surface occurs as a consequence of surface atoms broken bonds with higher energies compared to those inside bulk. Stress relaxation exist and extend several layers into the bulk. Stepped surfaces (vicinal surfaces) introduce step-like discontinuities in the surface structure. Electrons tend to spread out and smooth out step discontinuities and minimize step energies. Chemical reactivity is different at steps changing diffusion of adsorbates due to local fields thus one diffusion direction is more favorable than the other. Many high-index planes tend to facet at equilibrium, and spontaneously form arrays of low index planes. A catalogue of stepped surfaces of several surfaces such as Si(111), GaAs(100), Pt(100) is reference [136].

The surface of two metal compounds, such as those of intermetallics $Cu_3Au(100)$; (100), (111), (110), $Ni_3Al(111), (110)$, $NiAl$, $Ti_3Pt(100)$ [137] exhibit unique catalytic behavior due to the fact that the composition of the surface depends on both, the exposed surface and bulk compositions. True intermetallic compounds are formed due to material solubility,

which could be different at surfaces than inside bulk. If the surface energy of one of the components is significantly lower than that of the other, then it preferentially segregates to the surface. For binary a alloys AB, A and B are the relative sizes, as well as A-A, A-B, B-B interaction strength determines endothermic or exothermic alloy formation. Relative values determine whether segregation occurs. If formation is exothermic, then there is no segregation, unless strain in the lattice influences the energetics of segregation. Segregation is expected unless alloy formation is highly exothermic and there is a good matching of atomic radii. If the alloy is made from the deposition of one metal on top of another, then the surface structure depends on deposition conditions, more specifically, whether it was kinetically or dynamically controlled. Chapter 5 details our efforts in the fabrication of an alloy trap based on Aluminum and Copper.

The surface of transition metals cannot be approximated as having dangling bonds, since the bulk is not based on covalent bonds as in semiconductors. In transition metals, the ability for certain sites to be able to bond is related to symmetry, nature and energy of the electronic states at these sites. Surface electronic states of transition metals are extended, delocalized states that correlate poorly with unoccupied or partially occupied orbitals centered on a single metal atom. Nontransition metals such as Aluminum can also exhibit highly localized surface electronic states.

The strength of the adsorbate and surface interaction varies according to the corrugation of the surface, the underlying periodicity of surface atoms and associated electronic states. The symmetry of underlying surfaces allows for random, commensurate, incommensurate structure formation of adsorbates. This is the reason supporting our trap surfaces to be as flat as possible. Once corrugations are introduced, such as due to metal removal in CVD of graphene, we expect an increase on adsorbates at the surface. A detailed measurement of the relationship between overlayer and underlying substrate structure is obtained using Low-energy electron diffraction (LEED), one surface analytical technique available for our surface studies in Chapter 5.

Surface reconstructions minimize surface energy by reorganizing bonding of surface atoms. Surface terminations give a different periodicity to the crystal than of the bulk. In metal surfaces, delocalized electrons adjust easily to relaxations and to geometric changes in the structures of low-index planes. Dangling bonds are high-energy entities, and solids react to minimize the number of them. Step atoms are also associated with localized electronic states, even on metals. If not stabilized by simple relaxations, they undergo faceting.

At thermodynamic equilibrium, in the limit of sufficient long time and high temperature, all phases of a system posses the lowest possible chemical potential. This holds for the system gas-phase/adsorbed-phase/substrate with consequences in adsorbate structure order, provided chemisorption is sufficiently exothermic to overcome unfavorable entropy factors. Chemisorption of Hydrogen removes dangling bonds of Silicon surfaces with Si-H bond, strong and non-polar. Adsorbed-induced reconstructions have a dramatic effect on the kinetics of reactions. Surface stability is studied compared with its surface reconstruction [135] [134]. For strong interactions, high adsorbate concentrations, and an stable surface, the formation of a solid chemical compound, such as an oxide layer, or a volatile compound

(for etching) is possible. Surface structure not only affects the heat of adsorption but can also change the probability of dissociative chemisorption.

Another property of materials is called the work function, $\phi : \phi = E_{vac} - E_F$, which is the minimum energy required to remove one electron from the material at 0K. The work-function depends on the crystallographic orientation of the surface in the presence of surface defects, steps, chemical impurities [138] [139]. This is a consequence of the electron density wavefunction not terminating abruptly at the surface, instead there is an oscillating electron density near the surface before decaying into vacuum (Friedel oscillations), which create an electrostatic dipole layer. This surface dipole is the difference between electrostatic potential far into vacuum and mean potential deep in bulk.

Surface atoms behave as a kind of impurity. Associated with them there is a strong localization of electronic states at the surface, forming a true surface state (exists in the bandgap) meaning it does not interact with the bulk (not an overlapping state) as surface resonances do. Structural defects can also generate surface states and resonances. By engineering surface states, the surface may have increased or decreased electron density compared to that of the bulk and thus influence strongly the electrical properties of devices. Strong interaction between bulk and resonance reduces the lifetime of electrons excited into the resonance, while with surface states, excited electrons exhibit much longer lifetimes. In metals, an electron excited into a surface state band experiences an attractive force associated with its image potential, forming a series of bounding states or image potential states [140], surface analogues of Rydberg states in atomic and molecular systems. Reference [142] reports lifetimes for Cu(100) varied by the number of surface states. The increase in lifetimes by introducing spacer layers have also been reported in reference [143]

Analogous to electronic states, quantization of the vibrations in solids depend on the movement and direction on which atoms vibrate. Vibrations overlap forming a phonon band structure (phonon number as a function of wavevector). The behavior of an isolated molecule's energy of vibrational normal modes is studied using the harmonic oscillator model. Analogous to the quantized electromagnetic field, the vibrational state is described in terms of particle-like entities (phonons) representing quantized elastic waves. Vibrational energy of a solid is nonvanishing at 0K, as is the case for diatomic molecules. The mean phonon occupation number is described by a Planck distribution law (integer spin). Phonon number in given state is unlimited and dependent only on the temperature. As is the case for the other systems, phonon modes confined to the surface exist such as surface phonon resonances coupling with the bulk (in the bandgap) and true surface phonons existing only in the bandgap (do not interact with bulk). In particular, vibrational amplitudes perpendicular to the surface are larger for surface than for bulk atoms. The electronic noise generated by the thermal agitation of the charge carriers inside an electrical conductor at any applied voltage. The statistical physical derivation of this noise is called the fluctuation-dissipation theorem, where generalized impedance or generalized susceptibility is used. Thermal noise in an idealistic resistor is approximately white, meaning that the power spectral density is nearly constant throughout the frequency spectrum.

Different surface-sensitive techniques are used to probe surface properties. Instrumenta-

tion of surface science is reviewed in detail in references [144] [145] [147] [148]. To mention few, scanning probe techniques such as scanning tunneling microscopy and spectroscopy, atomic force microscopy, near-field scanning optical microscopy, low energy electron diffraction, electron spectroscopy, multiphoton photoemissions, Auger electron spectroscopy (AES), photoelectron microscopy, vibrational spectroscopy, infrared spectroscopy, electron energy loss spectroscopy. The sphere chamber, to report in Chapter 5 is capable of allocating few of these systems for insitu measurement of surface properties as they are changing with our experiments. It is not part of this thesis to review all of these, however for reasons that will become clearer in the text, we introduce one kind of electron spectroscopy, which is Auger electron spectroscopy (AES) in which the impinging excitation leads to an electron ejection from the solid from which energy as well as angular spatial distribution can be detected and analyzed. Further details can be found in the book by [145].

The depth profile of a surface can be extracted by a combination of AES and sputtering [144] [149]. High energy electron beams are focused to few nm spot sizes, thus has higher resolution surface microscopy than XPS. It can be used as an Scanning electron microscope to image the topography as well as providing information on the elemental composition of the surface. Auger spectroscopy can be used to detect any element apart from hydrogen and Helium. For surface analytical purposes the exact energy and lineshape of Auger transitions is not needed in order to know the composition of the surface, thus low resolution is enough for a quantitative surface analysis. Small energy differences from different elements tend to be fairly widely spaced in energy and do not overlap, making the highly resolved analysis more complicated.

1.7 Organization and Contribution of this Thesis

As stated in the last section of this chapter, the interface aspect tunes the interaction between light and the available electrons. Observed effective for each of the devices fabricated on a surface, structure modification was achieved by introducing an electronic interface or modifying the geometrical structure (according to the wavelength of the incident light). Chapter 2 details our work on plasmonic devices and Chapter 3 on plasmonic lenses and tribology for lithographic purposes. We also change the electronic structure of the surface, as is shown in Chapter 4 with graphene, for which we modify the density of electrons near an optical waveguide by applying an electric field. Chapter 5 does combine everything previously covered in order to understand the surface science of similar devices (dielectric substrates and metallic surfaces) which are used to trapped ions, and from which we can extract important information of the surface through heating rates measurements. To conclude, we remark on nanophotonic integration and review few interesting work towards the future of plasmonic metamaterials and other monolayered nonlinear optical system capable to interact with quantum systems in nano-devices. Due to the independent nature of each device and or system reported, introduction to each is presented in each chapter, as well as conclusions and references.

Bibliography

[1] Jackson. *Classical Electrodynamics*. 1962.

[2] Raether Heinz. *Surface plasmons*. Springer-Verlag Berlin, 1988.

[3] RH Ritchie. "Plasma losses by fast electrons in thin films". In: *Physical Review* 106.5 (1957), p. 874.

[4] EN Economou. "Surface plasmons in thin films". In: *Physical review* 182.2 (1969), p. 539.

[5] William L Barnes, Alain Dereux, Thomas W Ebbesen, et al. "Surface plasmon subwavelength optics". In: *Nature* 424.6950 (2003), p. 824.

[6] Stefan A Maier. *Plasmonics: fundamentals and applications*. Springer Science+ Business Media, 2007.

[7] G Mie. "Articles on the optical characteristics of turbid tubes, especially colloidal metal solutions". In: *Ann. Phys* 25.3 (1908), pp. 377–445.

[8] C Sönnichsen et al. "Plasmon resonances in large noble-metal clusters". In: *New Journal of Physics* 4.1 (2002), p. 93.

[9] EJ Heilweil and RM Hochstrasser. "Nonlinear spectroscopy and picosecond transient grating study of colloidal gold". In: *The Journal of chemical physics* 82 (1985), p. 4762.

[10] Stephan Link and Mostafa A El-Sayed. "Shape and size dependence of radiative, non-radiative and photothermal properties of gold nanocrystals". In: *International Reviews in Physical Chemistry* 19.3 (2000), pp. 409–453.

[11] Uwe Kreibig and Michael Vollmer. "Optical properties of metal clusters". In: (1995).

[12] Werayut Srituravanich et al. "Plasmonic nanolithography". In: *Nano letters* 4.6 (2004), p. 1085.

[13] Nicholas Fang et al. "Sub-diffraction-limited optical imaging with a silver superlens". In: *Science* 308.5721 (2005), p. 534.

[14] Zhaowei Liu et al. "Far-field optical hyperlens magnifying sub-diffraction-limited objects". In: *Science* 315.5819 (2007), p. 1686.

[15] John Brian Pendry. "Negative refraction makes a perfect lens". In: *Physical review letters* 85.18 (2000), p. 3966.

[16] Igor I Smolyaninov, Yu-Ju Hung, and Christopher C Davis. "Magnifying superlens in the visible frequency range". In: *Science* 315.5819 (2007), p. 1699.

[17] P Andrew, SC Kitson, and WL Barnes. "Surface-plasmon energy gaps and photoabsorption". In: *journal of modern optics* 44.2 (1997), p. 395.

[18] Vladimir M Shalaev. "Optical negative-index metamaterials". In: *Nature photonics* 1.1 (2007), p. 41.

[19] VP Safonov et al. "Spectral dependence of selective photomodification in fractal aggregates of colloidal particles". In: *Physical review letters* 80.5 (1998), p. 1102.

[20] DR Smith, JB Pendry, and MCK Wiltshire. "Metamaterials and negative refractive index". In: *Science* 305.5685 (2004), p. 788.

[21] Katrin Kneipp et al. "Single molecule detection using surface-enhanced Raman scattering (SERS)". In: *Physical Review Letters* 78.9 (1997), p. 1667.

[22] Sergey I Bozhevolnyi et al. "Waveguiding in surface plasmon polariton band gap structures". In: *Physical Review Letters* 86.14 (2001), p. 3008.

[23] H Ditlbacher et al. "Two-dimensional optics with surface plasmon polaritons". In: *Applied Physics Letters* 81.10 (2002), p. 1762.

[24] Stefan A Maier. "Plasmonics: metal nanostructures for subwavelength photonic devices". In: *Selected Topics in Quantum Electronics, IEEE Journal of* 12.6 (2006), p. 1214.

[25] JA Dionne et al. "Plasmon slot waveguides: Towards chip-scale propagation with subwavelength-scale localization". In: *Physical Review B* 73.3 (2006), p. 035407.

[26] JJ Burke, GI Stegeman, and T Tamir. "Surface-polariton-like waves guided by thin, lossy metal films". In: *Physical Review B* 33.8 (1986), p. 5186.

[27] Domenico Pacifici, Henri J Lezec, and Harry A Atwater. "All-optical modulation by plasmonic excitation of CdSe quantum dots". In: *Nature photonics* 1.7 (2007), p. 402.

[28] J Gómez Rivas et al. "Low-frequency active surface plasmon optics on semiconductors". In: *Applied physics letters* 88.8 (2006), p. 082106.

[29] Alexey V Krasavin and NI Zheludev. "Active plasmonics: Controlling signals in Au/Ga waveguide using nanoscale structural transformations". In: *Applied physics letters* 84.8 (2004), p. 1416.

[30] S Anantha Ramakrishna and John B Pendry. "Removal of absorption and increase in resolution in a near-field lens via optical gain". In: *Physical Review B* 67.20 (2003), p. 201101.

[31] DE Chang et al. "Quantum optics with surface plasmons". In: *Physical review letters* 97.5 (2006), p. 53002.

[32] J Bellessa et al. "Strong coupling between surface plasmons and excitons in an organic semiconductor". In: *Physical review letters* 93.3 (2004), p. 36404.

[33] Arup Neogi et al. "Enhancement of spontaneous recombination rate in a quantum well by resonant surface plasmon coupling". In: *Physical Review B* 66.15 (2002), p. 153305.

[34] JB Pendry, L Martin-Moreno, and FJ Garcia-Vidal. "Mimicking surface plasmons with structured surfaces". In: *Science* 305.5685 (2004), pp. 847–848.

[35] FJ Garcia-Vidal, L Martin-Moreno, and JB Pendry. "Surfaces with holes in them: new plasmonic metamaterials". In: *Journal of optics A: Pure and applied optics* 7.2 (2005), S97.

[36] Min Qiu. "Photonic band structures for surface waves on structured metal surfaces". In: *Optics express* 13.19 (2005), pp. 7583–7588.

[37] Alastair P Hibbins et al. "Waveguide arrays as plasmonic metamaterials: transmission below cutoff". In: *Physical review letters* 96.7 (2006), p. 073904.

[38] DS Citrin. "Plasmon-polariton transport in metal-nanoparticle chains embedded in a gain medium". In: *Optics letters* 31.1 (2006), pp. 98–100.

[39] Ivan Avrutsky. "Surface plasmons at nanoscale relief gratings between a metal and a dielectric medium with optical gain". In: *Physical Review B* 70.15 (2004), p. 155416.

[40] Thomas W Ebbesen et al. "Extraordinary optical transmission through sub-wavelength hole arrays". In: *Nature* 391.6668 (1998), pp. 667–669.

[41] Riichiro Saito, Gene Dresselhaus, Mildred S Dresselhaus, et al. *Physical properties of carbon nanotubes*. Vol. 4. Imperial college press London, 1998.

[42] Sumio Iijima et al. "Helical microtubules of graphitic carbon". In: *nature* 354.6348 (1991), pp. 56–58.

[43] HW Kroto, AW Allaf, and SP Balm. "C60: Buckminsterfullerene". In: *Chemical Reviews* 91.6 (1991), pp. 1213–1235.

[44] KS Novoselov et al. "Electric field effect in atomically thin carbon films". In: *Science* 306.5696 (2004), pp. 666–669.

[45] PR Wallace. "The band theory of graphite". In: *Physical Review* 71.9 (1947), p. 622.

[46] Phaedon Avouris, Zhihong Chen, and Vasili Perebeinos. "Carbon-based electronics". In: *Nature nanotechnology* 2.10 (2007), pp. 605–615.

[47] Qing Cao and John A Rogers. "Ultrathin Films of Single-Walled Carbon Nanotubes for Electronics and Sensors: A Review of Fundamental and Applied Aspects". In: *Advanced Materials* 21.1 (2009), pp. 29–53.

[48] Kazuhito Tsukagoshi, Bruce W Alphenaar, and Hiroki Ago. "Coherent transport of electron spin in a ferromagnetically contacted carbon nanotube". In: *Nature* 401.6753 (1999), pp. 572–574.

[49] Young-Woo Son, Marvin L Cohen, and Steven G Louie. "Half-metallic graphene nanoribbons". In: *Nature* 444.7117 (2006), pp. 347–349.

[50] JA Misewich et al. "Electrically induced optical emission from a carbon nanotube FET". In: *Science* 300.5620 (2003), pp. 783–786.

[51] Ning Wang et al. "Materials science: Single-walled 4 Å carbon nanotube arrays". In: *Nature* 408 (2000), pp. 50–51.

[52] Min-Feng Yu et al. "Strength and breaking mechanism of multiwalled carbon nanotubes under tensile load". In: *Science* 287.5453 (2000), pp. 637–640.

[53] Fushen Lu et al. "Advances in bioapplications of carbon nanotubes". In: *Advanced Materials* 21.2 (2009), pp. 139–152.

[54] Mikhail I Katsnelson and KS Novoselov. "Graphene: New bridge between condensed matter physics and quantum electrodynamics". In: *Solid State Communications* 143.1 (2007), pp. 3–13.

[55] Chunsheng Du, Jeff Yeh, and Ning Pan. "High power density supercapacitors using locally aligned carbon nanotube electrodes". In: *Nanotechnology* 16.4 (2005), p. 350.

[56] Peng Wei et al. "Anomalous thermoelectric transport of Dirac particles in graphene". In: *Physical review letters* 102.16 (2009), p. 166808.

[57] Hiroki Ago et al. "Composites of carbon nanotubes and conjugated polymers for photovoltaic devices". In: *Advanced Materials* 11.15 (1999), pp. 1281–1285.

[58] WB Choi et al. "Fully sealed, high-brightness carbon-nanotube field-emission display". In: *Applied physics letters* 75 (1999), p. 3129.

[59] Xiaolin Li et al. "Chemically derived, ultrasmooth graphene nanoribbon semiconductors". In: *Science* 319.5867 (2008), pp. 1229–1232.

[60] Philip G Collins, Michael S Arnold, and Phaedon Avouris. "Engineering carbon nanotubes and nanotube circuits using electrical breakdown". In: *Science* 292.5517 (2001), pp. 706–709.

[61] Henk W Ch Postma et al. "Carbon nanotube single-electron transistors at room temperature". In: *Science* 293.5527 (2001), pp. 76–79.

[62] Joerg Appenzeller et al. "Comparing carbon nanotube transistors-the ideal choice: a novel tunneling device design". In: *Electron Devices, IEEE Transactions on* 52.12 (2005), pp. 2568–2576.

[63] Jae Eun Jang et al. "Nanoscale memory cell based on a nanoelectromechanical switched capacitor". In: *Nature nanotechnology* 3.1 (2007), pp. 26–30.

[64] Hamed Dadgour, Alan M Cassell, and Kaustav Banerjee. "Scaling and variability analysis of CNT-based NEMS devices and circuits with implications for process design". In: *Electron Devices Meeting, 2008. IEDM 2008. IEEE International*. IEEE. 2008, pp. 1–4.

[65] Franz Kreupl et al. "Carbon nanotubes in interconnect applications". In: *Microelectronic Engineering* 64.1 (2002), pp. 399–408.

[66] Jun Li et al. "Bottom-up approach for carbon nanotube interconnects". In: *Applied Physics Letters* 82.15 (2003), pp. 2491–2493.

[67] Mizuhisa Nihei et al. "Low-resistance multi-walled carbon nanotube vias with parallel channel conduction of inner shells [IC interconnect applications]". In: *Interconnect Technology Conference, 2005. Proceedings of the IEEE 2005 International*. IEEE. 2005, pp. 234–236.

[68] Akio Kawabata et al. "Robustness of CNT via interconnect fabricated by low temperature process over a high-density current". In: *Interconnect Technology Conference, 2008. IITC 2008. International*. IEEE. 2008, pp. 237–239.

[69] JE Jang et al. "Nanoscale capacitors based on metal-insulator-carbon nanotube-metal (MICNM) structures". In: *Solid-State Device Research Conference, 2005. ESSDERC 2005. Proceedings of 35th European*. IEEE. 2005, pp. 545–547.

[70] Hong Li and Kaustav Banerjee. "High-frequency effects in carbon nanotube interconnects and implications for on-chip inductor design". In: *Electron Devices Meeting, 2008. IEDM 2008. IEEE International*. IEEE. 2008, pp. 1–4.

[71] M Radosavljević, J Lefebvre, and AT Johnson. "High-field electrical transport and breakdown in bundles of single-wall carbon nanotubes". In: *Physical Review B* 64.24 (2001), p. 241307.

[72] BQ Wei, R Vajtai, and PM Ajayan. "Reliability and current carrying capacity of carbon nanotubes". In: *Applied Physics Letters* 79.8 (2001), pp. 1172–1174.

[73] F Li et al. "Tensile strength of single-walled carbon nanotubes directly measured from their macroscopic ropes". In: *Applied physics letters* 77.20 (2000), pp. 3161–3163.

[74] J Hone et al. "Thermal conductivity of single-walled carbon nanotubes". In: *Physical Review B* 59.4 (1999), R2514–R2516.

[75] Choongho Yu et al. "Thermal conductance and thermopower of an individual single-wall carbon nanotube". In: *Nano Letters* 5.9 (2005), pp. 1842–1846.

[76] P Kim et al. "Thermal transport measurements of individual multiwalled nanotubes". In: *Physical review letters* 87.21 (2001), p. 215502.

[77] Alexander A Balandin et al. "Superior thermal conductivity of single-layer graphene". In: *Nano letters* 8.3 (2008), pp. 902–907.

[78] S Ghosh et al. "Extremely high thermal conductivity of graphene: Prospects for thermal management applications in nanoelectronic circuits". In: *Applied Physics Letters* 92 (2008), p. 151911.

[79] CL Kane et al. "Temperature-dependent resistivity of single-wall carbon nanotubes". In: *EPL (Europhysics Letters)* 41.6 (1998), p. 683.

[80] Takeshi Kawano et al. "An electrothermal carbon nanotube gas sensor". In: *Nano letters* 7.12 (2007), pp. 3686–3690.

[81] Q Shao et al. "High-temperature quenching of electrical resistance in graphene interconnects". In: *Applied Physics Letters* 92.20 (2008), pp. 202108–202108.

[82] Ji-Yong Park et al. "Electron-phonon scattering in metallic single-walled carbon nanotubes". In: *Nano Letters* 4.3 (2004), pp. 517–520.

[83] H_J Li et al. "Multichannel ballistic transport in multiwall carbon nanotubes". In: *Physical review letters* 95.8 (2005), p. 086601.

[84] KI Bolotin et al. "Temperature-dependent transport in suspended graphene". In: *Physical review letters* 101.9 (2008), p. 096802.

[85] KM Liew et al. "Thermal stability of single and multi-walled carbon nanotubes". In: *Physical Review B* 71.7 (2005), p. 075424.

[86] Changgu Lee et al. "Measurement of the elastic properties and intrinsic strength of monolayer graphene". In: *science* 321.5887 (2008), pp. 385–388.

[87] D Gunlycke, HM Lawler, and CT White. "Room-temperature ballistic transport in narrow graphene strips". In: *Physical Review B* 75.8 (2007), p. 085418.

[88] W Steinhogl et al. "Comprehensive study of the resistivity of copper wires with lateral dimensions of 100 nm and smaller". In: *Journal of Applied Physics* 97.2 (2005), pp. 023706–023706.

[89] Sungjun Im et al. "Scaling analysis of multilevel interconnect temperatures for high-performance ICs". In: *Electron Devices, IEEE Transactions on* 52.12 (2005), pp. 2710–2719.

[90] Navin Srivastava and Kaustav Banerjee. "A comparative scaling analysis of metallic and carbon nanotube interconnections for nanometer scale VLSI technologies". In: *Proc. 21st Intl. VLSI Multilevel Interconnect Conf.* 2004, pp. 393–398.

[91] Navin Srivastava and Kaustav Banerjee. "Interconnect challenges for nanoscale electronic circuits". In: *Jom* 56.10 (2004), pp. 30–31.

[92] Kaustav Banerjee and Navin Srivastava. "Are carbon nanotubes the future of VLSI interconnections?" In: *Proceedings of the 43rd annual Design Automation Conference*. ACM. 2006, pp. 809–814.

[93] Carter T White and John W Mintmire. "Fundamental properties of single-wall carbon nanotubes". In: *The Journal of Physical Chemistry B* 109.1 (2005), pp. 52–65.

[94] KS Novoselov et al. "Two-dimensional gas of massless Dirac fermions in graphene". In: *nature* 438.7065 (2005), pp. 197–200.

[95] KS Novoselov et al. "Unconventional quantum Hall effect and Berrys phase of 2π in bilayer graphene". In: *Nature Physics* 2.3 (2006), pp. 177–180.

[96] Yuanbo Zhang et al. "Experimental observation of the quantum Hall effect and Berry's phase in graphene". In: *Nature* 438.7065 (2005), pp. 201–204.

[97] MI Katsnelson, KS Novoselov, and AK Geim. "Chiral tunnelling and the Klein paradox in graphene". In: *Nature Physics* 2.9 (2006), pp. 620–625.

[98] F Miao et al. "Phase-coherent transport in graphene quantum billiards". In: *Science* 317.5844 (2007), pp. 1530–1533.

[99] AC Ferrari et al. "Raman spectrum of graphene and graphene layers". In: *Physical review letters* 97.18 (2006), p. 187401.

[100] Jun Yan et al. "Electric field effect tuning of electron-phonon coupling in graphene". In: *Physical review letters* 98.16 (2007), p. 166802.

[101] Z Jiang et al. "Infrared spectroscopy of Landau levels of graphene". In: *Physical review letters* 98.19 (2007), p. 197403.

[102] C Casiraghi et al. "Rayleigh imaging of graphene and graphene layers". In: *Nano letters* 7.9 (2007), pp. 2711–2717.

[103] Sergei M Bachilo et al. "Structure-assigned optical spectra of single-walled carbon nanotubes". In: *Science* 298.5602 (2002), pp. 2361–2366.

[104] Feng Wang et al. "The optical resonances in carbon nanotubes arise from excitons". In: *Science* 308.5723 (2005), pp. 838–841.

[105] B Huard et al. "Transport measurements across a tunable potential barrier in graphene". In: *Physical review letters* 98.23 (2007), p. 236803.

[106] JR Williams, L DiCarlo, and CM Marcus. "Quantum Hall effect in a gate-controlled pn junction of graphene". In: *Science* 317.5838 (2007), pp. 638–641.

[107] Stewart E Miller. "Integrated optics- An introduction(Laser beam circuitry miniaturization facilitating laser circuit assembly isolation from thermal, mechanical and ambient changes)". In: *Bell System Technical Journal* 48 (1969), pp. 2059–2069.

[108] Graham T Reed et al. "Silicon optical modulators". In: *Nature Photonics* 4.8 (2010), pp. 518–526.

[109] K Novoselov. "1. The rise of graphene AK Geim and KS Novoselov Nat. Mater., vol. 6, no. 3, pp. 183-191, 2007". In: *Nat. Mater* 6.3 (2007), pp. 183–191.

[110] Kostya Novoselov. "Graphene: Mind the gap". In: *Nature materials* 6.10 (2007), pp. 720–721.

[111] Andre Konstantin Geim. "Graphene: status and prospects". In: *science* 324.5934 (2009), pp. 1530–1534.

[112] Qiaoliang Bao and Kian Ping Loh. "Graphene photonics, plasmonics, and broadband optoelectronic devices". In: *ACS nano* 6.5 (2012), pp. 3677–3694.

[113] Zhaolin Lu and Wangshi Zhao. "Nanoscale electro-optic modulators based on graphene-slot waveguides". In: *JOSA B* 29.6 (2012), pp. 1490–1496.

[114] Chao Xu et al. "Characteristics of electro-refractive modulating based on Graphene-Oxide-Silicon waveguide". In: *Optics Express* 20.20 (2012), pp. 22398–22405.

[115] David R Andersen. "Graphene-based long-wave infrared TM surface plasmon modulator". In: *JOSA B* 27.4 (2010), pp. 818–823.

[116] Steven J Koester and Mo Li. "High-speed waveguide-coupled graphene-on-graphene optical modulators". In: *Applied Physics Letters* 100.17 (2012), pp. 171107–171107.

[117] L Wu et al. "Highly sensitive graphene biosensors based on surface plasmon resonance". In: *Optics express* 18.14 (2010), pp. 14395–14400.

[118] Seung Ho Choi, Young L Kim, and Kyung Min Byun. "Graphene-on-silver substrates for sensitive surface plasmon resonance imaging biosensors". In: *Optics express* 19.2 (2011), pp. 458–466.

[119] Omer Salihoglu, Sinan Balci, and Coskun Kocabas. "Plasmon-polaritons on graphene-metal surface and their use in biosensors". In: *Applied Physics Letters* 100.21 (2012), pp. 213110–213110.

[120] Fengnian Xia et al. "Ultrafast graphene photodetector". In: *Nature nanotechnology* 4.12 (2009), pp. 839–843.

[121] Thomas Mueller, Fengnian Xia, and Phaedon Avouris. "Graphene photodetectors for high-speed optical communications". In: *Nature Photonics* 4.5 (2010), pp. 297–301.

[122] Francesco Bonaccorso et al. "Graphene photonics and optoelectronics". In: *Nature Photonics* 4.9 (2010), pp. 611–622.

[123] Marco Furchi et al. "Microcavity-integrated graphene photodetector". In: *Nano letters* 12.6 (2012), pp. 2773–2777.

[124] Jin Tae Kim and Sung-Yool Choi. "Graphene-based plasmonic waveguides for photonic integrated circuits". In: *Optics Express* 19.24 (2011), pp. 24557–24562.

[125] SA Mikhailov and K Ziegler. "New electromagnetic mode in graphene". In: *Physical review letters* 99.1 (2007), p. 016803.

[126] George W Hanson. "Dyadic Greens functions and guided surface waves for a surface conductivity model of graphene". In: *Journal of Applied Physics* 103.6 (2008), pp. 064302–064302.

[127] Marinko Jablan, Hrvoje Buljan, and Marin Soljačić. "Plasmonics in graphene at infrared frequencies". In: *Physical review B* 80.24 (2009), p. 245435.

[128] Ashkan Vakil and Nader Engheta. "Transformation optics using graphene". In: *Science* 332.6035 (2011), pp. 1291–1294.

[129] Bing Wang et al. "Strong coupling of surface plasmon polaritons in monolayer graphene sheet arrays". In: *Physical Review Letters* 109.7 (2012), p. 073901.

[130] Lei Ren et al. "Terahertz and infrared spectroscopy of gated large-area graphene". In: *Nano letters* 12.7 (2012), pp. 3711–3715.

[131] Sukosin Thongrattanasiri, Frank HL Koppens, and F Javier García de Abajo. "Complete optical absorption in periodically patterned graphene". In: *Physical Review Letters* 108.4 (2012), p. 047401.

[132] Kurt K Kolasinski. *Surface science: foundations of catalysis and nanoscience*. Wiley, 2012.

[133] A Patrykiejew, Stefan Sokołowski, and Kurt Binder. "Phase transitions in adsorbed layers formed on crystals of square and rectangular surface lattice". In: *Surface science reports* 37.6 (2000), pp. 207–344.

[134] GA Somorjai and Y Li. "Introduction to Surface Science and Catalysis". In: *See for example Wiley New York* (1994).

[135] GA Somorjai. "Surface reconstruction and catalysis". In: *Annual Review of Physical Chemistry* 45.1 (1994), pp. 721–751.

[136] Vitaliy A Shchukin and Dieter Bimberg. "Spontaneous ordering of nanostructures on crystal surfaces". In: *Reviews of Modern Physics* 71.4 (1999), p. 1125.

[137] Charles T Campbell. "Bimetallic surface chemistry". In: *Annual Review of Physical Chemistry* 41.1 (1990), pp. 775–837.

[138] Roman Smoluchowski. "Anisotropy of the electronic work function of metals". In: *Physical Review* 60.9 (1941), p. 661.

[139] K Besocke, B Krahl-Urban, and H Wagner. "Dipole moments associated with edge atoms; A comparative study on stepped Pt, Au and W surfaces". In: *Surface Science* 68 (1977), pp. 39–46.

[140] Richard Haight. "Electron dynamics at surfaces". In: *Surface science reports* 21.8 (1995), pp. 275–325.

[141] W Steinmann and Th Fauster. "Two-photon photoelectron spectroscopy of electronic states at metal surfaces". In: *Laser Spectroscopy and Photochemistry on Metal Surfaces. Part I* (1995), p. 184.

[142] U Höfer et al. "Time-resolved coherent photoelectron spectroscopy of quantized electronic states on metal surfaces". In: *Science* 277.5331 (1997), pp. 1480–1482.

[143] M Wolf, E Knoesel, and T Hertel. "Ultrafast dynamics of electrons in image-potential states on clean and Xe-covered Cu (111)". In: *Physical Review B* 54.8 (1996), R5295–R5298.

[144] John C Vickerman and Ian Stuart Gilmore. *Surface analysis: the principal techniques*. Vol. 2. Wiley Online Library, 2009.

[145] Gerhard Ertl and Jürgen Küppers. *Low energy electrons and surface chemistry*. VCH Verlagsgellschaft Distribution USA and Canada VCH Publishers, 1985.

[146] David Phillip Woodruff and Trevor A Delchar. *Modern techniques of surface science*. Cambridge University Press, 1994.

[147] Leonard C Feldman and James W Mayer. *Fundamentals of surface and thin film analysis*. Vol. 119. North-Holland New York, 1986.

[148] John T Yates and Lawrence G Rubin. "Experimental innovations in surface science: a guide to practical laboratory methods and instruments". In: *Physics Today* 51.8 (1998), pp. 66–66.

[149] S Hofmann. "Sputter depth profile analysis of interfaces". In: *Reports on Progress in Physics* 61.7 (1998), p. 827.

Chapter 2

Plasmonic Devices

2.1 Introduction

After reviewing some of the fundamentals of plasmonics in the previous chapter, we now review experimental practices in the field towards the development of applications. Three of the five prominent research areas in plasmonics are reviewed here. One of such areas studies the propagation of surface plasmons in waveguides and high-quality of resonance via cavities, the main passive devices of this infrastructure. Another area studies the transmission of light through subwavelength apertures via plasmon excitations, from which it was found enhanced transmission of light in aperture arrays. Important optical patterning and imaging applications are based on this effect, one reviewed in Chapter 3. Complex plasmonic structures with subwavelength sized alterations gives rise to the field of plasmonic metamaterials, experimentally implemented here to achieve unconventional effective optical responses such as negative index of refraction or allow to theoretically study the creation of optical surface states in metal-dielectric metamaterials. The other two research areas are related to surface-enhanced Raman spectroscopy, studying highly localized fields around metallic nanostructures to enhance emission of molecules placed in hot spots; and biological sensing and labeling using different methods of spectroscopy for localized modes.

Here, we will review our contributions to the first three areas. Enhanced transmission through subwavelength holes is used as the principle for the plasmonic lens effect which is used in Plasmonic Nanolithography to be discussed in Chapter 3. This chapter is divided in four sections (published in five papers [150], [187], [218], [249], [250]); the first two of the contributions in the area of plasmonics for control of surface plasmon transport and amplification. Section 2.2, presents plasmon waveguide devices, key in the conception of integrated devices for coupling electronic and photonic devices, loss compensation through design of active waveguides in the pursue of SPP amplifiers (spasers). Section 2.3 describe our work on another interesting plasmonic device, a High-Q surface plasmon cavity, which is a plasmonic resonant structure that could exploit field compression in order to have ultrasmall-mode-volume devices. The third and fourth contributions were on the area of metamaterials,

in section 2.4, the first demonstration of negative index of refraction in the visible part of the electromagnetic spectrum and the study of metallo-dielectric structures and its surface states as a way to mimic solid state surface state dynamics.

2.2 Plasmonic Waveguides and Gain Media

Here, we detail our study and experimental efforts in the control of surface plasmon propagation in passive devices. As described earlier, the existing trade-off between confinement and loss demands for geometrical design of the plasmonic interface, which depends on the length scale over which energy is to be transferred. Typically, thin metal waveguides in homogeneous media can guide SPPs over long distances with weakly confined fields, and also waveguides consisting on metal nanowires or nanoparticles can exhibit transverse modes with high energy confinement below the diffraction limit with reduced propagation lengths. Routing of SPPs on planar interfaces with small attenuation or enhancement is key in the propagation of signals or fabrication of nanoscale coherent light sources. The unique features of surface plasmons, such as enhanced and spatially confined electromagnetic field at metal-dielectric interfaces have been exploited in various fields [151], [152], [153], [154], [155], [156], [157] from which exciting applications remain impractical due to high losses resulting from the damping of electromagnetic fields in metals.

The field of active plasmonics studies the interaction between surface plasmons and an active medium, possibly increasing the number of applications [151] [152] [153] [154] [155] [156] [157] [158] [159] [160] [161] [162] [163] [164] [165]. To overcome losses, work focused on surface plasmon amplification [166] [167] [168] [169] [170] [171] [172] [173] . The gain medium provides the energy to compensate for the SPP loss by the process of stimulated emission, thus increasing the SPP propagation length imposing stringent requirements on gain media. Other attempts based on quantum well heterostructures [166] [167] [168], quantum dot inclusions [169], and dye molecules [170] have been reported. Lasing of a non-pure plasmonic mode has been demonstrated in metallic-coated nanocavities using semiconductor heterostructures [174].

Observation of Stimulated Emission of Surface Plasmons

Various structures utilizing several metal geometries and active media have been theoretically studied to achieve surface plasmon amplification. It has been studied in planar metallic films, strips and gratings [168] [167] [170][166]. Gain media and localized surface plasmons are also discussed with regard to random composite materials consisting of metal particles and two-level emitters [181] [182] [183]. Some recent experiments have demonstrated SPP lasing at the wavelength of 10 μm [184], partial compensation of losses in localized surface plasmons [185] and SPPs at visible wavelengths [186]. Experimental work on surface plasmon amplification in the visible and infrared frequencies has not been satisfactory in terms of the magnitude of amplification.

To realize SPP lasing is important to establish stimulated emission of SPPs. Previous experiments have studied stimulated emission of SPPs by measuring the change in the reflectance. However, the observation is indirect and the small measured change offers limited evidence of SPP enhancement ($\sim 10e^{-5}$ in differential reflectance corresponds to a gain of $0.8cm^{-1}$). In our case, stimulated emission of SPP is studied by measuring the change in the propagation length in a SPP waveguide to provide direct evidence of the SPP enhancement. Our measurements are performed in both continuous and pulsed modes to prove that the enhancement arises from stimulated emission only and not by SPP contribution from spontaneous emission. Our work offers the possibility to realize SPP-based applications such as plasmonics-based signal processing.

To study stimulated emission of SPPs, we fabricated plasmon waveguides, thin gold strips embedded in erbium-doped phosphate glass (operating at telecom wavelengths) as shown in Figure 2.1. A symmetric configuration was chosen in order to support a long-range surface plasmon mode with a symmetric transverse electric field. [175] [176]. Experiments were designed in a way that both the pump and the signal are SPPs interacting with erbium ions. By first pumping SPPs, we excite active erbium ions (in the phosphate host glass) to a higher energy state. These excited ions decay by spontaneous emission process into all the available modes. This configuration can support multiple plasmonic spatial modes [175] however most of these modes are highly confined thus they have short propagation length. Only a small fraction of energy is carried by the long-range SPP mode by spontaneous emission. The energy transfer can be routed to long-range SPP mode by the process of stimulated emission using signal SPP (Figure 2.1b). For this to happen, the buildup time of stimulated emission needs to be shorter than the excited-state lifetime of the ion; this is easily satisfied due to the long lifetime ($\sim 7.9ms$) of the excited erbium ions. An attenuation as low as 1.4 dB/cm was obtained by the long-range mode supported by metal strip SPP waveguides depending on the cross-section geometry (width and thickness) of the metal strips, cladding materials, and fabrication methods,[160][177] whereas a gain of 4.1 dB/cm using Er-doped glass with $5.31020cm^{-3}$ Er^{3+} concentration was experimentally obtained [178]. This comparable gain with SPP propagation loss of metal strip waveguides and erbium-doped phosphate glass implies that lossless propagation of SPP or even lasing could be possible in configurations of SPP waveguides surrounded by Er-doped glass.

Our experimental setup, as shown in Figure 2.2 is designed to accommodate the optical pumping of Er-doped glass by using a long-range SPP mode guided by the same metal strip. We use a laser diode with wavelength of 1480 nm as the pump laser and another laser diode at 1532 nm as the signal. The pump and signal input fibers are mixed by a fiber multiplexer and connected to the SPP waveguides using a regular single mode fiber with a polarization controller. The modes are overlapped so that between the signal and pump SPP, the interaction is maximized. To distinguish stimulated emission from spontaneous emission, we study the pump-signal interaction in both continuous and pulsed mode. In the latter mode, both laser diodes are modulated such that there is no mode overlap between the pump and the signal SPPs. Only after the pump pulse has propagated and excited the active ions, the signal pulse is transmitted.

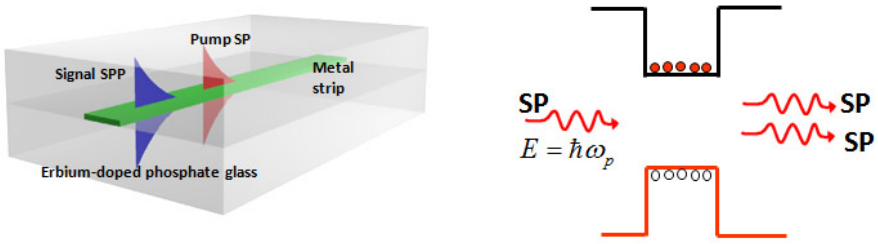

Figure 2.1: *Proposed configuration to study Stimulated Emission of Surface Plasmons.* a) thin metal strip embedded in Erbium doped phosphate glass for pump-probe experiments. b) The process of stimulated emission, pumping Surface Plasmons bring ions into excited states, before decaying into the ground state, a probe surface plasmon signal allows for stimulated emission studies.

To fabricate SPP waveguides, gold metal strips embedded in Er-doped glass, we use conventional top-down fabrication methods: Chemical Mechanical Polishing (CMP), photolithography, etching, deposition, and lift-off. Erbium-doped phosphate glass wafers (MM-2 laser glass, Kigre Inc.) with $\%4.2 Er_2O_3$ and $1\% Yb_2O_3$ are polished using chemical-mechanical process with CeO_2 slurry, resulting in flat surfaces with an rms of surface roughness of $\sim 0.5nm$. After a cleaning process, SPP waveguides of various widths are patterned into the glass wafer substrates by photolithography and transferred to the substrate by a dry-etching process; this depth of trench is characterized to be of $\sim 22nm$. Thin films of pure gold ($\sim 20nm$) and chromium ($\sim 2nm$) are then evaporated to fill the trenches (Cromium is used as an adhesion layer). After a lift-off process, SPP waveguides on Er-doped glass wafer are obtained. This wafer is diced into chips and these chips are thoroughly cleaned and bonded to non-patterned chips of similar size and of Er-doped glass. The solution used as a buffer is a sodium phosphate solution, which was centrifuged, filtered, and maintained at a pH value of ~ 7. The chip pairs were placed in a vacuum desiccator, and an additional heat treatment to improve the bonding strength of the chips. The bonded chips are diced one more time into different lengths. These last cuts are made flat across the metal waveguides in order to provide a good coupling to the fiber. The ending product results in SPP waveguides with erbium doped glass gain medium surrounding them; the substrate and the superstrate are well bonded, with a thin interlayer formed during low temperature bonding process. Figure 2.4 shows the ending interface after last dicing process.

We perform both, pulsed and continuous mode measurements with signal and pump lasers to find the features of SPP amplification by stimulated emission. The input fiber is aligned to the SPP waveguide as depicted in the Figure 2.2c y d, and the output from the waveguides is imaged onto an IR CCD using a 40 objective as can be seen in Figure 2.2b where the observed mode profile is pictured. The SPP nature of the propagating mode is guaranteed by observing the TM polarization dependence and sensitivity to misalignments

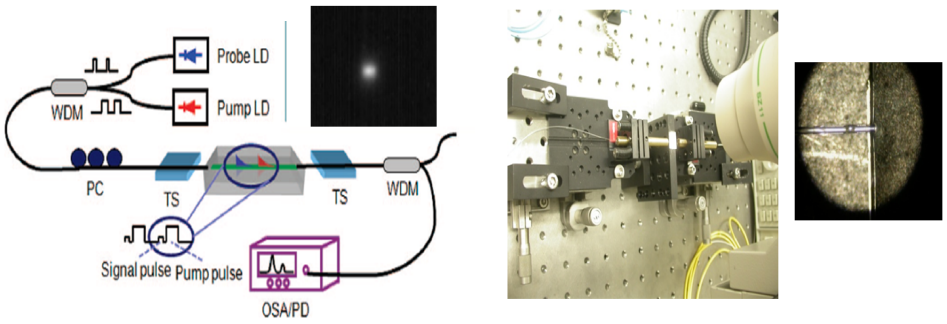

Figure 2.2: *Experimental set up for the study of stimulated emission of surface plasmons.* A) Pulsed and Continuous measurements setup. Pump and Probe diode lasers are combined using a WDM, polarization adjusted in order to maximize the polarization extinction ratio. (B) Plasmonic mode profile image of signal SPP acquired by an IR CCD camera.(C) Microscope for alignment of optical fibers to device under test. (D) Alignment (Top view) of device to fiber optics. The thickness of the metal strip is 22 nm and the width is 8 μm.

of the input fiber. The transmission of the plasmon waveguide is measured by an optical spectrum analyzer and a photodetector. The output fiber is aligned with the SPP waveguide so that the maximum output power and the strongest polarization extinction ratio ($> 20dB$) are obtained, ensuring with this the collection of the guided SPP mode only.

We measured the total insertion loss for the signal SPP mode without pump, and it is observed to be of 39 dB for an $8\mu m$ wide and 8 mm long SPP waveguide. The total insertion loss accounts for the passive waveguide loss, coupling loss between waveguide and fibers, and absorption loss by active Er ions (in the absence of pumping). The estimated passive waveguide loss is 27.5 dB (excluding the coupling and Er absorption losses). Passive waveguide loss includes both intrinsic loss in the metal and scattering loss. Scattering losses appear due to imperfections in the bonded interface, breaking locally the symmetry of the dielectric media surrounding the waveguide, which causes an increase of radiation and coupling losses. We probe the system in the small signal limit where gain is not depleted by the signal. The Er ions pumped with SPP mode use the same fiber-end coupling as the signal. The signal SPP stimulates the transition of the erbium ions from the upper ${}^4I^{13/2}$ manifold to the ground ${}^4I^{15/2}$ manifold, which results in stimulated emission, thus enhancing the SPP signal.

The dynamics of the stimulated emission of SPPs can be studied by modulating the injection current of the signal and pump lasers. We generate pump and signal square pulses, and measure the signal enhancements as a function of the pump power. The signal and pump pulse durations are of 150 and 500 μs with 1 ms period and with no overlap in the time domain. The time delay between the pump and signal pulse is of 30 μs, which is shorter than the lifetime, $\tau \sim 7.9ms$, of the excited-state of erbium ions. This ensures that the population of the excited state is maintained to interact with the signal SPP pulse. The signal pulses collected by the photodetector with increasing pump power are displayed in Figure 2.3a; the signal enhancement versus average pump power is plotted as well in

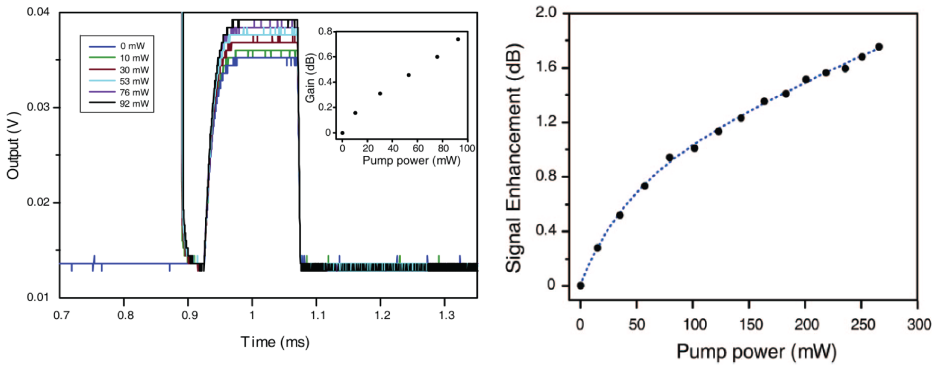

Figure 2.3: *Signal pulses at the photodetector with increasing power* and *Signal enhancement versus the average pump power* The maximum enhancement is less than the absorption of Er-doped glass at 1532 nm. The stimulated emission rate of signal SPP is smaller than the stimulated absorption rate.

Figure 2.3b. A key characteristic in Figure 2.3a is that the ground level of the signal remains unchanged even at the maximum average power of 92 mW. This confirms that the contribution of amplified spontaneous emission can be neglected as the possible source in the observed signal enhancement. The maximum signal enhancement in pulse mode is 0.74 dB (18%). In continuous wave mode, however, a maximum signal enhancement of $\sim 50\%(1.73dB)$ was recorded at a higher pump power of 266 mW (Figure 2.3b).

Even with the maximum average power, the maximum enhancement is still less than the absorption of Er-doped glass at 1532 nm, indicating that the stimulated emission rate of signal SPP is smaller than the stimulated absorption rate. The rapid decay of the pump power along the waveguide limits the enhancement to small values. Other factors such as imperfections in the bonded interface (as seen in Figure 2.4) and thermal effects may also affect the performance of the system. These thermal effects can emerge as optical pump energy is absorbed by erbium ions and as pump energy dissipated into heat due to ohmic losses in the metal. These thermal effects are dual: First, the optical gain is diminished due to the change in occupation probability density of each manifold depending on the Boltzmann distribution and the probability of occupation for the energy levels at the top of each manifold increasing with increasing temperature[179]. Second, metal loss due to increased electron scattering rates also increases; [180] theoretical calculations show that the change in passive propagation loss due to increased metal loss, and the gain diminished effects are partially responsible for the gain constraint at high pump powers. In addition to these thermal effects, the non-uniformity of the bonded interface along the SPP waveguide allows for varying local signal enhancements. By measuring different SPP waveguides, we suspect the bonding interface plays an important role in reducing these signal enhancements, however there is no easy way to experiment on the effects on signal enhancement. Although the signal enhancements seem to be small, saturation has not been reached as can be seen in

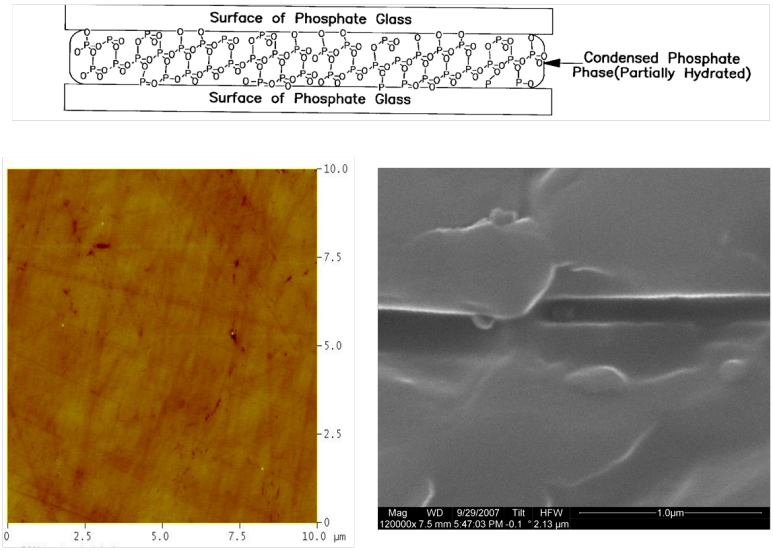

Figure 2.4: *Surface and cross-section of bonded Er-doped glass chips.* The chips are bonded with a thin bonding interlayer formed using condensed phosphate phase after a low temperature bonding process.(A) AFM Image of a CMP-ed surface of Erbium doped glass.(B)SEM image of the bonding interface layer, depicted in the cartoon above them

Figure 2.3b. There is room for further improvement by reducing the propagation loss down to a few dB/cm and thus ensure a slower decay of the pump and signal power.

We demonstrated a direct evidence of stimulated emission of surface plasmon polaritons. The system is appropriate for the study of dynamics of SPP amplification. A system capable of providing a symmetric dielectric environment surrounding the SPP waveguide, such as, polymers containing active rare-earth ions, could be implemented to overcome the metal losses and achieve SPP lasers with optical feedback mirrors or gratings. Systems like this described in this Section can be used for integrated optical devices. The coupling of a single emitter or an ensemble of emitters in the excited state to SPP mode can be also implemented, opening a route to new experiments in weak and strong coupling regimes.

2.3 Plasmonic Cavities

Devices capable of transporting or amplifying plasmon signals are of extreme importance for the development of the field due to the mentioned loss mechanisms. Just as important, other passive device is needed to better parameterize the quality of the guided excitation or to preserve signal coherency and better define its interaction with other signals or systems. This parameter is the quality factor of our excitation which, just as in acoustics, is studied by designing cavities for plasmonic modes to function as passive resonators.

Plasmonic resonant cavities exploit the field confinement to create ultrasmall-mode-

volume devices working for narrow band devices. This device is used to improve coherency in optical signals and thus guarantee clean interactions. The figure of merit of these structures is the ratio of cavity quality factor (Q), which is related to the dissipation rate of photons confined to the cavity, to the cavity mode volume (V)[197][198]. Plasmonic cavity Q factors have been limited to small values for the visible and the near-infrared wavelengths, smaller than the theoretically achievable Q factors for plasmonic resonant structures. [199] [200] [201] [202] [203]

Optical micro- and nanocavities made of dielectric or semiconducting materials exhibit high Q factors and small diffraction-limited cavity mode volumes. Metal-based counterparts (surface-plasmonic cavities) have been implemented for subwavelength-scale miniaturization, with results below theoretically expectations, especially in terms of cavity loss, set by ohmic losses in metals [199] [200] [201] [202] [203]. Losses are understood as the sum of loss contributions in surface scattering, radiation, finite cavity mirror reflectance or significant field penetration into the metal.

High-Q micro-cavity for Surface Plasmon Polaritons

In this section we describe the design and fabrication of a high-Q SPP whispering-gallery microcavity. This device is made by coating the surface of a high-Q silica micro resonator with a thin layer of a noble metal. Using this device, Q factors of $1,376 \pm 65$ were achieved in the near infrared for surface-plasmonic whispering-gallery modes at room temperature. This value is close to the theoretical metal-loss-limited Q factor (nearly ideal), and it is attributed to the suppression and minimization of radiation and scattering losses that are made possible by the geometrical structure and the fabrication method.

The whispering-gallery microcavity supports SPP eigenmodes, as well as dielectric eigenmodes, which can be accessed evanescently by using a single thread of a low loss, tapered optical waveguide [204][205] selectively exciting and probing confined SPP eigenmodes. This mechanism allows for coupling up to 49.7 per cent of input power by phase-matching control between the microcavity SPP and the tapered fibre eigenmodes. These seemingly different dielectric and plasmonic waveguiding principles can be combined in a single cavity by using mature optical microcavity technology such as that provided by disk [206][207] or toroidal microcavities [208]

Silica microdisk resonators are great templates for the study of surface-plasmonic whispering-gallery modes primarily because they routinely have optical Q factors bigger than 1,000,000 (larger than the metal-loss limited Q factor). Using wedge structures, Q factors as high as 6×10^7 have been experimentally obtained, showing a very low scattering loss value [206][40]. In addition, the extremely low photon loss rate and small cavity mode volume of whispering-gallery devices offer interesting physics, covering many areas of research including device physics, nonlinear optics and quantum optics [197][198].

The dielectric microcavity is engineered to minimize surface blemishes and thus reduce scattering. [206][207]. The proposed plasmonic microdisk cavity structure is pictured in Figure 2.5 The plasmonic cavity is composed of a core of silicon dioxide (disk microcavity)

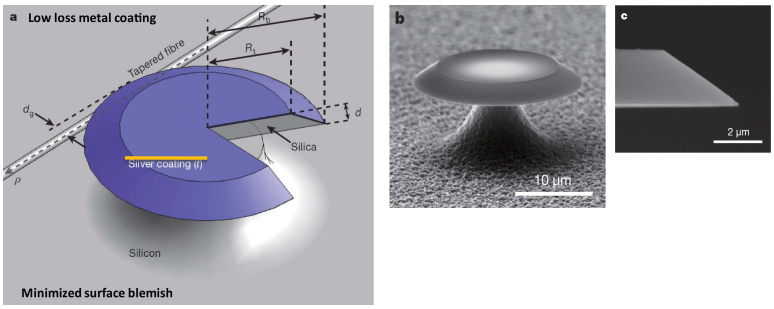

Figure 2.5: *Proposed plasmonic microdisk.* sp. A) Geometry of the microdisk and coupling mechanism. B) SEM picture of the resonator after Silver has been evaporated. C.) Expanded view of the wedge of the disk resonator.

and a thin layer of silver which is deposited using conventional evaporation methods. A scanning electron picture of a silver-coated SPP microdisk resonator is shown in Figure 2.5b, and the corresponding expanded view of the edge of the disk resonator is shown in Figure 2.5c.

Finite-element analysis was performed for the SPP resonators [209][210] taking into account the effects of silver [211] and silica[212]material dispersion. The calculated cavity mode dispersion diagram of an SPP microdisk resonator (Figure 2.6) shows the real part of the eigenfrequency, f, of the cavity modes as a function of an azimuthal mode number, m. The vacuum light line is defined by $f = \frac{mc}{2\pi n R_b}$ with respect to the bottom radius,R_b, of the silica disk microcavity, and the silica light line is defined by $f = \frac{mc}{2\pi n_{Silica}(f) R_b}$. The eigenmodes can be classified into two different categories depending on their cavity mode dispersion: (1) surface-plasmonic modes at the metal-dielectric interface and (2) optical dielectric modes due to the presence of the dielectric. In the insets of Figure 2.6a, the fundamental SPP eigenmode (first-order), the second-order SPP eigenmode and the fundamental dielectric eigenmode are plotted for magnetic energy density using a false-color map (a conventional cylindrical coordinate system (r, ϕ, z) is used for the analysis).

The SPP eigenmodes of an SPP microdisk resonator have electromagnetic energy-density profiles that peak at the silica-metal interface in the transverse plane (constant w). The SPP eigenmodes are categorized as $SPP_{q,m}$, where qm is the plasmonic mode number and the optical dielectric eigenmodes are denoted by $DE_{h,m}$, where hm is the dielectric mode number. The Plasmonic mode number is defined as the number of antinodes in $H_S PP^{q,m}$ along the silica-metal interface (excluding the vicinity of the sharp corner of the microcavity). Dispersion relations for the four lowest-order SPP eigenmodes (q=1, 2, 3, 4) and the two lowest-order dielectric eigenmodes (h=1, 2) are plotted in Figure 2.6a.

The cavity mode index,n_c, of a specific eigenmode can be evaluated with respect to the dielectric cavity edge $r = Rb$ as $n_c = mc/2R_b f$. Figure 2.6b shows the calculated mode index for modes SPP_{1m},SPP_{2m} and DE_{1m}. The mode index of a fundamental surface-plasmonic mode (SPP_{1m}) is clearly larger than that of a fundamental dielectric mode (DE_{1m}) within

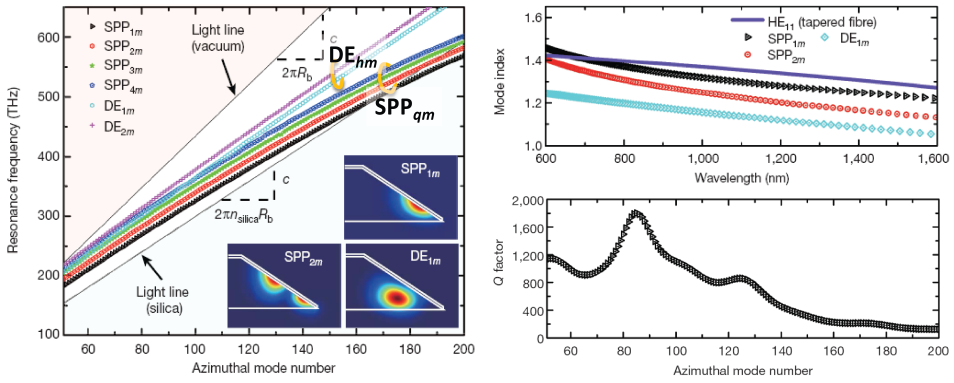

Figure 2.6: *Calculations of SPP microdisk resonator.* A) finite-element eigenfrequency analysis of cavity mode dispersions: the fundamental SPP eigenmode (first-order), the second-order SPP eigenmode and the fundamental dielectric eigenmode. Light lines, corresponding to vacuum and silica, are given as two black lines (silica material dispersion has been taken into account). The four lowest-order SPP eigenmodes and the two lowestorder dielectric eigenmodes are plotted. B)Effective cavity mode indices,nc, of $SPP_{1,m}$, $SPP_{2,m}$ and $DE_{1,m}$ (with respect to R_b), shown as a function of resonance wavelength. The mode index of a tapered-fibre HE11 mode is shown to demonstrate phase matching. C) Theoretical Q factor for $SPP_{1,m}$, plotted as a function of azimuthal mode number, m.

most of the visible and near-infrared frequency band, owing to the plasmonic surface-wave characteristics. The mode index is important because it determines the phase-matching condition for excitation of SPP modes by an input tapered fibre waveguide. After n_c has been calculated, the corresponding phase-matched fibre-waveguide mode index can be approximated as $n_w \approx n_c \frac{\sin^{-1}\sqrt{\delta(2-\delta)}}{\sqrt{\delta(2-\delta)}} = n_c(1 + 1/3 + 2/15^2 + O(g^3))$ where $\delta = \frac{-d_g}{R_b} \geq 0$ denotes the relative gap width. To qualitatively describe the effect of gap width variation on the phase matching, the HE_{11} mode index of a fibre waveguide with a $1 - \mu m$ waist diameter is shown in 2.6b. The fibre mode index is slightly larger than the SPP_{1m} mode index in the near-infrared wavelength band. However, owing to the above phase-matching formula, the SPP_{1m} eigenmode can be effectively phase-matched to the tapered-fibre eigenmode by increasing the relative gap width. We also note that the diameter of the tapered fibre can be optimized to phase match the cavity eigenmodes to the fibre eigenmode because the fibre diameter determines the mode index of the fibre eigenmode. The calculated cavity Q factors for SPP_{1m} eigenmodes as a function of azimuthal mode number, m, are plotted in Figure 2.6c. The error bounds for the imaginary part of the permittivity of Silver are taken into account in estimating the bounds on the theoretical Q factors and are discussed in [211]. The calculated Q factors consist of contributions from intrinsic metal loss (silica material loss is negligible in comparison with metal loss [209] [211] [212]) and the geometry and material dependent radiation loss into free space: $Q^{-1} = Q^{-1}_{metal} + Q^{-1}_{rad}$. Therefore, this Q

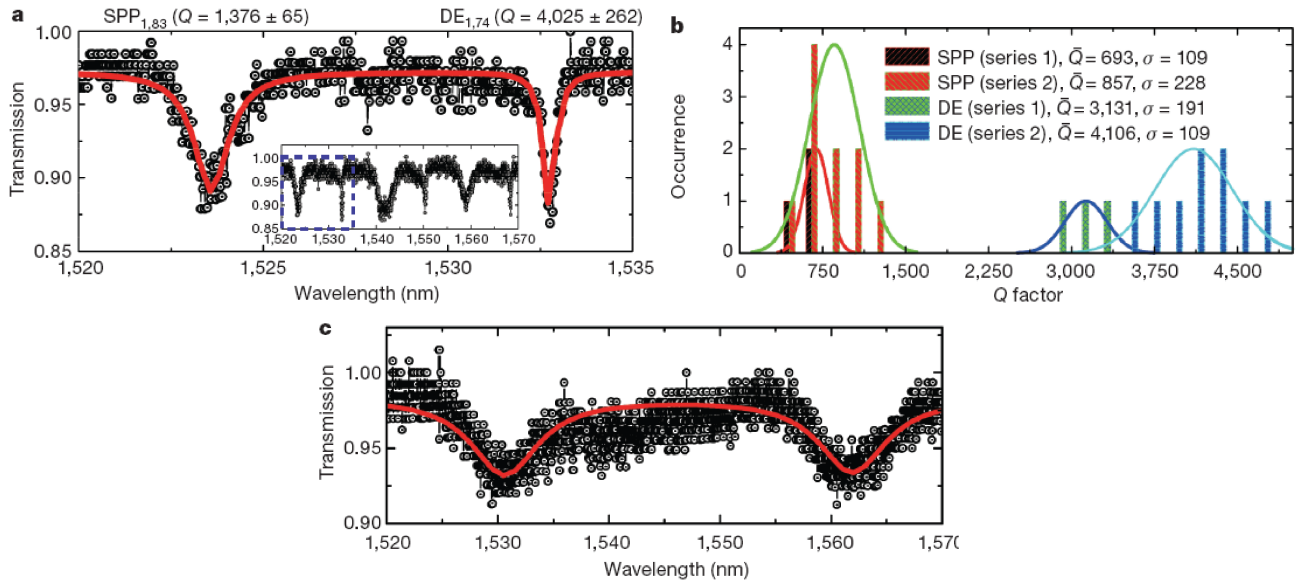

Figure 2.7: *Q-factor measurements for silver-coated and chromium-coated microdisk resonators.* A.) Normalized transmission spectrum showing the highest measured SPP Q factor of $1,376 \pm 65$ and a dielectric resonance with a Q factor of $4,025 \pm 262$. The inset (main panel outlined) is the entire wavelength band (1,520-1,570 nm) scanned for this sample. $R_b = 15.450.05\mu m$, $R_t = 12.730.04\mu m$, $d = 2\mu m$, $t \approx 100nm$. B.) Statistical histogram of measured Q values showing the occurrence of each eigenmode (SPP and dielectric) for two different sample batches (series 1 and series 2). Mean $\overline{Q}$ and standard deviation (σ) of Q factors are shown in the key (series 1, n=3 measurements; series 2, n=9). C.) Normalized transmission spectrum for a chromium-coated microdisk resonator ($R_b \approx 11\mu m$, $R_t \approx 7.9\mu m$ $d \approx 2\mu m$) with a two-dip Lorentzian fit.

value provides the ideal theoretical limit on the Q performance of SPP microdisk resonators that have negligible scattering loss induced by surface roughness. The radiation-limited Q factor, Q_{rad}, is orders of magnitude larger than the metal-loss-limited Q factor, Q_{metal}; the ideal SPP microcavity is thus metal-loss limited: $Q^{-1} = Q^{-1}_{metal}$. In Figure 2.6c, the highest fundamental SPPQ factor is found to be 1,800, at the resonant wavelength of 1,062.45 nm (m=85). At a wavelength of 1,568.25 nm (m=54), which is close to the value used in measurements described below (series 1 in Figure 2.7), the theoretical Q factor is 1,140. The cavity mode volume, V, and the figure of merit $fracQv$ of the SPP microcavity are estimated in more detail in the supplementary information of reference

The template silica microdisks are fabricated by photolithography and buffered oxide etching as described elsewhere [189][189]. During the wet etch, the photoresist is undercut and produces a beveled silica edge, which provides for conformal silver coating of the top surface of the microdisk. The silver coating is deposited on the template silica microdisks using a D.C. sputtering technique (Edwards 360) with a chamber argon pressure of 30 mTorr

and Power of 100 Watts. Two batches of samples (series 1 and 2) are prepared in this way to investigate the size-dependent characteristics of SPP microcavities.

To measure the SPP microdisk resonances experimentally, a narrow linewidth (¡300 kHz) a tunable external-cavity semiconductor laser is coupled to the tapered fibre waveguide and scanned over the 1,520- 1,570-nm wavelength range. The position of the tapered fibre with respect to the SPP microdisk resonator is controlled at a fixed vertical distance by piezoelectric stages with an encoded resolution of 100 nm, and the laser polarization is controlled using a fibre polarization controller and monitored with a polarimeter. For large overlap between the cavity and the waveguide modes, the tapered fibre is positioned underneath the beveled edge of the resonator, where the silica microdisk is free of silver coating. The output transmission is recorded using a photodetector and a digital oscilloscope. Figure 2.7a shows the normalized transmission spectrum from an SPP microdisk resonator with a Lorentzian line-shape fit (red curve) to each resonance. Two resonances, located at 1,523.59 and 1,532.76 nm ($SPP_{1,83}$ and $DE_{1,74}$ as estimated by calculation), can be clearly identified. An expanded view of the scan (main panel modes outlined) is shown in the inset of Figure 2.7a and spans three free spectral ranges of SPP and dielectric eigenmodes. The cavity Q factor for the fundamental $SPP_{1,83}$ eigenmode is found to be 1,376665 (which falls within the theoretical Q-factor range of $760 \leq\sim Q \leq\sim 2,360$, with a nominal Q factor of 1,225 for the $SPP_{1,83}$ eigenmode), and that of the fundamental $DE_{1,74}$ mode is 4,0256262. This SPP Q factor of 1,376 is over 30 times larger than the Q factors reported in previous SPP cavity work [199] [200] [201] [202] [203].

The demonstration of high-Q surface-plasmonic microcavities opens many possibilities for applications in fields ranging from fundamental science to device engineering. As a specific example, it could make possible a plasmonic laser, for which adequate gain materials as well as a high-Q SPP cavity are key prerequisites [189]. Although the demonstrated SPP Q factor is still less than that of an optical micro- or nanocavity [197][198] the corresponding SPP loss coefficient of $\alpha_{SPP} \approx \frac{2\pi n_c}{\lambda Q_{SPP}} \approx 39cm^{-1}$ (where λ is the wavelength) satisfies the experimental criteria for a laser cavity and shows that, in principle, such surface-plasmonic lasing devices are possible. The tapered-fibre excitation scheme also demonstrates a convenient means of exciting these structures and selectively probing SPP cavity modes; because it directly controls the mode overlap and phase matching between the cavity and fibre eigenmodes. We also note that coupling to a conventional, chip-based waveguide is possible [215]

Furthermore, it is notable that the SPP Q factor could be substantially increased beyond the values measured here by lowering the temperature of the SPP microcavity [214][216]. From a fundamental standpoint, the SPP Q factor is sufficient to observe interesting cavity quantum electrodynamical phenomena in the weak-coupling regime relating to enhanced Purcell factors [198] [216] [217]. In addition, using the high nonlinearity of metal (or materials deposited in the vicinity of the metal), it may be possible to extend the applications of nonlinear plasmonics.

2.4 Plasmonic Metamaterials

As previously introduced in Chapter 1, metamaterials are artificially engineered structures that can have properties unattainable by natural materials. One of those fundamental properties is the refractive index of materials Negative-index metamaterials (NIMs) [219] [220] [221] [222], first demonstrated for microwave frequencies [223] [224], have been challenging to design for optical frequencies because of significant fabrication challenges and strong energy dissipation in metals [225] [226]. Such thin structures are analogous to a monolayer of atoms in a surface, which makes difficult to assign bulk properties such as the index of refraction.

Negative refraction of surface plasmons was recently demonstrated but confined to a two-dimensional waveguide [227]. Three-dimensional (3D) optical metamaterials have come into focus recently, including the realization of negative refraction by using layered semiconductor metamaterials and a 3D magnetic metamaterial in the infrared frequencies; however, neither of these had a negative index of refraction [228] [229]. In this section we report a 3D optical metamaterial having negative refractive index with a very high figure of merit of 3.5 (that is, lowloss). This metamaterial is made of cascaded 'fishnet' structures, with a negative index existing over a broad spectral range. Moreover, it can readily be probed from free space, making it functional for optical devices. We construct a prism made of this optical NIM to demonstrate negative refractive index at optical frequencies, resulting unambiguously from the negative phase evolution of the wave propagating inside the metamaterial. Bulk optical metamaterials open up prospects for studies of 3D optical effects and applications associated with NIMs and zero-index materials such as reversed Doppler effect, superlenses, optical tunneling devices [230][231], compact resonators and highly directional sources[232].

In addition, we present the first study of plasmonic diabolic point and deep sub-wavelength surface states in binary metallodielectric lattice. The lattice is formed by a hybrid of alternating normal and anomalous coupling. We show formation of a singularity (diabolic point) in two-band structure and conical-like diffraction around the singular point. Moreover, when breaking either the normal or anomalous coupling results in deep sub-wavelength surface waves which manifest as strongly confined plasmonic Tamm and Shockley states. Such surface states provide of unique features originating from the hybrid coupling between plasmon modes. Together with strong diffraction anomalies arising from plasmonic diabolic point, such novel surface states could provide a means to control signal routing in nano-scale optical circuits.

Three-dimensional Optical metamaterial with negative refractive index

Negative-Index Metamaterials (NIMs) were first described by Veselago more than 40 years ago [219] and recently discussed in the framework of metamaterials [220], they arise from the fact that both the permittivity and the permeability of the materials are simultaneously negative . In the past several years, much effort has been dedicated to the engineering and extension of the functionalities of metamaterials at terahertz frequencies [233] [234] [235]

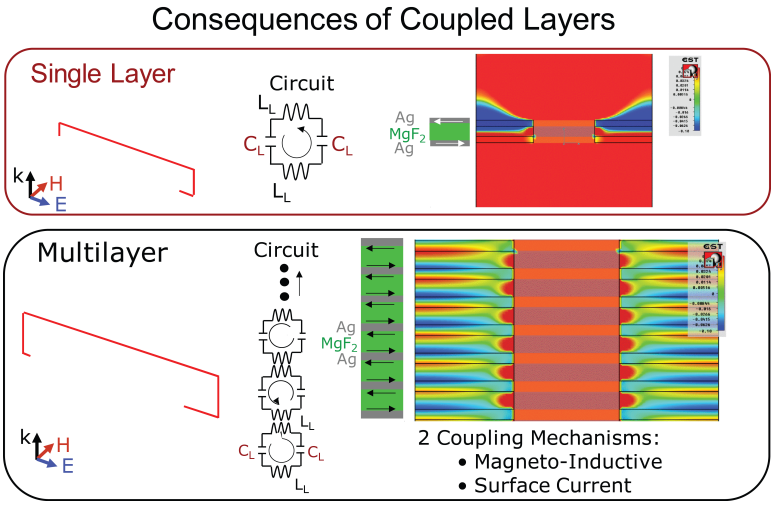

Figure 2.8: *Simulation of Fishnet metamaterial.* As a consequence of induced currents and magneto-inductive mechanisms, single layers (modeled as LC circuits) are coupled to effectively reduce (as increased in number) the group velocity of the wave of light at specified wavelength range propagates through the layers.

and optical frequencies [225] [226] [228] [236] [237] [238] [239]. Metal-dielectric-metal fishnet structures were among the earliest demonstrations of optical NIMs. These structures, however, consist of a single functional layer along the direction of propagation. This is equivalent to an atomic monolayer, making it difficult to explore phenomena in three dimensions and develop device applications. Moreover, as a result of their resonant nature, these systems suffer substantial loss at optical frequencies. On the basis of the above, it is therefore imperative to realize low-loss bulk optical NIMs if we are to demonstrate unambiguously the unique effects associated with negative index of refraction.

Recently, it has been suggested theoretically that stacking up multiple fishnet functional layers along the propagation direction constitutes a promising approach for achieving a 3D optical NIM [240]. This cascading leads to a strong magneto-inductive coupling between neighboring functional layers[241]. As demonstrated recently [242], the tight coupling between adjacent LC resonators through mutual inductance results in a broadband negative index of refraction with low loss, which is similar to the material response of left-handed transmission lines [243] [244]. Figure 2.8 shows the simulation of the magneto-inductive mechanisms and induced currents coupled to reduce the group velocity of propagating light in the incident wavelength range.

In addition, the loss is further reduced owing to the destructive interference of the anti-symmetric currents across the metal film, effectively cancelling out the current flow in the centre of the film [241]. Here we experimentally demonstrate the first 3D optical NIM by directly measuring the angle of refraction from a prism made of cascaded fishnet metamaterial. The experimental results, along with numerical calculations, serve as direct evidence

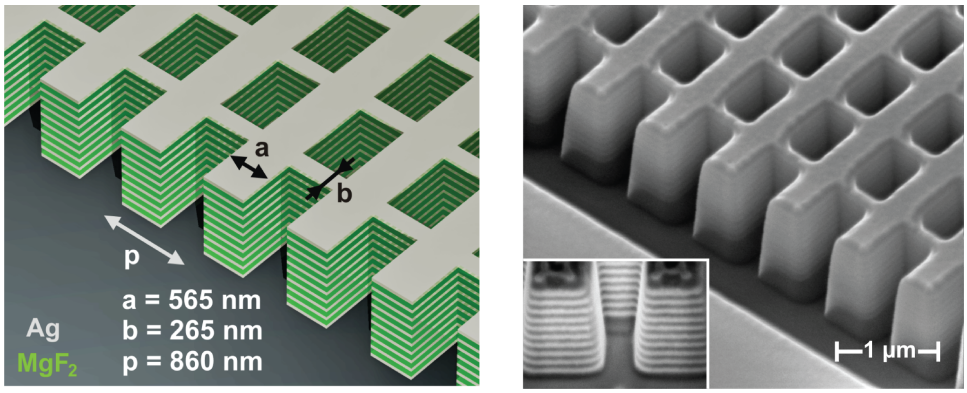

Figure 2.9: *Fishnet metamaterial.* A.) Diagram of the 21-layer fishnet structure. B.) SEM image of the 21-layer fishnet structure with the side etched, showing the cross-section. The structure consists of 21 alternating layers of 30 nm silver (Ag) and 50 nm magnesium fluoride (MgF2). The inset shows a cross-section of the pattern taken at a 45 angle. .

of zero and negative phase index in the metamaterial.

As shown in figure 2.9a the 3D fishnet metamaterial is fabricated on a multilayer metaldi-electric stack deposited as 21 films of alternated Silver and Mangnesium Fluorisde e-beam evaporated thin films (10 functional layers). Then after, we programed a focused ion-beam milling (FIB) system, capable of cutting nanometre-sized features with a high aspect ratio. Figure 2.9b shows the scanning electron microscopy (SEM) image of the proposed 3D fishnet pattern.

To measure the index of refraction of the 3D metamaterial experimentally, a prism was created in the multilayer stack (Figure 2.10a,b). Measurements of the refractive index of these structures were performed by observing the refractive angle of light passing through the prism by Snell's law. This provides a direct and unambiguous determination of the refractive index, because the refraction angle depends solely on the phase gradient that the light beam experiences when refracted from the angled output face. We used a femtosecond synchronously pumped optical parametric oscillator as a tunable light source to determine the refractive index at different wavelengths. The beam was focused on the sample, and a charge-coupled device (CCD) camera was placed in the Fourier plane (Figure 2.10).

The beam shift δ resulting from the bending of light at the prism output at different wavelengths, ranging from 1,200 to 1,700 nm, is shown in figure 2.10b and figure 2.11. The measurement was performed on a prism of angle 5.0° and the beam shift is plotted along with reference measurements of transmission through a window, without the presence of the prism (left panel). Clearly, as the wavelength increases, the beam shift resulting from the prism refraction is changing from positive to negative, indicating a transition from a positive index in the shorter wavelengths to a negative index in the longer wavelengths. At a wavelength l of 1,475 nm, the index of refraction is approaching zero; that is, the beam does not acquire any phase while propagating in the metamaterial. Consequently there is

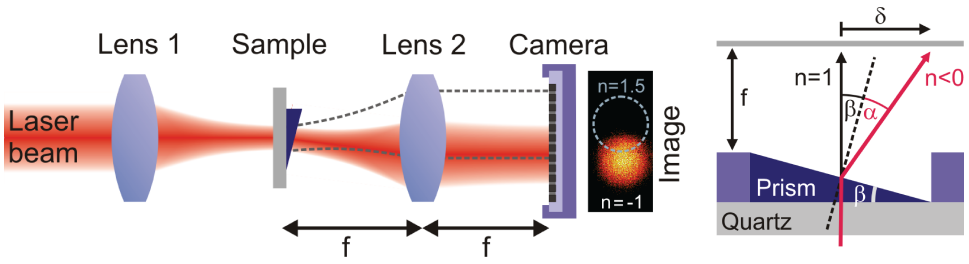

Figure 2.10: *Measurement of the index of refraction of a prism made out of 3D Fishnet metamaterial.* A.) Simple Snell's Law arrangement for free space light propagation test. B.) Geometry diagram of the angle measurement by observing the refraction angle of light passing through the prism. C.) Experimental setup for the beam refraction measurement.

no phase gradient at the angled output face and the exiting beam is exactly normal to the output face (see dashed lines in Figs 2.10 and 2.11a.

Figure 2.11b depicts the measured refractive index of the 3D fishnet metamaterial at various wavelengths. The refractive index varies from n = 0.630.05 at 1,200nm to n=-1.230.34 at 1,775 nm. The refractive index was determined from multiple measurements of two fishnet prisms with angles of $\beta = 5.0°$ and 4.7° and for wavelengths ranging from 1,200 to 1,800 nm. Although there is a correlation between the beam spot positions shown in Figure 2.10 and the refractive index, it should be noted that Figure 2.11 shows the average of measurements on different prisms with the standard deviation as error bars, whereas Figure 2.11a shows an individual measurement. The experimental results are found to be in good agreement with the theoretical predictions (black line in Figure 2.11b on the basis of rigorous coupled-wave analysis (RCWA). The measured negative refraction angle is a direct result of negative phase evolution for light propagating inside the sample caused by a negative refractive index. This is illustrated in Figure 2.11b by a numerical calculation of the in-plane electromagnetic field distribution in the fishnet prism at $\lambda = 1,763nm$, where the structure shows a refractive index of n=-1.4. In the numerical studies of the 3D fishnet metamaterial, the intrinsic losses of the metal are included. The multilayer stack was deposited by electron-beam evaporation of alternating layers of Silver (30 nm) and magnesium fluoride (50 nm) resulting in a total thickness of 830 nm. Two different configurations of the fishnet samples were fabricated on the multilayer stack. Samples of the first configuration consist of 22×22 in-plane fishnet unit cells and were used for the characterization of the transmittance. The second configuration (prism sample) was formed by etching the film at an angle β to the film surface, using FIB. The exact angle was measured with an atomic force microscope and was found to vary slightly between samples. A 10×10 fishnet pattern was subsequently milled in the prism.

To obtain the absolute angle of refraction, a window with an area equal to that of the prism was etched through the multilayer stack to serve as a reference. The window and prism Fourier images were measured for all wavelengths on an indium gallium arsenide infrared

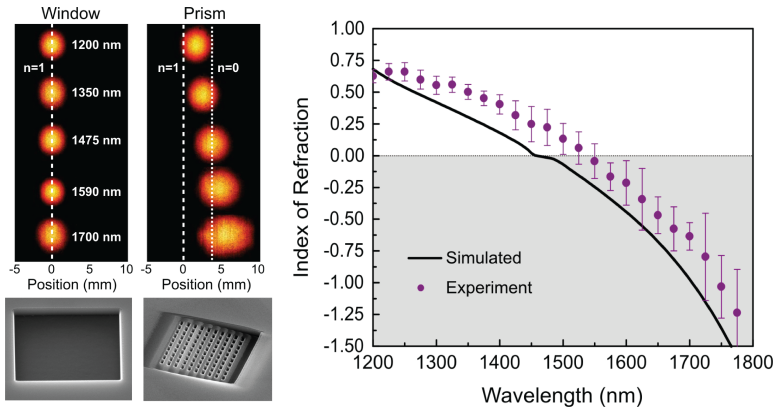

Figure 2.11: *Experimental Results and Simulations of the 3D Fishnet metamaterial.*Fourier-plane images of the beam for the window and prism sample for various wavelengths. The horizontal axis corresponds to the beam shift δ and positions of n = 1 and n = 0 are denoted by the white lines. The image intensity for each wavelength has been normalized for clarity. Measurements and simulation of the fishnet refractive index. The circles show the results of the experimental measurement with error bars (s.d., N = 4 measurements). The measurement agrees closely with the simulated refractive index using the RCWA method (black line). FIB-fabricated prism of fishnet metamaterial compared to its absence (window) SEM image of the fabricated 3D fishnet NIM prism. The inset shows a magnified view with the film layers visible in each hole.

camera and the total beam shift δ of the spot center was calculated. Consequently, the angle of refraction α at the surface of the prism is given as $\alpha = \beta - \arctan(\frac{\delta}{f_2})$. Snell's law ($n = \frac{sin\alpha}{/sin\beta}$) was used to calculate the real part of the refractive index of the sample. The imaginary part of the refractive index of the sample was obtained from transmittance and reflectance data acquired with a 21-layer sample of the first configuration (as described above)

Because of the negative phase propagation inside the metamaterial, the electromagnetic wave emerging from the thicker part of the prism experiences phase advance compared with that passing through the thinner parts, causing the light to bend in the negative direction at the exit interface. We note that the refractive index remains consistent for the fishnet metamaterial with three or more functional layers along the propagation direction, which leads to a uniform wavefront exiting from the prism.

To acquire a clear understanding of the 3D metamaterial's optical response, we separate the fishnet into two subsets and calculate the dispersion curves with RCWA. The first constituent is a 3D array of metal wires aligned with the polarization direction of the incident electric field (Figure 2.12a). This array serves as an effective medium with lowered volumetric plasma frequency (220 THz), below which wave propagation is not allowed because of negative effective permittivity. The second constituent is a 3D array of metal strips along the

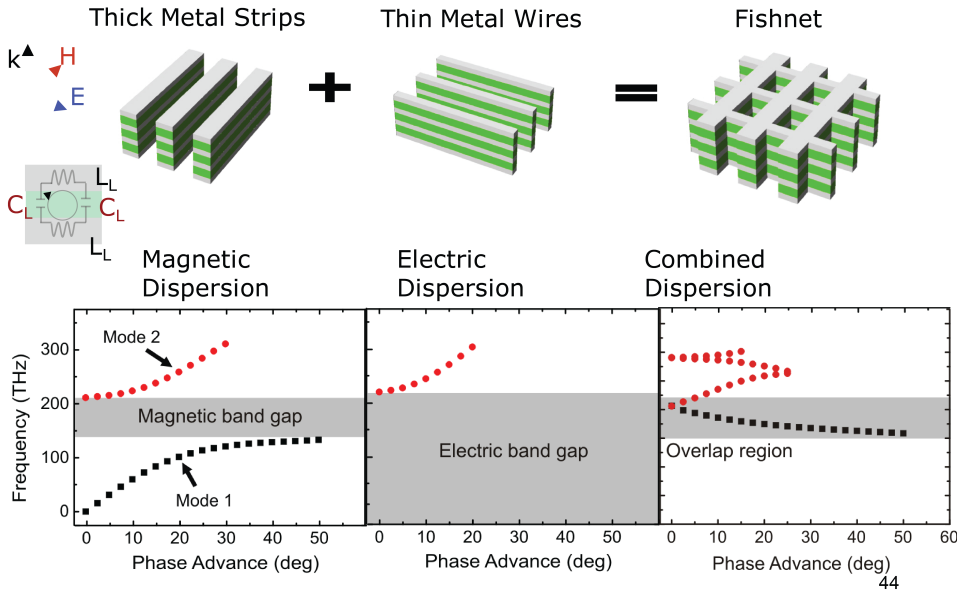

Figure 2.12: *Fishnet metamaterial.* A,Dispersion Relations: Magnetic dispersion, Electric dispersion. Combined Dispersion. In all plots the grey area corresponds to the negative-index region as determined by simulations. B, Dispersion relation for a 3D array of metal wires aligned along the electric field E, where k denotes the incident propagation vector. The dotted lines in the diagram mark the unit cell size. Dispersion relation of a 3D array of metal strips along the magnetic field H. C, The dispersion for the 3D fishnet structure. A dispersion curve with negative slope appears within the overlapped region of the electric bandgap and magnetic bandgap if both structures are combined.

direction of the magnetic field (Figure 2.12b.), in which induced antisymmetric conductive currents across the dielectric layers give rise to a magnetic bandgap between 135 and 210 THz. This is further confirmed by the plots of the magnetic fields at two frequencies, below and above the bandgap. Above the bandgap the magnetic response is positive, as shown in Figure 2.12a, where the magnetic field component between the strips is in phase with the external field. Above the bandgap, the metal strips have a moderately negative response, as shown in Figure 2.12b, where the magnetic field between the strips is out of phase. Finally, these two structures are merged to form the 3D fishnet metamaterial, for which the dispersion relation is shown in Figure 2.12c. A propagation band with negative slope appears in the overlapped region of the forbidden gaps of both electric and magnetic media, demonstrating that the negative-index behavior in the 3D cascaded fishnet does indeed result from the fact that both the electric permittivity and the magnetic permeability are negative.

In addition, transmittance measurements were performed on the 3D fishnet metamaterial made of 21 layers with the use of a Fourier transform infrared microscope (Nicolet Nic-Plan IR microscope). . The simulation predicts a broad negative-index band spanning from $1.45\mu m$ to $2.2\mu m$ (shaded region), which coincides with the high transmission band from

$1.5\mu m$ to $1.8\mu m$. As mentioned previously, this wide band of negative index results from the strong coupling between neighboring layers. The measured transmittance has similar features to those of the calculation, namely two peaks imposed over the transmission band that are slightly red-shifted with respect to the numerical results. These features are due to the Fabry-Perot effect, in which the impedance mismatch leads to reflectance at the metamaterial/air and metamaterial/glass interfaces. Although the peaks are visible at lower refractive index values owing to the lower loss, the Fabry-Perot effect cannot be clearly seen in the transmission spectra for larger negative index at longer wavelength where the loss is higher, resulting in broadening and extinction of spectral features. We note that the transmittance in the negative-index band is one-quarter of the numerically calculated value, which is probably due to imperfections in the fabrication. Nevertheless, our simulations show that the presence of loss in the coupled fishnet metamaterial has a minimal impact on the dispersion relation (see Supplementary Information). This is because the 3D fishnet structure operates far from the band edge (Figure 2.12c), where resonance is not significant. This explains the good agreement between the experimentally measured and simulated refractive indices despite the fabrication imperfections.

The fishnet metamaterial has a period about $\lambda/20$ in the vertical direction. The propagation of light travelling along this direction or within some angular range is dominated by this deep sub-wavelength period and not by the in-plane period, as long as the wavevector projection on the in-plane directions is small compared with the in-plane reciprocal lattice vector of the fishnet metamaterial. There is only a single propagating mode in the negative-index frequency region, justifying the description of the fishnet metamaterial with an effective index. In contrast, if higher dielectric materials such as silicon ($n \approx 3.6$) are used to serve as the dielectric layer, the ratio between the wavelength and in-plane period can be significantly increased because of the larger capacitance in the LC circuit.

Unlike the negative index obtained from photonic crystals [247], the negative index presented here results from simultaneous negative magnetic and electric responses and shows a resemblance to the left-handed transmission line due to the tight coupling between the adjacent LC resonators. The negative index occurs in the first propagation band and with smooth negative-phase evolution along the light propagation direction, which differs from the negative refraction obtained in photonic crystals. Here we have experimentally demonstrated the first 3D NIM at optical frequencies and directly measured the refractive index of a NIM prism in the free space. The 3D optical metamaterials may offer the possibility to explore a large variety of optical phenomena associated with zero and negative refractive index, as well as applications in the scaling down of photonics and imaging.

Deep subwavelenght surface states in metal-dielectric metamaterials

Recent studies on the dynamics of light propagation in sub-wavelength metallodielectric arrays show strong optical anomalies such as those seen in the last section for the negative

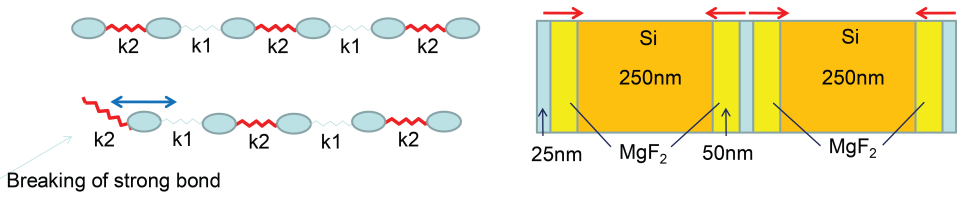

Figure 2.13: *Deep sub-wavelength surface states in binary metallodielectric lattice.* Surface states manifest unique features originating from the hybrid coupling between plasmon modes metamaterial. Low-dielectric (MgF2) and high dielectric (Si) waveguides coupling is modeled as weak and strong springs among nearest massive neighbors (waveguides)

refraction, or subwavelength solitons, and subwavelength focusing [251] [252] [253] [254] [255]. It was revealed that such arrays possess unique dispersion properties due to anomalous coupling [252][256] and can surpass the fundamental diffraction limit due to the plasmonic nature of the lattice. This new toolset for controlling light dynamics can be further extended by introducing multi-band periodic structures, as done with binary dielectric waveguide arrays [257] [258]. Metallodielectric arrays having a multi-band structure can bring richer dynamics through the combination of normal and anomalous waveguide coupling, which is not available for conventional dielectric waveguide arrays [252][253]. Band crossing of iso-frequency surfaces in k-space is of particular interest in the study of multi-band structures, for its analogy to degeneracy in potential energy surfaces, known as conical intersection in quantum chemistry [259]. In optics, this phenomenon has important implications as well, such as the diffraction catastrophes [260]. Moreover, by breaking the periodicity of such arrays, intriguing surface physics analogous to periodic lattice termination of solid state crystal, can be studied in a controlled environment. This is not only a main research topic in condensed matter and surface science, but also plays an important role in the fields of nano-science and engineering due to the large surface-to-volume ratio. For instance, surface defect states in semiconductor nanocrystals make a major impact on their photoluminescence [261] and lattice termination in graphene monolayers into nanoribbons to create intriguing band structures [262]. Optical analogue of the surface states also have been addressed in photonic lattice systems such as photonic crystals [263] [264] [265] and periodic array of optical waveguides [258] [266] [267]. Such optical surface states have provided new approaches to photon manipulation. In this section, we present the first study of plasmonic diabolic point and deep sub-wavelength surface states in binary metallodielectric lattice. Such surface states manifest unique features originating from the hybrid coupling between plasmon modes. We show diffraction of hybrid surface plasmon polaritons near a singularity at the intersection of dispersion curves and analyze the existence conditions of the surface states.

We begin by analyzing a 1D binary array of single mode waveguides with alternating normal and anomalous coupling as shown in Figure 2.13(a). Each waveguide (blue bar) is evanescently coupled to its nearest neighbors with alternating sign of the coupling coefficients, C_+ and, C_- defined by $C = (\beta_s - \beta_a)/2$, where β_s and β_a are the propagation constants (the

wave-vector components in the propagation direction), of the symmetric and antisymmetric modes of a coupled waveguide system, respectively. Depending on its sign, the coupling is 'normal' ($C_+ > 0$) or 'anomalous' ($C_- < 0$) [252] [256]. The anomalous coupling can be achieved by coupling through a metal layer in metallodielectric waveguides [251] [252] [253] [254] [255] or coupling between photonic crystal waveguides [256]. This is in sharp contrast with normal coupling between two conventional dielectric waveguides based on total internal reflection. For the array in Figure 2.14a, an approximated band structure in the propagation constants can be found by applying the coupled mode theory considering only nearest neighbor interaction, which simplifies into the Hamiltonian equations 2.1

$$H|\psi\rangle = K|\psi\rangle, H(\eta,\kappa) = \begin{pmatrix} 0 & \eta e^{-i\kappa}+1 \\ \eta e^{i\kappa}+1 & 0 \end{pmatrix}, |\psi\rangle = \begin{pmatrix} A \\ B \end{pmatrix} \tag{2.1}$$

where we used Floquet-Bloch eigenmodes, $a_n = Aexp(i\beta z + i\kappa n)$ for E_{2n} and $b_n = Bexp(i\beta z + i\kappa n)$ for E_{2n+1}, κ is normalized Bloch vector, E_n is the field amplitude of the nth waveguide, β_0 is the propagation constant of single isolated waveguide, $K = \frac{(\beta-\beta_0)}{C_+}$ is the dimensionless propagation constant, and asymmetry coefficient $\eta = \frac{C_-}{C_+}$, which takes negative values for the hybrid coupling. The Hamiltonian H is Hermitian for real η and κ and has real eigenvalue K. By solving the equations, we obtain the diffraction relation $K_\pm(\eta,\kappa) = \pm\sqrt{\eta^2 + 2\eta cos\kappa + 1}$ where each sign corresponds to the upper and lower band, respectively, as shown in Figure 2.14(b). Interestingly, the diffraction curves for negative $\eta = -0.5$ (hybrid coupling, solid lines) are inverted compared to positive $\eta = 0.5$ (dotted lines). Namely, the narrowest band gap occurs at $\kappa = 0$, and not at $\kappa = \pm\pi$ as normally occurs for conventional periodic structures [268]. The second derivative $D = \frac{d^2K}{d\kappa^2}$, indicating diffraction spreading is also plotted for each band in Figure 2.14(b), having opposite properties. The corresponding symmetries of the eigenvectors at the band edges are also shown in Figure 2.14(c) for $-1 < \eta < 0$ (hybrid coupling and direct bandgap).

The unique features of the inverted two band structure become more prominent when η gets close to -1. As shown in Figure 2.15(a), the band structure appears as a double-cone shape around $\kappa = 0$ and $\eta = -1$ in $\kappa - \eta$ space with degeneracy, which generically occurs in a family of Hamiltonians labeled by at least two parameters [269]. The singularity is referred as 'diabolical point', at which the direction of group velocity is not uniquely defined [270] [20]. This band crossing is also a common phenomenon for Hermitian quantum systems. For instance, the conduction and the valence band of graphene; a monolayer of honeycomb carbon lattice having unusual transport properties, where the linear dispersion relationship ($E = \pm\hbar\nu|k|$) results in 'massless' electrons [271]. The 'massless' fermions in graphene are analogous to 'diffractionless' surface plasmon polaritons for the considered structure with hybrid coupling for wide range of κ. This analogy is reflected in the similarity between Hamiltonian in Equation 2.1 and that in reference [271]. Around the diabolic point, the propagation dynamics of surface plasmon polariton modes exhibit 2-D conical-like diffraction analogous to those of Hamilton's conical diffraction due to a k-space singularity. However, unlike Hamilton's conical diffraction which originates from polarization, the

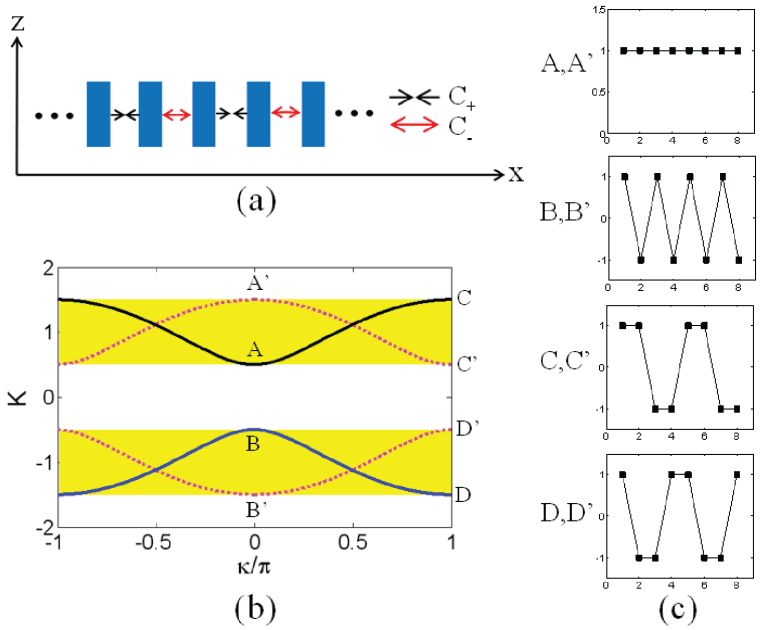

Figure 2.14: *Hybrid coupling among waveguides* . (a) Schematic of waveguide arrays with alternating hybrid coupling $C_+ > 0$ and $C_- < 0$. (b) Band diagram of normalized propagation constant K and diffraction D for asymmetry coefficient . solid line: , dotted line: . (c) The corresponding eigenvectors at the band edges A, B, C, and D in (b).

diabolic point with the array of hybrid coupling is solely due to lattice symmetry, alternating normal and anomalous coupling with equal coupling strength. The conical diffraction due to lattice symmetry was demonstrated only in honeycomb photonic lattices mimicking graphene structure [270][20].

An inverted dual-band array can be realized using a unit cell consisting of four layers: metal, low index dielectric, high index dielectric, low index dielectric. The structure shown in Figure 2.13 consists of 8nm gold, 50nm MgF2 with refractive index of 1.34, 200nm of Si with index of 3.48, and 50nm layer of MgF_2. The wavelength in this study is 1550nm. For single unit cell with infinite thickness of outer layers, the electric field (E_x) of the mode is highly confined in the 50nm ($\sim \lambda/30$) low index dielectric layer forming hybrid surface plasmon polariton mode [272]. The alternating hybrid coupling in the array is realized by anomalous coupling through 8nm gold layer and normal coupling through the 200nm silicon layer. For the given parameters, the corresponding band structure is plotted in Figure 2.14(c) showing almost linear diffraction curves in wide range of κ and the diabolic point at $\kappa = 0$. A slight deviation from the symmetry of the bands as predicted by the coupled mode theory (Figure 2.14(a)) is due to the strong coupling between the waveguide modes. Figure 2.14(b) shows the propagation of hybrid surface plasmon modes excited by a normally incident Gaussian beam, which clearly demonstrates characteristic conical diffraction in 2-

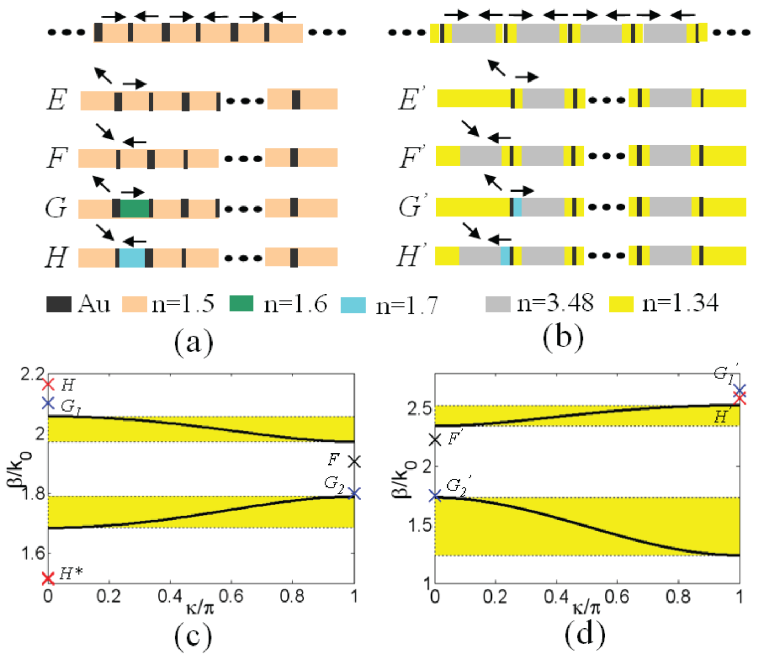

Figure 2.15: *Band diagram calculation and numerical simulations.* (a) Band diagram of normalized propagation constant K in space. At , the band crossing occurs. At exact , the two bands collapse to one band. (b) Numerically simulated propagation of normally incident Gaussian beam to the metallodielectric array. The electric field intensity is normalized the intensity maximum. The unit cell parameters of the array are Au (8nm)/MgF2 (50nm, n=1.34)/Si (200nm, n=3.48)/MgF2 (50nm, n=1.34) at the wavelength of 1550nm. (c) The corresponding band structure for the array in (b) .

D form near the diabolic point. The metal loss was discarded here for better visibility of propagation. The hybrid surface plasmon modes propagate as a cross section of ring shape with nearly constant thickness and increasing radius, which is in a sharp contrast to discrete diffraction in conventional arrays (see e.g., Figure 2(e) in reference [253]).

Notwithstanding the interest in peculiar properties associated with infinite waveguide arrays with hybrid coupling, finite waveguide arrays exhibit even more fascinating phenomena where the termination of the periodic chain of couplings creates a 'surface' between the array and an external dielectric. As in the case of solid state, this surface may support localized eigenmodes, known as surface states. Surface states in solid state crystals with discrete electronic energy levels are formed either by perturbing the surface potential or by terminating stronger atomic bonding even without surface potential perturbation, which are termed Tamm states and Shockley states, respectively [263] [264] [273] [274] [275]. Deep sub-wavelength plasmonic Tamm states and Shockley states can be formed in such a finite metallodielectric lattices with hybrid coupling, depending on the termination of the waveguide array. A periodic array of 20 unit cells is shown in Figure 2.16(a) with different type of

lattice termination, A, B, C, and D at the left end, where the right end side is 'passivated' by the low-index layer. The unit cell parameters are Au (20nm)/MgF2 (50nm, n=1.34)/Si (200nm, n=3.48)/MgF2 (50nm, n=1.34). The diffraction curves for infinite array are shown in Figure 2.15(c). For the given thickness of the layers, the strength of normal coupling (C_+) is stronger than that of anomalous coupling ($|C_-|$), such that the asymmetry constant η is in the range of $-1 < \eta < 0$. The termination type A and C manifest a break of the weak and strong coupling, respectively, with no additional surface perturbation (the dielectric material at the termination point is the same as that in the array), while the termination type B and D represent a break of weak and strong coupling with strong surface perturbation by adding another material at the outermost layer, respectively. While type A does not create any surface modes, type C is shown to support a Shockley-like surface mode due to the strong coupling break, even without surface perturbation. The corresponding mode field for the type C is plotted in Figure 2.16(b). We find the electric field (E_x) highly localized in the first 50 nm low index dielectric layer and rapidly decays into bulk. Also, note that the field confinement occurs mainly in the odd number waveguides. For the type B and D, both types of termination form Tamm-like surface states due to strong surface perturbation, with different mode symmetry from the Shockley-like surface state. The mode field for the type B is a staggered mode changing the field sign at every adjacent waveguide and the type D surface state changes its sign at every other adjacent waveguide[258]. The corresponding eigenvalue for the each type of termination is marked in the band diagram in Figure 2.15(c). The Shockley-like state (C) is located within the bandgap. Tamm-like states (B and D) can be within the bandgap or either above or below the band edge depending on which coupling breaks. For any type of surface states, the electric fields are mainly localized in 50 nm low index dielectric layers, i.e., the 'surface'. The decay rate of the surface states to the bulk is determined by the magnitude of asymmetry constant η. To find existence conditions of surface states , we consider a semi-infinite metallodielectric array and impose boundary conditions. Details on this are found in paper [187].

To summarize, we have considered waveguide arrays with hybrid of alternating normal and anomalous coupling. We have theoretically shown 2-D conical-like diffraction near the diabolic point arising from inverted two-band structures. With the termination of the array, Tamm-like or Shockley-like surface states are formed depending on termination type and strength of surface perturbation. These phenomena are numerically demonstrated in the context of metallodielectric lattices realizing the hybrid coupling. We have also analyzed the existence condition of the surface states. We expect that these new findings, plasmonic diabolic point and deep subwavelength plasmonic surface states, could provide a means to control signal processing and routing in nano-scale optical circuits.

2.5 Conclusions

Until here, we have reviewed the most important aspects of our passive devices fabricated for surface plasmon propagation and manipulation to improve information transfer, achieve

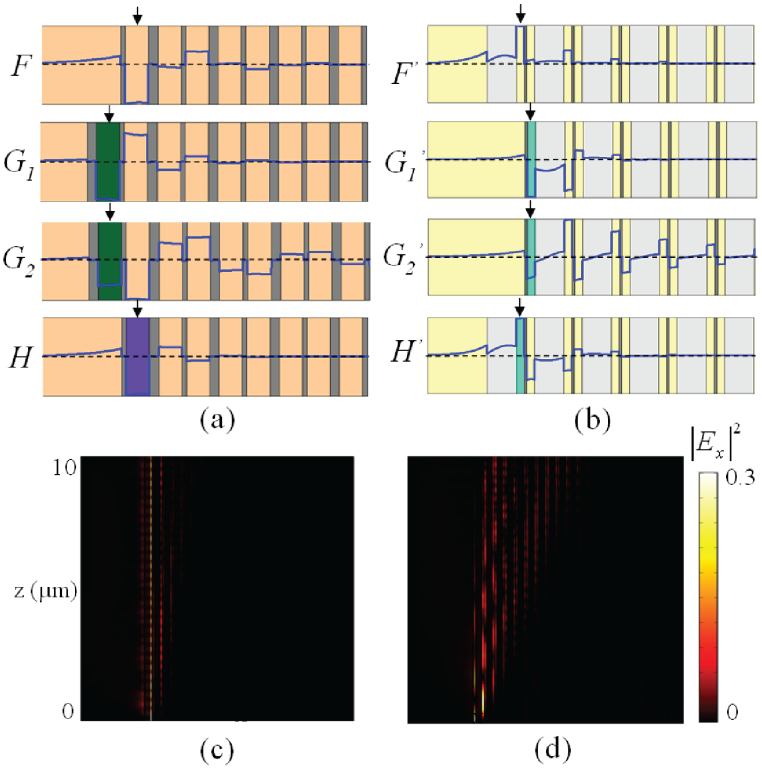

Figure 2.16: *Four configurations for metamaterial surface terminations.* (a) Four types of surface termination at the left end of the array. Right end is passivated. The arrows indicate strength of couplings and their break. HI: high index material (n=3.48), LI: low index material (n=1.34) (b) The mode field profile (Ex) for each surface states. The field is normalized to the maximum (c) The corresponding eigenvalues for the termination type A, B, C, and D in (a).

unconventional light manipulation, or optical surface state generation.

From plasmonic waveguides fabrication in bonded phosphate-doped glass or Quartz, to Focused Ion beam (FIB) drilled multilayers to achieve metamaterials, fabrication and experimentation with plasmonic devices. From these, deposition of the several metallic and dielectric materials was achieved by the most advanced techniques in pro of the best optical conditions of the metal or dielectric. Optical setups with polarization control of incident excitation with time-dependent modulation of signals to achieve the required probe of the designed effects. Optical measurement techniques used, since the observation of stimulated emission in Er doped glass using optical fiber setup and diode lasers until the achievement of the negative index of refraction in the 3D metamaterial at visible and NIR wavelengths using femtosecond light sources.

It remains a challenge to achieve the compensation of losses provided by the metal. Provided gain media there exists a chance to break the limit imposed to unravel a fascinating

broad set of plasmonics devices applicable to several areas that impact our lifes.

Bibliography

[150] Muralidhar Ambati et al. "Observation of stimulated emission of surface plasmon polaritons". In: *Nano letters* 8.11 (2008), pp. 3998–4001.

[151] Barnes W. L., Dereux A., and Ebbesen T. W. In: *Nature* 424 (2003), p. 824.

[152] Ozbay E. In: *Science* 311 (2006), p. 189.

[153] Shalaev V. M. In: *Nat. Photon.* 1 (2007), p. 41.

[154] Kneipp K. et al. In: *Phys. Rev. Lett.* 78 (1997), p. 1667.

[155] Nie S. M. and Emery S. R. In: *Science* 275 (1997), p. 1102.

[156] Lal S., Link S., and Halas N. J. In: *Nat. Photonics* 1 (2007), p. 641.

[157] Anker J. N. et al. In: *Nat. Mater.* 7 (2008), p. 442.

[158] Bellessa J. et al. In: *Phys. Rev. Lett.* 93 (2004), p. 036404.

[159] Chang D. E. et al. In: *Phys. Rev. Lett.* 97 (2006), p. 053302.

[160] Ju J. J. et al. In: *Appl. Phys. Lett.* 91 (2007), p. 171117.

[161] Neogi A. et al. In: *Phys. Rev. B* 66 (2002), p. 153305.

[162] Pockrand I., Brillante A., and Mobius D. J. In: *Chem. Phys.* 77 (1982), p. 6289.

[163] Boltasseva A. and Bozhevolnyi S. I. In: *IEEE J. Sel. Top. Quantum Electron.* 12 (2006), p. 1233.

[164] Protsenko I. E. et al. In: *Phys. Rev. A* 71 (2005), p. 063812.

[165] Vuckovic J., Loncar M., and Scherer A. In: *IEEE J. Quantum Electron.* 36 (2000), p. 1131.

[166] Maziar P Nezhad, Kevin Tetz, and Yeshaiahu Fainman. "Gain assisted propagation of surface plasmon polaritons on planar metallic waveguides". In: *Opt. Express* 12.17 (2004), pp. 4072–4079.

[167] Muhammad Z Alam et al. "Gain assisted surface plasmon polariton in quantum wells structures". In: *Opt. Express* 15.1 (2007), pp. 176–182.

[168] Dentcho A Genov, Muralidhar Ambati, and Xiang Zhang. "Surface plasmon amplification in planar metal films". In: *Quantum Electronics, IEEE Journal of* 43.11 (2007), pp. 1104–1108.

[169] Bergman D. J. and Stockman M. I. In: *Phys. Rev. Lett.* 90 (2003), p. 027402.

[170] Ivan Avrutsky. "Surface plasmons at nanoscale relief gratings between a metal and a dielectric medium with optical gain". In: *Physical Review B* 70.15 (2004), p. 155416.

[171] Maier S. A. In: *Opt. Commun.* 258 (2006), p. 295.

[172] Noginov M. A. et al. In: *Opt. Lett.* 31 (2006), p. 3022.

[173] Seidel J., Grafstrom S., and Eng L. In: *Phys. Rev. Lett.* 94 (2005), p. 177401.

[174] Hill M. T. et al. In: *Nat. Photon.* 1 (2007), p. 589.

[175] Berini P. In: *Phys. Rev. B* 61 (2000), p. 10484.

[176] Charbonneau R. et al. In: *Opt. Lett.* 25 (2000), p. 844.

[177] Berini P. et al. In: *Appl. Phys. Lett.* 90 (2007), p. 061108.

[178] Yan Y. C. et al. In: *Appl. Phys. Lett.* 71 (1997), p. 2922.

[179] Bolshtyansky M., Wysocki P., and Conti N. J. In: *Lightwave Technol.* 18 (2000), p. 1533.

[180] McKay J. A. and Rayne J. A. In: *Phys. Rev. B* 13 (1976), p. 673.

[181] David J Bergman and Mark I Stockman. "Surface plasmon amplification by stimulated emission of radiation: quantum generation of coherent surface plasmons in nanosystems". In: *Physical review letters* 90.2 (2003), p. 27402.

[182] DS Citrin. "Plasmon-polariton transport in metal-nanoparticle chains embedded in a gain medium". In: *Optics letters* 31.1 (2006), p. 98.

[183] NM Lawandy. "Localized surface plasmon singularities in amplifying media". In: *Applied physics letters* 85.21 (2004), p. 5040.

[184] Alessandro Tredicucci et al. "Single-mode surface-plasmon laser". In: *Applied physics letters* 76.16 (2000), p. 2164.

[185] MA Noginov et al. "Enhancement of surface plasmons in an Ag aggregate by optical gain in a dielectric medium". In: *Optics letters* 31.20 (2006), p. 3022.

[186] J Seidel, S Grafström, and L Eng. "Stimulated emission of surface plasmons at the interface between a silver film and an optically pumped dye solution". In: *Physical review letters* 94.17 (2005), p. 177401.

[187] Bumki Min et al. "High-Q surface-plasmon-polariton whispering-gallery microcavity". In: *Nature* 457.7228 (2009), pp. 455–458.

[188] Raether H. R. *Surface Plasmons on Smooth and Rough Surfaces and on Gratings.* Macmillan Publishers Limited. All rights reserved, 1988.

[189] Ebbesen T. W. Barnes W. L. Dereux A. "Surface plasmon subwavelength optics". In: *Nature* 424 (2003), p. 824.

[190] Maier S. A. "Local detection of electromagnetic energy transport below the diffraction limit in metal nanoparticle plasmon waveguides". In: *Nature Mater.* 2 (2003), p. 229.

[191] Stockman M. I. "Nanofocusing of optical energy in tapered plasmonic waveguides". In: *Phys. Rev. Lett.* 93 (2004), p. 137404.

[192] Ozbay E. "Plasmonics: Merging photonics and electronics at nanoscale dimensions". In: *Science* 311 (2006), p. 189.

[193] Cubukcu E. et al. "Plasmonic laser antenna". In: *Appl. Phys. Lett.* 89 (2006), p. 093120.

[194] Lopez-Tejeira F. "Efficient unidirectional nanoslit couplers for surface plasmons". In: *Nature Phys.* 3 (2007), p. 324.

[195] Lal S., Link S., and Halas N. J. "Nano-optics from sensing to waveguiding". In: *Nature Photon.* 1 (2007), p. 641.

[196] Brongersma M. L. and Kik P. G. *Surface Plasmon Nanophotonics*. 2007.

[197] Vahala K. J. "Optical microcavities". In: *Nature* 424 (2003), p. 839.

[198] Noda S., Fujita M., and Asano T. "Spontaneous-emission control by photonic crystals and nanocavities". In: *Nature Photon.* 1 (2007), p. 449.

[199] Ditlbacher H. "Silver nanowires as surface plasmon resonators". In: *Phys. Rev. Lett.* 95 (2005), p. 257403.

[200] Bozhevolnyi S. I. et al. "Channel plasmon subwavelength waveguide components including interferometers and ring resonators". In: *Nature* 440 (2006), p. 508.

[201] Miyazaki H. T. and Kurokawa Y. "Squeezing visible light waves into a 3-nm-thick and 55-nm-long plasmon cavity". In: *Phys. Rev. Lett.* 96 (2006), p. 097401.

[202] Weeber J.-C. et al. "Submicrometer in-plane integrated surface plasmon cavities". In: *Nano Lett.* 7 (2007), p. 1352.

[203] Vesseur E. J. R. "Surface plasmon polariton modes in a single-crystal Au nanoresonator fabricated using focused-ion-beam milling". In: *Appl. Phys. Lett.* 92 (2008), p. 083110.

[204] Cai M., Painter O., and Vahala K. J. "Observation of critical coupling in a fiber taper to a silica-microsphere whispering-gallery mode system". In: *Phys. Rev. Lett.* 85 (2000), p. 74.

[205] Spillane S. M. et al. "Ideality in a fiber-taper-coupled microresonator system for application to cavity quantum electrodynamics". In: *Phys. Rev. Lett.* 91 (2003), p. 043902.

[206] Kippenberg T. J. et al. "Demonstration of an erbium-doped microdisk laser on a silicon chip". In: *Phys. Rev. A* 74 (2006), 051802(R).

[207] Borselli M., Johnson T. J., and Painter O. "Beyond the Rayleigh scattering limit in high-Q silicon microdisks: theory and experiment". In: *Opt. Express* 13 (2005), p. 1515.

[208] Armani D. K. et al. "Ultra-high-Q toroid microcavity on a chip". In: *Nature* 421 (2003), p. 925.

[209] Spillane S. "Ultra-high-Q toroidal microcavities for cavity quantum electrodynamics". In: *Phys. Rev. A* 71 (2005), p. 013817.

[210] Oxborrow M. "Traceable 2-D finite-element simulation of the whispering-gallery modes of axisymmetric electromagnetic resonators". In: *IEEE Trans. Microw. Theory Tech.* 55 (2007), p. 1209.

[211] Johnson P. B. and Christy R. W. "Optical constants of noble metals". In: *Phys. Rev. B* 6 (1972), p. 4370.

[212] Palik E. D. "Handbook of Optical Constants of Solids". In: (1985).

[213] Rowland D. R. and Love J. D. "Evanescent wave coupling of whispering gallery modes of a dielectric cylinder". In: *IEE Proc. J. Optoelectron.* 140 (1993), p. 177.

[214] Hill M. T. "Lasing in metallic-coated nanocavities". In: *Nature Photon.* 1 (2007), p. 589.

[215] Almeida V. R. et al. "All-optical control of light on a silicon chip". In: *Nature* 431 (2004), p. 1081.

[216] Gong Y. Y. and Vuckovic J. "Design of plasmon cavities for solid-state cavity quantum electrodynamics applications". In: *Appl. Phys. Lett.* 90 (2007), p. 033113.

[217] Akimov A. V. "Generation of single optical plasmons in metallic nanowires coupled to quantum dots". In: *Nature* 450 (2007), p. 402.

[218] Jason Valentine et al. "Three-dimensional optical metamaterial with a negative refractive index". In: *Nature* 455.7211 (2008), pp. 376–379.

[219] V. G. Veselago. "The electrodynamics of substances with simultaneously negative values of [epsi] and[thinsp][mgr]". In: *Sov. Phys. Usp.* 10 (1968), p. 509.

[220] D. R. Smith, J. B. Pendry, and M. C. K. Wiltshire. "Metamaterials and negative refractive index". In: *Science* 305 (2004), p. 788.

[221] J. B. Pendry. "Negative refraction makes a perfect lens". In: *Phys. Rev. Lett.* 85 (2000), p. 3966.

[222] K. L. Tsakmakidis, A. D. Boardman, and O. Hess. "/'Trapped rainbow/' storage of light in metamaterials". In: *Nature* 450 (2007), p. 397.

[223] R. A. Shelby, D. R. Smith, and S. Schultz. "Experimental verification of a negative index of refraction". In: *Science* 292 (2001), p. 77.

[224] C. G. Parazzoli et al. "Experimental verification of negative index of refraction using Snell/'s law". In: *Phys. Rev. Lett.* 90 (2003), p. 107401.

[225] N. C. Panoiu and R. M. Osgood. "Numerical investigations of negative refractive index metamaterials at infrared and optical frequencies". In: *Opt. Commun.* 223 (2003), p. 331.

[226] V. M. Shalaev. "Optical negative-index metamaterials". In: *Nature Photonics* 1 (2007), p. 41.

[227] H. J. Lezec, N. A. Dionne, and H. A. Atwater. "Negative refraction at visible frequencies". In: *Science* 316 (2007), p. 430.

[228] N. Liu. "Three-dimensional photonic metamaterials at optical frequencies". In: *Nature Mater.* 7 (2008), p. 31.

[229] A. J. Hoffman. "Negative refraction in semiconductor metamaterials". In: *Nature Mater.* 6 (2007), p. 946.

[230] M. Silveirinha and N. Engheta. "Tunneling of electromagnetic energy through subwavelength channels and bends using epsilon-near-zero materials". In: *Phys. Rev. Lett.* 97 (2006), p. 157403.

[231] B. Edwards. "Experimental verification of epsilon-near-zero metamaterial coupling and energy squeezing using a microwave waveguide". In: *Phys. Rev. Lett.* 100 (2008), p. 033903.

[232] S. Enoch. "A metamaterial for directive emission". In: *Phys. Rev. Lett.* 89 (2002), p. 213902.

[233] T. J. Yen. "Terahertz magnetic response from artificial materials". In: *Science* 303 (2004), p. 1494.

[234] W. J. Padilla. "Dynamical electric and magnetic metamaterial response at terahertz frequencies". In: *Phys. Rev. Lett.* 96 (2006), p. 107401.

[235] H. T. Chen. "Active terahertz metamaterial devices". In: *Nature* 444 (2006), p. 597.

[236] S. Linden. "Magnetic response of metamaterials at 100[thinsp]terahertz". In: *Science* 306 (2004), p. 1351.

[237] C. M. Soukoulis, S. Linden, and M. Wegener. "Negative refractive index at optical frequencies". In: *Science* 315 (2007), p. 47.

[238] G. Dolling, M. Wegener, and S. Linden. "Realization of a three-functional-layer negative-index photonic metamaterial". In: *Opt. Lett.* 32 (2007), p. 551.

[239] A. Alu and N. Engheta. "Three-dimensional nanotransmission lines at optical frequencies: A recipe for broad band negative-refraction optical metamaterials". In: *Phys. Rev. B* 75 (2007), p. 024304.

[240] S. Zhang. "Optical negative-index bulk metamaterials consisting of 2D perforated metal-dielectric stacks". In: *Opt. Express* 14 (2006), p. 6778.

[241] T. Li. "Coupling effect of magnetic polariton in perforated metal/dielectric layered metamaterials and its influence on negative refraction transmission". In: *Opt. Express* 14 (2006), p. 11155.

[242] G. V. Eleftheriades. "Analysis of bandwidth and loss in negative-refractive-index transmission-line (NRI-TL) media using coupled resonators". In: *IEEE Microw. Wireless Components Lett.* 17 (2007), p. 412.

[243] A. Grbic and G. V. Eleftheriades. "Overcoming the diffraction limit with a planar left-handed transmission-line lens". In: *Phys. Rev. Lett.* 92 (2004), p. 117403.

[244] A. Lai, C. Carloz, and T. Itoh. "Composite right-/left-handed composite transmission line metamaterials". In: *IEEE Microw. Mag.* 5 (2004), p. 34.

[245] J. B. Pendry et al. "Low frequency plasmons in thin-wire structures". In: *J. Phys. Condens. Matter* 10 (1998), p. 4785.

[246] X. B. Fan. "All-angle broadband negative refraction of metal waveguide arrays in the visible range: Theoretical analysis and numerical demonstration". In: *Phys. Rev. Lett.* 97 (2006), p. 073901.

[247] M. Notomi. "Theory of light propagation in strongly modulated photonic crystals: Refraction-like behavior in the vicinity of the photonic band gap". In: *Phys. Rev. B* 62 (2000), p. 10696.

[248] P. B. Johnson and R. W. Christy. "Optical constants of the noble metals". In: *Phys. Rev. B* 6 (1972), p. 4370.

[249] Sung Hyun Nam et al. "Deep subwavelength surface modes in metal–dielectric metamaterials". In: *Optics letters* 35.11 (2010), pp. 1847–1849.

[250] Sung H Nam et al. *General properties of surface modes in binary metal-dielectric metamaterials*. Tech. rep. DTIC Document, 2010.

[251] M Scalora et al. "Transparent, metallo-dielectric, one-dimensional, photonic band-gap structures". In: *Journal of Applied Physics* 83.5 (1998), pp. 2377–2383.

[252] Xiebin Fan et al. "All-angle broadband negative refraction of metal waveguide arrays in the visible range: theoretical analysis and numerical demonstration". In: *Physical review letters* 97.7 (2006), p. 073901.

[253] Yongmin Liu et al. "Subwavelength discrete solitons in nonlinear metamaterials". In: *Physical review letters* 99.15 (2007), p. 153901.

[254] Lieven Verslegers et al. "Deep-subwavelength focusing and steering of light in an aperiodic metallic waveguide array". In: *OPTO*. International Society for Optics and Photonics. 2010, 76040O–76040O.

[255] Guy Bartal, Geoffroy Lerosey, and Xiang Zhang. "Subwavelength dynamic focusing in plasmonic nanostructures using time reversal". In: *Physical Review B* 79.20 (2009), p. 201103.

[256] Andrea Locatelli et al. "Diffraction engineering in arrays of photonic crystal waveguides". In: *Opt. Lett.* 30.21 (2005), pp. 2894–2896.

[257] Andrey A. Sukhorukov and YuriS. Kivshar. "Discrete gap solitons in modulated waveguide arrays". In: *Opt. Lett.* 27.23 (2002), pp. 2112–2114.

[258] Mario I. Molina et al. "Discrete surface solitons in semi-infinite binary waveguide arrays". In: *Opt. Lett.* 31.15 (2006), pp. 2332–2334.

[259] David R Yarkony. "Diabolical conical intersections". In: *Reviews of Modern Physics* 68.4 (1996), p. 985.

[260] Michael Berry. "Making waves in physics". In: *Nature* 403.6765 (2000), pp. 21–21.

[261] Stefanie Godefroo et al. "Classification and control of the origin of photoluminescence from Si nanocrystals". In: *Nature nanotechnology* 3.3 (2008), pp. 174–178.

[262] Young-Woo Son, Marvin L Cohen, and Steven G Louie. "Energy gaps in graphene nanoribbons". In: *Physical Review Letters* 97.21 (2006), p. 216803.

[263] N Malkova and CZ Ning. "Shockley and Tamm surface states in photonic crystals". In: *Physical Review B* 73.11 (2006), p. 113113.

[264] N Malkova and CZ Ning. "Interplay between Tamm-like and Shockley-like surface states in photonic crystals". In: *Physical Review B* 76.4 (2007), p. 045305.

[265] Kenji Ishizaki and Susumu Noda. "Manipulation of photons at the surface of three-dimensional photonic crystals". In: *Nature* 460.7253 (2009), pp. 367–370.

[266] Pochi Yeh, Amnon Yariv, and AY Cho. "Optical surface waves in periodic layered media". In: *Applied Physics Letters* 32 (1978), p. 104.

[267] Ivan L Garanovich, Andrey A Sukhorukov, and Yuri S Kivshar. "Defect-free surface states in modulated photonic lattices". In: *Physical review letters* 100.20 (2008), p. 203904.

[268] Simin Feng, J. Elson, and Pamela Overfelt. "Optical properties of multilayer metal-dielectric nanofilms with all-evanescent modes". In: *Opt. Express* 13.11 (2005), pp. 4113–4124.

[269] MV Berry and M Wilkinson. "Diabolical points in the spectra of triangles". In: *Proceedings of the Royal Society of London. A. Mathematical and Physical Sciences* 392.1802 (1984), pp. 15–43.

[270] Or Peleg et al. "Conical diffraction and gap solitons in honeycomb photonic lattices". In: *Physical review letters* 98.10 (2007), p. 103901.

[271] Kentaro Nomura and AH MacDonald. "Quantum transport of massless dirac fermions". In: *Physical review letters* 98.7 (2007), p. 076602.

[272] RF Oulton et al. "Confinement and propagation characteristics of subwavelength plasmonic modes". In: *New Journal of Physics* 10.10 (2008), p. 105018.

[273] Sydney G Davison and Maria Stkaeslicka. *Basic theory of surface states*. Vol. 46. Oxford University Press, 1992.

[274] J Koutecky. "An interpretation of the conditions for the existence of Shockley surface states". In: *Cechoslovackij fiziceskij zurnal B* 11.8 (1961), pp. 565–571.

[275] T Goto et al. "Optical Tamm states in one-dimensional magnetophotonic structures". In: *Physical review letters* 101.11 (2008), p. 113902.

[276] Jaroslaw Klos. "Conditions of Tamm and Shockley state existence in chains of resonant cavities in a photonic crystal". In: *Physical Review B* 76.16 (2007), p. 165125.

Chapter 3

Uncertainty control for Plasmonic lithography

3.1 Introduction

Time control of electronic sequential triggering of electro-optic modulators to plasmonic lens array on flying head at few nanometers on a spinning substrate, as an experience of both, ultrafast electronic system digital design and plasmonic nanolithography concept based on studies of tribology, the science of surfaces in continuous friction. Flying heads represent the fastest way to scan a surface, widely used in hard disk drives and other yet older systems.

The fabrication of integrated circuits relies strongly on lithographic processes to achieve a high throughput process.[277][278] Resolution in conventional lithography is constrained by the diffraction limit of light. Several alternatives have proposed mechanisms to provide resolution below the 22nm limit of standard lithography but have failed in providing a reliable scalable process. One other alternative is called Plasmonic nanolithography. It is based on the metamaterial called "Plasmonic lens" a device capable of providing such resolution. This lens can be used as an element of an individually addressable array which can be used in conjunct with flying head technology (tribology) and fast-parallel electronics to provide a system capable of providing a tool for the continuous fabrication of integrated circuits in subwavelength regimes.

In this chapter, a control system based on FPGA technology is presented. FPGA structure allows for faster and truly parallel Finite State Machines (FSM) for Pattern Generation with nanosecond accuracy. The design of these FSMs is detailed and implemented. The solution to Inter-track Stitching errors is provided by using an additional Magnetic Encoder to generate a more accurate Clock signal (CLK). This CLK signal is used to implement an FSM trigger mechanism for the pattern generator. Control signals for other sub-systems (focusing, spindle control, interfaces) are considered to program a time-effective FPGA-based Central Control Unit for the Plasmonic Nanolithography System. Results for single and dual-lens system are shown. Performance against the previous digital signal processor (DSP) used are

underlined.

3.2 Sub-22nm alternatives for Lithography

Conventional Lithography techniques for mass production in the semiconductor industry rely on the resolution that can be achieved by a mask projection method. Due to the wave nature of light, the resolution that can be reached using lenses is diffraction limited, that is, transmission through an aperture is accompanied by diffraction. The uncertainty principle for position and momentum, explains that by laterally confining a wave to a region (Δx), an associated uncertainty in its momentum in the transverse direction (Δp) will exist, that is, an uncertainty in the angle of propagation, hence compromising the resolution that can be accomplished. To improve resolution (to reduce Δx) we can reduce the working wavelength or increase the index of refraction of the lens being used (which affects the angle of propagation). Current fabrication techniques for the fabrication below the 22nm rely on the use of shorter wavelength excitation (now, all the way into the EUV) and using fluids like oils to provide a higher refractive index. . Although the resolution of this technique is improving, there have also been associated increases in costs. The fabrication of high-quality lithography masks is also time consuming and expensive, which restraining device prototyping, where changes in design are constantly needed.[277][278]

Maskless lithography techniques [287], including Electron-Beam Lithography (EBL)[283], Focused Ion-Beam (FIB)[279] and scanning-probe lithography (SPL)[280][282], offer a path to overcome these obstacles by reducing mask costs. However, the low throughput of the techniques is still a very hard obstacle to overcome. In addition to the fact that SPL technology relies on a slow scan of the tips at a distance of 10-100 nm from the surface, owing to the limited feedback bandwidth available to control the tip-sample distance at higher speeds. From these techniques the most promising candidate continues to be Electron Beam Lithography (EBL)[284]. This technique is currently used to fabricate masks and it is a very common tool in the nanofabrication of devices for research purposes. This technique relies heavily on a scanning process, reducing the throughput and increasing its price (the price of a typical lithography tool is close to 20 million of dollars). Multi-axial electron-beam lithography (EBL high-throughput version) [285] [289] is proposed to use multiple electron beams in parallel manner. However, there are difficulties in simultaneously regulating the multiple beam sizes and beam positions because of the thermal drift and electrical charge Coulomb interactions, resulting in lens aberration. Other techniques, such as, Zone-plate-array lithography (ZPAL) , uses a large array of diffractive optical elements or spatial light modulators to improve the throughput, but the ultimate resolution is still restricted to the diffraction limit. [287]. Techniques such as nano-imprint or self assembly have shown high throughput possibilities, but have still to show independence from the previous methods to fabricate the mold or the surface to be patterned, etc. Also, self assembly shows long-rage disorder thus setting an uncontrollable process of fabrication for big-size samples.

3.3 Plasmonic Nano Lithography

A particular way of using light can potentially increase throughput by two to five orders of magnitude compared to that achieved by parallel SPL and commercial electron-beam lithography. A high-throughput form of plasmonic nanolithography to circumvent the critical parallelization and slow scanning challenges.[294][296]

When light strikes a metal surface it can excite collective oscillations of the electrons at the surface that are known as surface plasmons [291], [292] [301] [297]. These oscillations can have wavelengths that are much shorter than the wavelength of the light that excited them, which means that surface plasmons could have applications for imaging and lithography with resolution beyond the diffraction limit [13]. A plasmonic lens made of a concentric ring grating has been used to focus the light to a sub-100 nm spot at the near field with local intensity .100 times higher than the incident light. These earlier results clearly suggest the potential of using a plasmonic lens for nanolithography. However, owing to the exponential decay of the evanescent field, the tightly focused spot only exists at the near field of the plasmonic lens, normally closer than 100 nm. Thus, high-throughput nanopatterning requires a new mechanism to ensure precise control of the nanoscale gap between the plasmonic lens and substrate during high-speed writing. A wide range of antennas is used to concentrate the energy more effectively, few of the most important designs have been collected, compared and pictured by reference [302]

To achieve high-speed scanning while maintaining the nanoscale gap, a novel air-bearing slider [298] is designed to fly the plasmonic lens arrays at a height of 20 nm above the substrate at speeds of between 4 and 12 m/s. The rotation of the substrate creates an air flow along the bottom surface of the plasmonic flying head, known as the air bearing surface (ABS) [299]. The ABS generates an aerodynamic lift force and it is balanced with the force supplied by the suspension arm to precisely regulate a nanoscale gap between the plasmonic lens and the disk.

In addition to the high-speed scanning we fabricate and individually control multiple flying Plasmonic lenses using a single air bearing. Figure 3.1 shows the Plasmonic lens array and the Plasmonic flying head concept. The throughput of our system can be further improved with the convenient null interaction between multiple pulses of light addressing the plasmonic lens array. This low cost nanofabrication scheme has the potential to fabricate few thousand lenses in each slider. It is the intention of this work to provide evidence of a system capable of firing several electro-optic modulators in a parallel and synchronous fashion [303].

The overall system is pictured in figure 3.2 The system uses a Digital Signal Processor (DSP) to generate a 200MHz signal triggering an Electro-Optic Modulator (EOM). This EOM modulates a picosecond-pulsed laser beam (365nm wavelength) with the proper time delays to produce space-delayed patterns (in accordance to the DSP generated signal and to the velocity of the spindle 10m/s) of sub-20nm spots recorded in the disk.

Previous to the disk surface, the beam pulse travels through an optical system in charge of conditioning the pulse and focusing it into the plasmonic lens. The major functions of

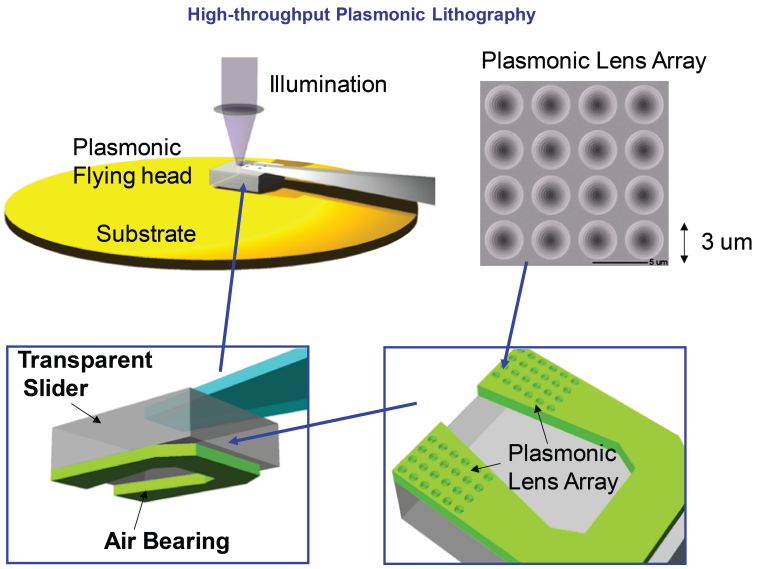

Figure 3.1: *Proposed scheme for High-throughput Plasmonic nanolithography.* An array of plasmonic lenses is fabricated on the Plasmonic Flying Head. A transparent slider supports thousands of plasmonic lenses separated by 3 um, which can be independently addressed. An electronic system capable of modulating the light signals arriving at each lens to accurately distibute, as needed, spot patterns in the disk.

these optics are for alignment purposes and the expansion of the beam. The expansion of the beam is required since we are using a high power laser beam. Expansion of the beam reduces the power density travelling through our optical mirrors (needs to be smaller than the damage threshold). Also, since we need to focus the light into a tight spot, we use a lens with large Numerical Aperture (NA) of 0.6. High NA lens needs a large effective enter aperture, if beam is thinner than the lens, you are not using the full NA of the lens. Thus confinement is compromised.

The disturbances to the motion in normal-to-the-lens direction are compensated by a simple PID control (Pre-focusing control system) since it is a low bandwidth perturbation to the system. An actuator (Lens Actuator) with a bandwidth of 100 kHz can be driven for such a purpose. Prefocusing measures the distance variations between the lens and the head, the source of error comes from the disk-head perturbations while flying. An interferometer-based measurement uses a lens to focus on the head (the head has metal on it). A CW-laser beam is reflected back after being loosely focused on the lens. The distance is acquired by an ADC in a separate PID-control board. The distance error is corrected with the lens actuator (focusing or moving the focal length). This system is in working condition and it is independent to some extent, since it is not in the same time-scale, of the pattern generation CLK related routines.

For the pattern generation, the DSP uses the optical encoder signal generated by the

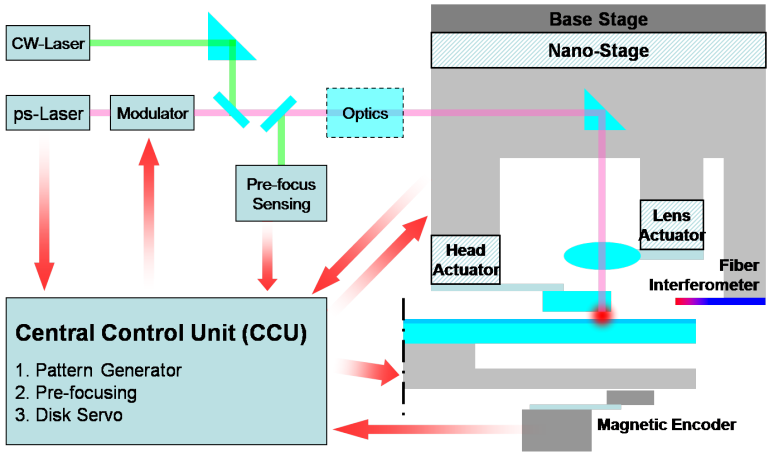

Figure 3.2: *Central Control Unit.* FPGA-based time-management unit to syncronize the dynamics of the system to the modulation of laser light pulses and optical encoder counts so that the location of the pattern is accurate. System Setup. The optical encoder of the spindle generates a trigger signal for a DSP to modulate by means of an EOM the pulses of a picosecond Laser source. The pre-focusing system regulates the height of the lens used to focus the pulses onto the Plasmonic flying head. The actuators for x-y position location (Nano-Stage and Head Actuator) are used to compensate disturbances in the radial direction.

spindle to trigger events in the EOMs. This optical encoder has 1024 counts per revolution. When the spindle spins at 10m/s generates a 33 kHz signal that constraint us to have spatial uncertainty (?x) of 300nm at most. In addition to this, DSP electronics introduce additional uncertainty in time delay of 50ns (200MHz) due to the hierarchical configuration in its logic and poor or inexistent CLK management possibilities.

The delay introduced by each system in the picture, especially for the purposes of patterning, is of special attention in this work. The time delays introduced by the DSP will be reduced by the usage of an FPGA. A device capable of implementing with optimal usage of hardware a truly parallel logic system that allows for CLK management. Also, additional to this, we notice that a much better measurement of position would be of benefit in the spatial location accuracy of our system.

Inter-track Stitching Error

In Figure 3.3 an AFM picture with the pattern "SINAM" shows the consequences of the uncertainty in delay on the spot location track after track. In the pattern the letters "I" is in the radial direction (perpendicular to the track) and clearly shows that the error can be as high as 1um. This error in space location is known as "inter-track" stitching error and it is a very well known problem in Hard disk Drive (HDD) control systems.

The present problem relates generally to a method for writing servo patterns on a data

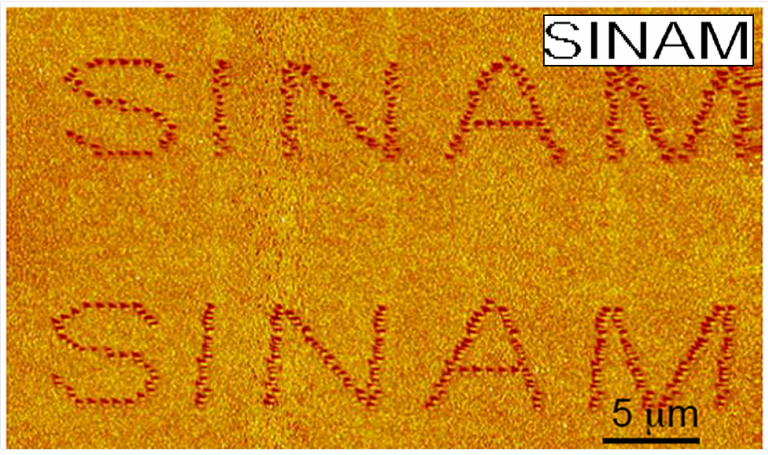

Figure 3.3: *Inter-track stitching error in pattern location.* The pattern here stands for the center SINAM. Along the letter "I" which should be a perfect line. After AFM measurements we find inaccuracies on the order of 300nm. The space location uncertainty is suspected introduced by DSP digital electronics time delays and low resolution of an optical encoder providing position location. Error is reduced by an order of magnitude by interpolation methods.

disk storage device, and more particularly, to self servo writing of servo sector patterns on a data disk storage device using geometric referencing to correct read write offset errors. In many processing and computing systems, magnetic data storage devices, such as disk drives are utilized for storing data. A typical disk drive includes a spindle motor having a rotor for rotating one or more data disks having data storage surfaces, and an actuator for moving a head carrier arm that supports a transducer (read/write) heads (HGAs), radially across the data disks to write data to or read data from concentric data tracks on the data disk.

In our system, the Plasmonic head position information is crucial to scan the surface of the disk and accurately locate sub 22nm-sized "spots" in a controlled and synchronous fashion. Due to the fact that the disks to be patterned are generally nonmagnetic, we don't intend to add a magnetic transducer head to the same slider. Rather, we include an additional disk, a magnetic disk. If the spindle velocity is kept constant we can assume that the velocity fluctuations of the spindle can be for both systems of the same origin and order, thus an important opportunity to study the time evolution of such fluctuations. In general, a magnetic transducer head is positioned very close to a data storage disk surface by a slider suspended upon an air bearing. The HGA of use is a SUPERHAWK by Seagate Corp. The close proximity of the head to the disk surface allows recording of very high resolution data and servo patterns on the disk surface. Servo patterns are typically written with uniform angular spacing of servo sectors and interleaved data sectors or blocks. An example servo pattern includes circumferentially sequential, radially staggered single frequency bursts. Servo patterns provide the disk drive with head position information to enable a linear actuator, instead of a rotary voice coil motor, to move the head from starting tracks to

destination tracks during random access track seeking operations. Further, the servo patterns provide the disk drive with head position information to enable the actuator to position and maintain the head in proper alignment with a track centerline during track following operations when user data is written to or read from the available data block storage areas in the patterned tracks on the surface of the magnetic disk.

Furthermore, the data written is of use in the synchronization of the system to further reduce electronic time delay uncertainty by introducing a new clock (CLK) signal. Data transducer heads currently in use employ dual elements. An inductive write element having a relatively wide recording gap is used to write information into the data tracks, and a read element such as a magneto-resistive sensor having a relatively narrow playback gap is used to read information from the data tracks. With this arrangement data track densities equaling and exceeding for example 30,000 tracks per inch are possible, thus enabling a more accurate measurement of distance. Conventional servo patterns are written into the servo sectors of each disk using a servo writer at a point in the drive assembly process before the hard disk unit is sealed against particulate contamination from the ambient. Such conventional servo writing method has been largely replaced by a self servo writing method. In the self servo writing methods, it is necessary to write the servo data precisely at a prescribed position on the disk. The head incorporated in the disk drive still utilizes the two discrete elements, i.e., the read-head element and the write-head element. A position offset inevitably exists between these elements. The position offset corresponds to the distance between the centerlines of the read and write head elements. This position offset is corrected and fixed. Since motion along the track is also fixed, then we expect to be able to follow a CLK track and thus trigger the pattern generator. A digital system has to independently control the task of "following" the track. This is also implemented in the FPGA and it is made to be optimal in time delay by the proper location of CLK buffers and Digital Lock Loop components to de-skew the signal. More specifically, the position accuracy of our system will be improved by a factor of 2 by implementing a magnetic encoder that is able to provide a stable high resolution in space CLK signal (200MHz).

The implementation of a magnetic encoder and the introduction of an FPGA-based control system regulating diverse tasks such as magnetic self-servo writing, track following, CLK de-skewing, pattern generation, real time space location measurement (fiber interferometer), space compensation (head actuator), a computer interface. This group of subsystems conform the Central Control Unit of the system by including the other time-scale systems such as prefocusing, graphic user interface, etc. that make of the overall system a very reliable and fast patterning system easier to control and use

Both improvements are independent of each other and can be achieved and explained in any order. For convenience, the FPGA introduction is explained first. After experimental results for this section, the magnetic encoder implementation and corrections to the FPGA programs will be explained in the next section.

3.4 FSM for FPGA-based Pattern Generation

To handle all the functions our Central Control Unit has, we are relying on FPGA technology. An FPGA essentially consists of an array of logic blocks (called Configurable Logic Block, CLB, or Logic Array Block, LAB, depending on vendor), I/O pads, and routing channels. In general, a logic block (CLB or LAB) consists of a few logical cells (called ALM, LE, Slice etc). A typical cell consists of a 4-input Lookup table (LUT), a Full adder (FA) and a D-type flip-flop. An application circuit is mapped into an FPGA with adequate and optimal resources. While the number of CLBs/LABs and I/Os required is easily determined from the design, the number of routing tracks needed may vary considerably even among designs with the same amount of logic. Since unused routing tracks increase the cost (and decrease the performance) of the part without providing any benefit, FPGA design makes emphasis on using just enough tracks so that most designs that will fit in terms of LUTs and IOs can be routed. These features allow us to build the highest levels of performance and functionality into their FPGA-based systems. We use FPGAs from Xilinx Corp. Virtex-5 LXT and SXT FPGAs. These are built on a 40 nm state-of-the art copper process technology, Virtex-6 FPGAs are a programmable alternative to custom ASIC technology.

For the implementation of the pattern generator we used VHDL language to implement an alternative mode for the look-up tables where they are used as 16-bit shift registers (SRL16). Using this Shift Register LUT (SRL) mode can improve performance and rapidly lead to cost savings of an order of magnitude. Although the SRL16 can be automatically inferred by the software tools, considering their effective use can lead to more cost-effective designs. Shift-in operations are synchronous with the clock, and output length is dynamically selectable. A separate dedicated output allows the cascading of any number of 16-bit shift registers to create whatever size shift register is needed. Each CLB resource can be configured using four of the eight LUTs as a 64-bit shift register. These shift registers enable the development of efficient designs for applications that require delay or latency compensation. Shift registers are also useful in synchronous FIFO and Content-Addressable Memory (CAM) designs The structure of the SRL16 is described from the bottom up, starting with the shift register and then building up to the surrounding FPGA structure. The Look-Up Table can be described as a 16:1 multiplexer with the four inputs serving as binary select lines, and the values programmed into the Look-Up Table serving as the data being selected (see Figure 3.4).

The address can be thought of as dynamically changing the length of the shift register. If D is used as the shift register output instead of Q15, setting the address to 7 (0111) selects Q7 as the output, emulating an 8-bit shift register. Note that since the address lines control the MUX, they provide an asynchronous path to the output. Each SRL16 LUT has an associated flip-flop that makes up the overall logic cell. The addressable bit of the shift register can be stored in the flip-flop for a synchronous output or can be fed directly to a combinatorial output of the CLB. When using the register, it is best to have fixed address lines selecting a static shift register length to avoid timing hazards. Since the clock-to-output delay of the flip-flop is faster than the shift register, performance can be improved by addressing the second-to-last bit and then using the flip-flop as the last stage of the shift register. Using

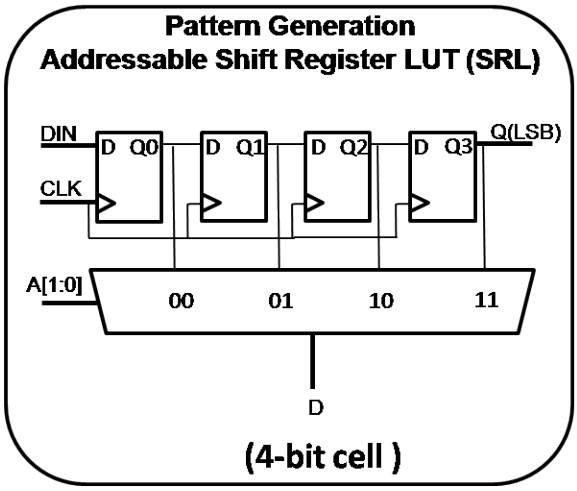

Figure 3.4: *Single Pattern Generator .* Shift-Register Look Up Tables (SR-LUTs are used to define regions of memory which can be rotated to emulate a serial output of the size of the register. It has been envisioned to be able to record a whole patter or pattern while downloading (in real-time) banks of memory with other patterns. LUT Modeled as a Multiplexer. With the SRL16 configuration, the fixed LUT values are configured instead as an addressable shift register. The shift register inputs are the same as those for the synchronous RAM configuration of the LUT: a data input, clock, and clock enable (not shown). A special output for the shift register is provided from the last flip-flop, called Q15 on the library primitives or MC15 in the FPGA Editor. The LUT inputs asynchronously (or dynamically) select one of the16 storage elements in the shift register.

the flip-flop also allows for asynchronous or synchronous set or reset of the output. The shift register input can come from a dedicated SHIFTIN signal, and the Q15/MC15 signal from the last stage of the shift register can drive a SHIFTOUT output. The addressable D output is available in all SRL primitives, while the Q15/MC15 signal that can drive SHIFTOUT is only available in the cascadable SRLC16 primitive, shown in Figure 3.4.

The design of the pattern generator relies heavily on this primitive. Figure 3.5 shows a Finite State Machine designed with the only purpose of synchronizing the optical encoder events with the a series of shift events of a 1024 bit long word that has the first track of an image. Two counters are coded. One is to aid in the counts of the 1024 shifts and the other counter is to count the number of tracks. Once the pattern is done shifting 1024 times it questions for the change of pattern (track) data that is to occur once 1024 trigger events happen (1024 marks per revolution from the optical encoder). The machine returns to the IDLE state after two PRE-IDLE STATES that were added to wait for the TRIGGER signal to be 0, otherwise it would return to OUTPUTTING state if found in IDLE. Two PRE-IDLE states because of glitch existent in the falling edge of the trigger event in the experiment. An additional state is sufficient to have a very robust triggering of events.

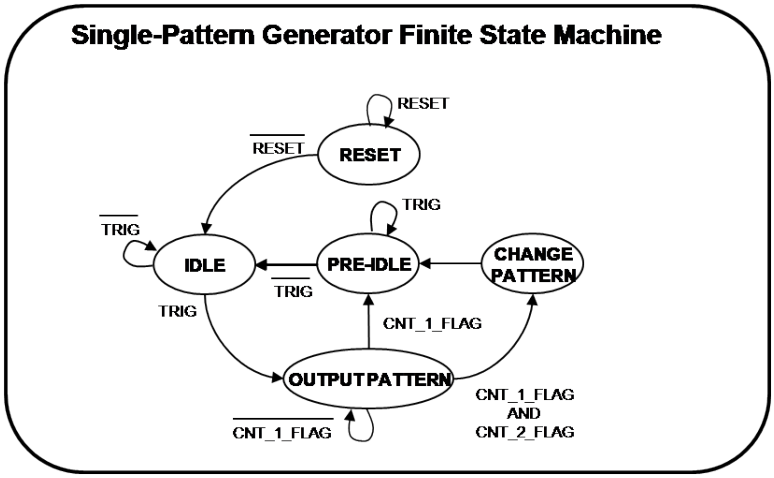

Figure 3.5: *Single Pattern Generator Finite State Machine State Diagram.* The evolution of the states is enable by the optical encoder trigger (1024 bits per revolution). The laser source has a repetition rate of 80MHz, which is internalized by the FPGA and multiplied by 4 to achieve faster rates synchronized to the laser clock. After that, each optical encoder pulse allows for a sequentially better behavior than of a DSP (no access to CLK). The system remains in state RESET, until a trigger event (optical encoder) promotes the outputting (shifting 1024 times) of a word. The system returns to idle after two pre-idle states (added for robustness on trigger falling edge)

Once the FSM is coded, the interfacing of the FPGA with the overall Plasmonic system is designed like is shown in Figure 3.8. The signal used as CLK comes from the picosecond laser system. A signal of 80MHz. The laser CLK is de-skewed by using a DLL. The global clock distribution network minimizes clock skews due to loading differences. By monitoring a sample of the DLL output clock, the DLL can compensate for the delay on the routing network, effectively eliminating the delay from the external input port to the individual clock loads within the device.

In addition to providing zero delay with respect to a user source clock, the DLL can provide multiple phases of the source clock. The DLL can also act as a clock doubler or can divide the user source clock by up to 16. Clock multiplication gives the designer a number of design alternatives. For our purposes, a 80 MHz source clock doubled by the DLL can drive an FPGA design operating at 160 MHz. This technique can simplify board design because the clock path on the board no longer distributes such a high-speed signal. A multiplied clock also provides designers the option of time-domain multiplexing, using one circuit twice per clock cycle, consuming less area than two copies of the same circuit. Two DLLs can be connected in series to increase the effective clock multiplication factor to four (320MHz). The DLL can also act as a clock mirror. By driving the DLL output off-chip and then back in again, the DLL can be used to deskew a board-level clock between multiple devices. De-skewing the CLK is important since almost all processes running in the pattern generators

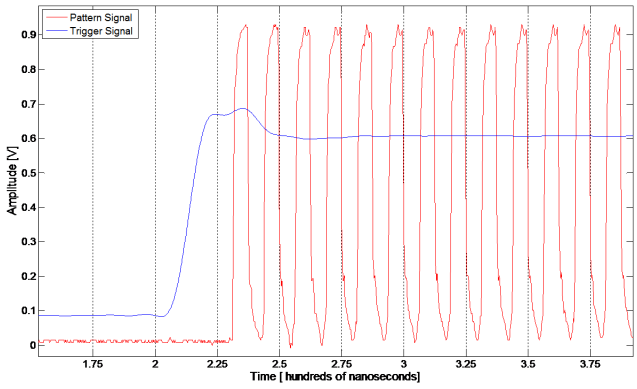

Figure 3.6: *Time evolution of Patterning signal (red) and Optical Triggering (blue).* The time delay after the optical trigger event is almost a constant 1.2ns. The inset shows the periodic leading edge of the trigger and associated LSB possible patterning events (here periodic 0, 1) for a single-lens.

are dependent on this signal. Figure 3.6 shows the time quasi constant delay introduced by the logic gates. Both signals, the triggering signal and the patterning signal are observed.

Figure 3.7 pictures Register Transfer Level (RTL) interconnection for two pattern generators. The implementation was run in ISE 10.1 and found 1% and 2% of total LUT usage for single and dual -pattern generators. With this we can expect approximately 100 patterns generators can be digitally modulated at a speed of 380MHz in a parallel and independent fashion by a single FPGA chip, which is not larger than 5x5cm in size. If this system was to be implemented to modulate the EOMs for 1000 plasmonic lenses, in principle it would be achieved by using 10 FPGAs.

3.5 Experimental Results for Single and Dual Plasmonic lens

For the experiment, the lens design was changed a bit to improve the spot confinement. H-shaped Plasmonic lenses were used. Figure 3.8, shows the cross-section of such a lens. It is important to note that due to the symmetry of the lens, confinement could be achieved in each of the two corners of the lens by tilting the angle of incidence.

The sapphire air bearing surface (ABS) was fabricated using micro fabrication techniques. First, the ABS pad and base recesses were fabricated using a lithography setup (Karl Suss MA6 Mask Aligner) to pattern the resist for subsequent Aluminium Reactive Ion Etcher (RIE) to etch the sapphire substrate. The substrate was separated into individual sliders using a Dicing Saw. An 80-nm chromium film (mechanical properties) and a 5-nm diamond-like coating protective layer were sputtered using a sputtering machine (Edwards Auto 306

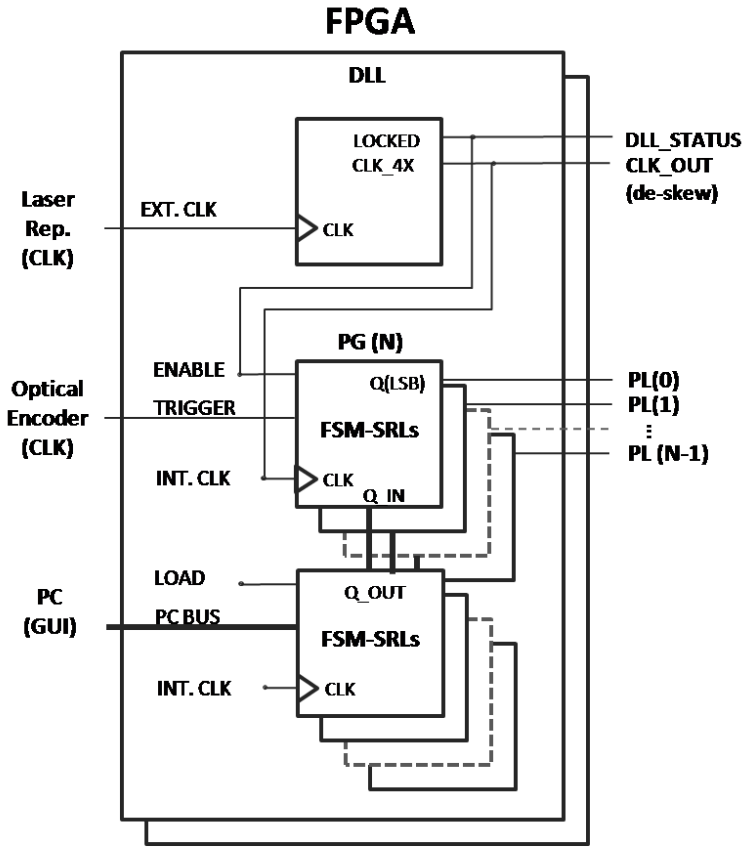

Figure 3.7: *FPGA Interfacing for the use of 2 or more Pattern generators.* A DLL unit is also used to better follow the variations in phase of the CLK. A DLL is like a PLL but digital. The DLL is used to better track the Laser Clock and multiply it by 4. : Synchronizing two pattern generators to a Laser CLK signal (times 4). A DLL is added to the input to de-skew the CLK signal. The spindle optical encoder triggers events in the pattern generator. The DLL primitive provides a LOCKED signal, which is used to alert the state machine when the external CLK source is irregular or nonexistent

DC and RF Sputter Coater). Then, a plasmonic lens was milled on the Chromium film using focused ion beam milling (FIB, FEI Strata201 XP). Finally, the slider was glued to a suspension using UV-curable glue, and evaluated in a dynamic flying height tester (DFHT IV, Phase Metrics).

For the head-disk protective overcoat, we used 80nm of inorganic TeOx [300] based solid resist deposited using magnetron sputtering and inspected by SEM and AFM to ensure good film quality. Additionally, to prevent contact induced resist damage, a protective coating of Si_3N_4 film is deposited by magnetron sputtering. According to AFM measurement, the RMS roughness value after deposition of the protective layer is about 0.3 nm which is almost the same as that of the substrate. Furthermore, a 2-nm thick lubricant Perfluoropolyether-Z

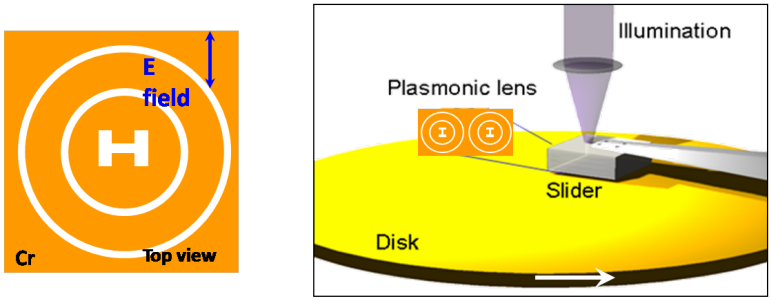

Figure 3.8: *Experimental Setup.* For this test, we use of an H-apperture for plasmonic lens. Multiple lenses are fabricated for parallel writing tests. Experimental configuration of the plasmonic flying head.

(PFPE-Z) is also coated on the top of the overcoat layer and examined using Optical Surface Analyzer (Candela OSA 5100) for thickness and uniformity. This tribological configuration greatly reduces the friction and possible damages when slider and the disk are in contact. Prior to experiments, individual plasmonic head was tested using dynamic flying head tester (Phase Metrics DFHT-IV), Acoustic Emission (AE) system and Laser Doppler Velocimeter (Polytec LDV OFV-512).

In the following lithography tests, exposures were obtained with no significant AE contact signal. With these tribological properties, we were able to directly load our flying heads on to the disk at 10 m/s linear disk velocity with no damage to the resist. The optical setup for the experiment addresses a single Plasmonic lens to perform a first test. The pattern "PIL" was encoded in a 32X1024 bits map in the LUTs previously described. Figures 3.9 shows AFM pictures of the pattern "PIL" recorded as heat-activated resist spots in the disk. These results are for a single Plasmonic lens modulated using the FPGA and synchronized to the Laser CLK and Optical Encoder events. We have been able to demonstrate lines smaller than 30nm (FWHM) using a single pattern generator.

The vertical lines (along track direction) help us determine the associated uncertainty in space now that we have implemented the FPGA based control of the pattern. The uncertainty of the time delay is 1.6ns (we can put a spot in a closer neighborhood). Thus, the space variation in the radial direction is still around 100nm. This is an improvement for time delay uncertainty from 50ns presented in DSP based system which had space uncertainty of around 500nm.

We also perform experiments for the parallel writing capability of the FPGA-electronics and overall system performance for a dual-lens pattern generator. The set-up for the parallel writing is described in Figure 3.10 A 50/50 beam-splitter separates the source laser beam in two paths (red and green). Two modulators EOMs, pictured in the top left picture, perform pattern encoding in the beams. Notice the Laser CLK source (80MHz) in the picture to the right. Then, after modulation the beams follow almost identical paths but due to the space constraints in the optical table, the red path is longer than the red for few centimeters, thus

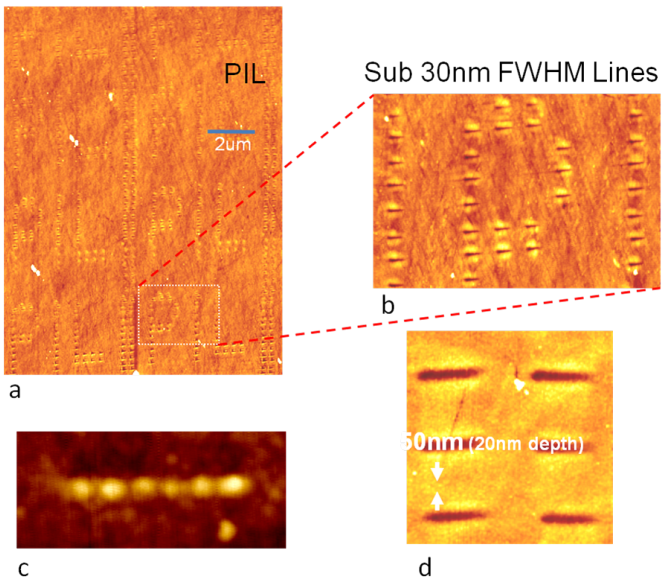

Figure 3.9: *Single Lens Results.*Sub 30nm Single Plasmonic lens experimental results. Time delay is constant with respect to the optical event delay associated with one revolution after. The space variation in the radial direction is still around 100nm (time delay is 1.6ns).

although compensated, still reduces the energy of one of the paths more than the other.

The pattern is sent periodically every optical trigger event. One of the lenses writes "IL" and the other "IP", so that when put close together the pattern will read "IPILI". The patterns are sent through beams red and black color in figure 3.11. The beams are aligned so that an angular difference of 1mrad accounts for the difference in space between the Plasmonic lenses, which were fabricated 4 to 5 microns separated from each other as pictured. Both generators produce signals of the same uncertainty and same as in the single lens case. There is an small difference in the path traveled by both beams, so that the one patterning "LI" has more energy and over exposes the thermal resist, thus the difference in the pattern. One of the beams has a little more divergence because, since they go through different optics and they have not been compensated, the intensity of the two beams is not the same.

The localization of heat due to surface Plasmon localization can be designed to provide a better confinement or a multiple of hot spots in the same structure but for different angle of incidence. Interestingly, we found that by arriving on an angle, the localization of heat in one of the hot spots allowed us to achieve sub 20 nm lines, that is, we have two regions addressable in this lens with a with a much better confinement. The experiment was performed using a single lens pattern generator. It is intention of further work thinking towards having two or more beams addressing the same plasmonic lens and have smaller pitch that way. Lines of 30nm and 20nm width have been patterned by tilting the angle of incidence (these changes were periodically varied) and was achieved using a single lens.

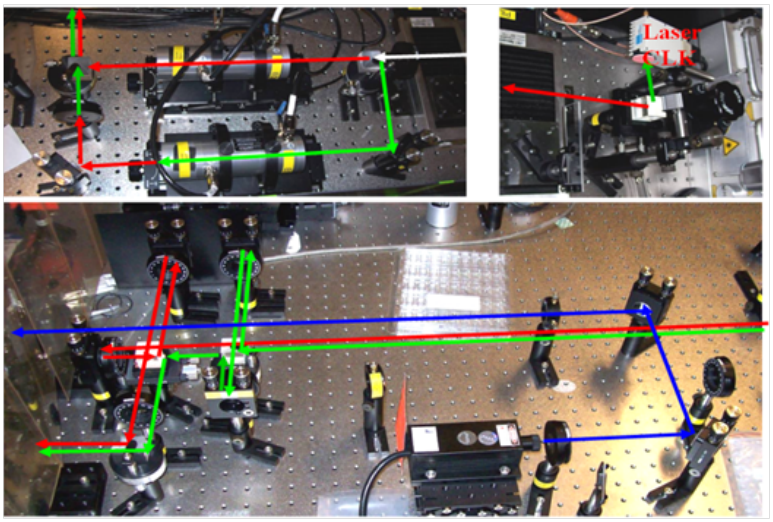

Figure 3.10: *Pictures of the optical set up for the dual-lens experiment.* A, a beamsplitter separates the beam in two (red and green) beam paths. EOMs modulate the separated beams after they cross the beamsplitter. The two paths are optically managed to reduce damage to the optics and optimize the use of the lens focusing on the plasmonic lens.

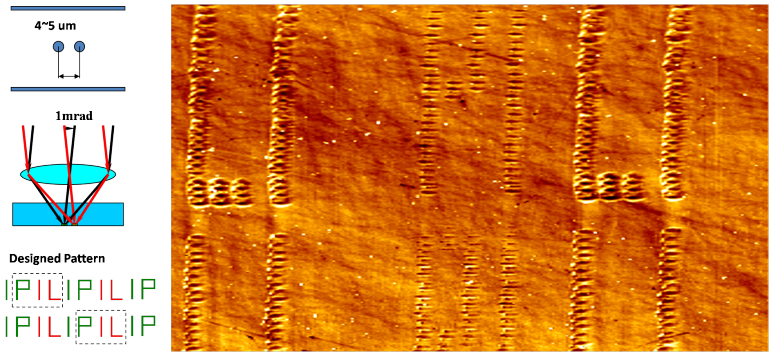

Figure 3.11: *Sub 30nm Dual Plasmonic lens experimental results.* The Plasmonic lenses are spatially separated by few microns. Independent patterns (red and green) are sent through two symmetric beams focused on the lenses. The uncertainty of the electronic time delay is the same for both lenses and same to the single case.

Further configurations will improve the performance of this tool. Accuracy of overlay of subsequent layers is an important issue in application of nanolithography. Regarding the approach of using rotary platform to do lithography, there is no obviously technical barrier that prevents overlay accuracy up to a few nanometers. To realize a better overlay accuracy, it normally requires i) a better rotational stage with smaller lateral run out to minimize the positioning error and ii) high band-width servo system to effectively compensate the positioning error. Next, we will present the design and fabrication of a magnetic encoder to

further minimize the position error.

3.6 Pattern generator with Magnetic Encoder CLK

Accurate position location is compromised not only due to the uncertainty in time delays from the electronic system modulating the laser pulses, it is also a response of fluctuations in the velocity of the spindle in the system (the spindle has approximately an error of 0.1% at the velocity of 2000rpm.). The previous method to measure this was by using the velocity measurement coming from the spindle's optical encoder, which has 1024 line marks per revolution. We used this marks to trigger the event of the EOMs in the system. If we do the calculations, the uncertainty in the position of the spot would be of 0.3um. By using interpolation in the DSP (adding delays) we can reduce the error to only 30nm). However, by introducing FPGA, we improved to 100nm position uncertainty without adding further delays.

As was proposed earlier, a better measurement of velocity can be obtained by having a magnetic encoder embedded in the same spindle of the "to-be-patterned" disk. This allows us to have an improved accuracy of 1pm due to the high density of marks per track already available in commercial HDD technology. The magnetic encoder can have a density as high as 30 Million counts per revolution providing a 1GHz position registered clock signal corresponding to 1pm accuracy. Figure 3.12 shows the schematic of our magnetic encoder. The signals that are relevant now are the laser CLK, the optical trigger, and the magnetic encoder CLK. We use the optical trigger to align data written in the magnetic encoder, however, for patterning purposes only the magnetic trigger has higher priority than the optical trigger and since it is more frequent as well, then the size of the word has to be changed accordingly.

To achieve the implementation of the magnetic encoder, we used knowledge from the existent hard disk drive (HDD) technology. Hard disk drives contain a plurality of magnetic heads that are coupled to rotating disks. The heads write and read information by magnetizing and sensing the magnetic fields of the disk. The disks are magnetized with a series of transitions. The transitions correspond to digital bits. Data is stored on concentric tracks that extend radially across the surfaces of the disks. Each track typically contains a plurality of sectors. Each sector may have a number of data fields. Each data field has a sync field that is used to synchronize the reading of data within the field. For example, when reading data the sync field is used as a timing signal to create a read clock. Data is then read from the disk in accordance with the clock. The sync field is typically written with the writing of data.

There have been developed disk media that have patterns of magnetic dots. The dots are constructed from magnetic material and are separated from each other by non-magnetic material. The non-magnetic materials inhibit cross-talk between the dots. The write clock must be very accurate so that the writing of data occurs above a magnetic dot. Using a conventional sync field to synchronize the write clock may result in undesirable jitter and the

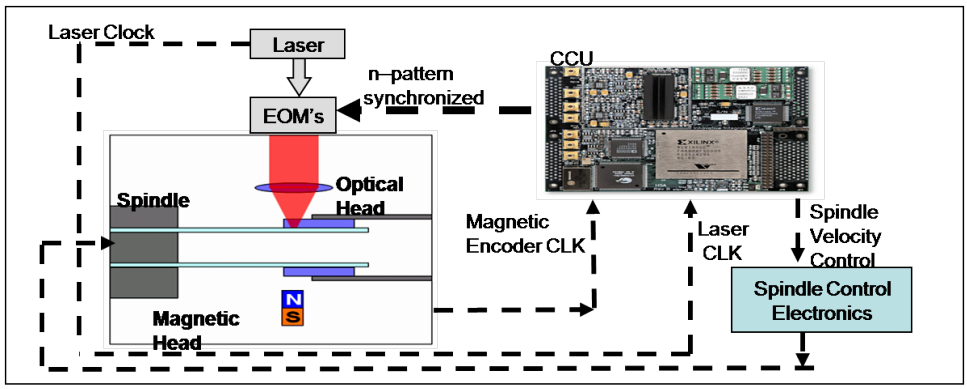

Figure 3.12: *Magnetic Encoder Synchronization Scheme.* The laser CLK is used by the FPGA to synchronize the magnetic encoder to the events of the pattern generator. The magnetic encoder is assumed to have more than 10^6 marks per revolution, which is more than 1024 in an optical encoder, more than enough to allow us for better resolution.

writing of data that is not aligned with the magnetic dots. Writing the sync field with the data will not necessarily result in the proper alignment of data and dots. The misalignment of writing will produce weak magnetic fields and possible cross-talk with adjacent dots.

Here we use a hard disk drive with a patterned disk that has a plurality of sync fields and a plurality of sync marks. The driver further has a controller that causes a head to write onto the patterned disk and synchronizes the writing of data with the sync field and the sync marks. In addition, it can be erased and written in real time to achieve an optimal configuration. Using the advantages of reconfiguration logic, high speed sampling and optimal predictive control algorithms, robust and fast single track reading providing a reliable CLK can be achieved. It is preferred to have this CLK signal coming from a single track in order to reduce time uncertainties due to different space locations.

If a clock is sent in parallel with data, that clock can be used to sample the data. Because the clock must be received and amplified before it can drive the flip-flops which sample the data, there will be a finite, and process-, temperature-, and voltage-dependent delay between the detected clock edge and the received data window. This delay limits the frequency at which data can be sent. One way of eliminating this delay is to include a deskew PLL on the receive side, so that the clock at each data flip-flop is phase-matched to the received clock. In that type of application, a special form of a PLL called a Delay-Locked Loop (DLL) is frequently used. This component has been used in the previous state machine to multiply the frequency of the CLK by 2 and 4 times. In this machine, the component will be used in order to de-skew the magnetic CLK signal.

FSM Modifications on FPGA-PG with Magnetic Encoder CLK

The modifications to the State machine are described in the Figure 3.13. The FSM uses now two triggers (optical and magnetic) to synchronize the Laser CLK events to those excited in the EOMs. Since the Magnetic encoder is closer to the CLK frequency, additional counters are set to monitor the number of bits per magnetic CLK event and the number of magnetic CLK events per complete word. For now, we will count 256 sets of 4 bits (1024 bits). 256 magnetic CLK events will suffice to send a complete word. Additionally, just as before, 1024 optical trigger events will complete a revolution. Continuous bandwidth improvement allows us to set the constraints for the frequency of both, the magnetic encoder CLK and the internal CLK. For now we will continue with the original CLK multiples of 80MHz until we set this bandwidth limit. We set up the Magnetic encoder CLK to run at 160MHz. So that we have 2 CLK events for the State Machine to guarantee that 2 bits are sent. This is performed by first making sure this is a reliable CLK event (oversampling) and then outputting the section of the pattern that corresponds in the row of 256 events like this. By reliable CLK we mean, this signal is on the non-transitory part of the pulse. High frequency events tend to be sharp and oscillatory in the corners, these ups and downs can excite unwanted dynamics in our state machine. We experienced this behavior in the optical trigger falling edge on the previous version of this one. Thus, we can implement a very robust system that oversamples leading and falling edges of a magnetic trigger running at twice the frequency of the running clock.

The oversampling unit does need to run faster than the FSM CLK. This is undoubtedly the best advantage of FPGA logic design, allowing us to perform parallel tasks to the same signal in different CLK domains. Since no further synchronization is expected, so even if it is a CLK of 550MHz, if we count events in the Magnetic CLK, we can count, at most, an additional CLK event to perform safer oversampling. This running CLK is expected to increase with further advances in the integrated circuit industry. Part of that problem is related with the Copper interconnections that are unable to follow electronic transitions at these rates without introducing interconnection issues, raised sensitivity to outside EM perturbations, etc. (Chapter 4). It is expected, that at some point in time the frequency of this logically travelling transitions become less unstable and the interface is reliable enough to allow us to reduce this ratio for a much faster frequency operation.

Later on, we will explain an additional reading and state machine implemented to this same signal with the purposes of studying the temporal evolution of the Magnetic Clock transfer function over CLK regimes were expected CLK contribution might allow us to close a loop in the Control system. Maybe allowing us to intelligently compensate in real time for the perturbations observed and studied using some model predictive control algorithm. In principle, if the oversampling of the leading edge is done fast enough, say on the order of FSM CLK events, then, the pattern generator would be able to delay or not the outputting events for the modulation of the EOMs. Phase evolution studies will be part of the study and described in the next section.

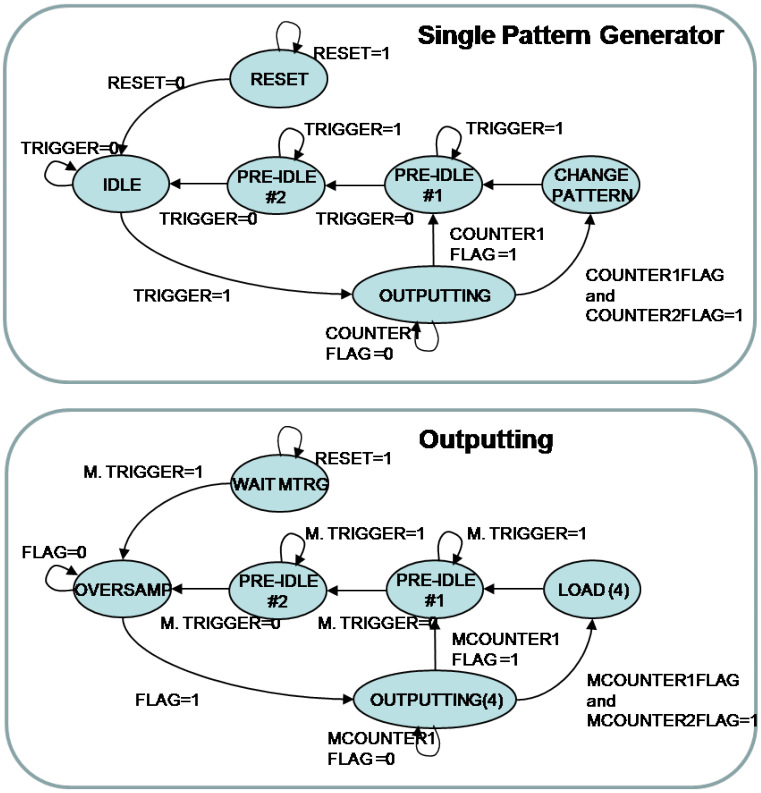

Figure 3.13: *Single Pattern generator and Outputting FSMs with Magnetic Encoder adaptation.* The differences are null. Once the system receives an optical trigger event, the system starts reading the magnetic encoder channel. If leading CLK edge is detected, then an oversampling step verifies for stable pulse event and outputs a sectioned word, the number of times required before the next optical pulse arrives.

3.7 Magnetic Encoder Implementation

For the implementation of the Magnetic encoder we started from scratch, HDDs of commercial vendors were taken apart to interconnect a measuring device and try to decode the various signals coming out of the preamplifier located on the head of the HGA. Unfortunately, no high frequency signal was detected to act as either a CLK or flowing data though the channel. It is very possible that the perturbation to the channel by the simple contacting of additional loads is sufficient to kill the reliability of the information in the channel. Next, we received through Hitachi Corporation, a test-bed system for HGAs that IBM Corporation used almost 10 years ago. Unfortunately, the test-bed system was out of power range to feed the HGA that we were using at that time (A Super-Hawk model by Seagate). The system was tested and repaired several times. The system was studied and improved to the point where considerable amount of re-work of the board was required and thus perturbing sufficiently the integrity of the signal. From the gained experience with the HDD dismantling,

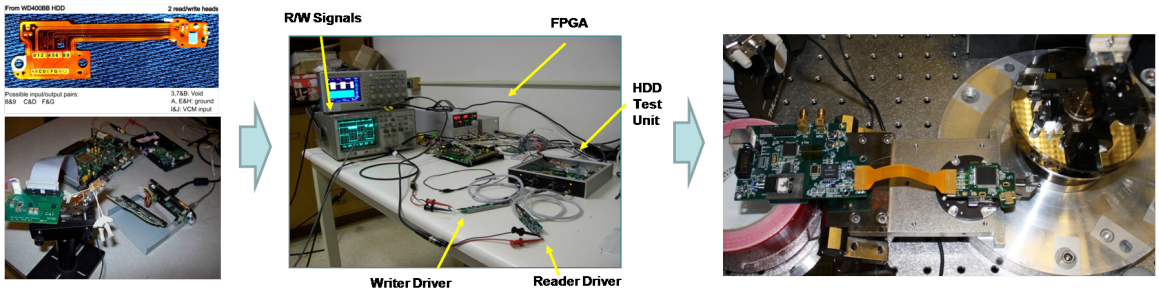

Figure 3.14: *Research endeavors for a Magnetic Encoder.* Interconnected Magnetic Encoder and Magnetic Encoder CLK signal. From a commertial HDD testing setup (back engineer connections and hack a HDD in the search of electronic signals of interest (frequency and amplitude). Pre-amp module interconnected using flexicables to a microcontroller (USB-interfaced to a PC). A module borrowed by Hitachi electronics to test HDDs was repaired and adapted. Commercial solution by using Seahawk heads (by Seagate), a HDD write/read head customized controller.

we decided to stop here our efforts to design a better board.

A very important hint was provided by Seagate Corporation personal. They mentioned that the HGAs that were to be used for writing on a disk should have "head-disk compatibility" in terms of their EM cross-sections. Different (than expected) thicknesses in overcoating might not allow us to induce magnetic transitions with the used potentials. From Seagate we received "combos" of HGA-Recording Media (250 Pharaoh Media and 500 Up-facing DF2 HGA's) but they were unfortunately also outside the range of the Hitachi Test-bed system. The solution that is implemented in this work is from Micro-Physics' corporation and it is shown in Figures 3.14 and 3.15 along with a picture of the Magnetic Encoder CLK signal. It is a compact kit that enables modification of bias current and applied voltages to the HGA electrodes. Also counts with the logic to drive the writer amplifiers at the frequency of external oscillations (From FPGA). We also read the data by an analog channel, which we interface with the appropriate electronics. A comparator (1-bit quantizer) is interfaced to sharpen the pulses and translating them into Low Voltage Differential Signal (LVDS) format. This signal is more robust for higher frequencies and is able (due to theoretical fundaments) to provide a better way to detect the edge of the signal (changes in phase) since it does not depend on the amplitude levels of the input (which fluctuate enough in our system) in the channel.

A series of commands are required to follow the method of writing and reading. If a state machine was to be implemented with the FPGA, a serial interface would then need to be implemented. It would be very similar in design to the previous FSMs due to the communication task common among them. Implementation as a FSM is part of the future work on this section since we would like to be able to control more appropriately the writing and reading of the unit. Once the system is implemented and has been used to write a CLK

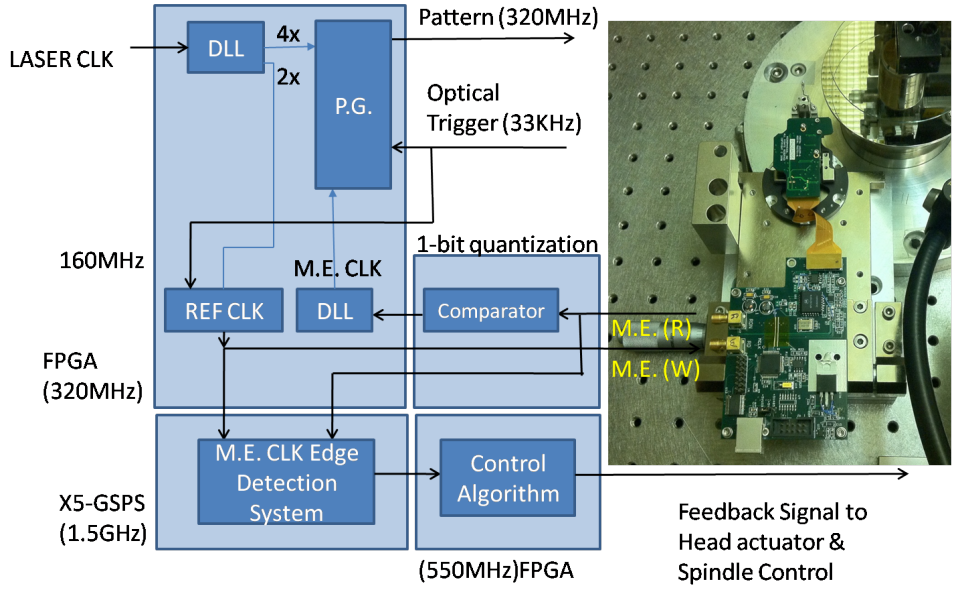

Figure 3.15: *Interconnected Magnetic Encoder and Magnetic Encoder CLK signal.* Left picture shows the FPGA side on the control of the HDD controlling unit for writing and reading purposes. A GSPS board is also included to read at a high BW, signals coming from the encoder to study the evolution of the Clock per track.

track, the reading of the Magnetic CLK is acquired for all future time. It is important to reduce the number of tracks recorded since only then the uncertainty of spot location can be improved. The experiment is performed using a similar lens design. The interface electronics are pretty much similar to the case of optical encoder with the additional preamplifier unit coming from the HDD flying head. With the addition of the comparator and the new FSM controlling the writing of pattern the system is tested at the mentioned frequencies.

Along with the normal operation of the pattern generator, a new unit for the observation of the Magnetic Encoder signal is implemented. The reading is based on the current state of the art in Analog to Digital converters (ADC) at a 1.5 to 3 GHz operating frequency. In reality the whole process is a memory based algorithm capable of saving (in a very generous resource of) memory up to 100 cycles per 320MHZ CLK event. That is 100 CLK events can be collected after a millisecond or so. This allows us to modify pattern generation to optimize the use of time for the best and fastest configuration.

The board used is an X5-GSPS from Innovative integration. This system provides a very high performance DSP core for this application. The close integration of the analog IO, memory and host interface with the FPGA allows for real-time signal processing at extremely high rates exceeding 300 GMACs per second. The X5 XMC modules count with 8-lane PCI Express interface providing over 1 GB/s robust transfer rates to the host. With this system we have been able to sample the transfer functions of the magnetic encoder.

A fourier spectrum of the acquired signal and its degradation after the number of pulses has been driven to a minimum. We find that noticeable phase differences happen when we reduce the sampling time to a number of N cycles. This provides evidence to the constraints the monitoring system has in terms of bandwidth.

3.8 Conclusion

A pattern generator has been designed and reliable transfer of data at high speeds has been implemented. In addition to these tasks, the FPGA is able to provide a feedback signal to improve the functioning of the device and optimize for time delays' disturbances. In fact, there are several ways of actuating on the system and modifying its diverse coupled dynamics. The HGA dynamics and Plasmonic head dynamics are coupled by the spindle dynamics. Both head's positions are monitored by two distinct sensors and can be driven by two different actuators. An interdisciplinary team from several Universities is directing efforts towards fully controlling the fast and accurate nano-positioning skills of our system. From several points of view, we have optimized the system measurements and actuation (methods and technology).

In the vertical direction, displacements are self regulated by the air bearings on the flying heads. The only vertical displacements controlled at the moment are for the purposes of Magnetic HGA to disk separation which can be achieved by measuring the A.E. Sensor and correcting with the Heater of the HGA. In addition, the prefocuing system corrects for additional displacements between the lens and the Plasmonic head which is achieved by driving the Lens Actuator corresponding to the disk measured and corrected for

As was described earlier, "drifting" might cause unwanted x-y displacements along the tracks of both the Plasmonic head and the HGA. However, by prioritizing the Plasmonic head displacements, both the sensor and the actuator bandwidths are set as high as the current state of the art methods allow. The magnetic HGA will count with a radial linear actuator with a bandwidth of 100KHz enough fo us to be able to compensate displacements measured by the x5-GSPS FPGA unit to follow a track and improve the signal integrity of this CLK signal over all time. The signal is predicted to decay over time, if not actuated to correct this drift, the disk might need to be recorded again to improve signal integrity. This modifies the rule and the system needs to reset the DLLs following this CLK. The system also depends on the changes to spindle velocity performed by the Control Unit feed-backing to the velocity of the spindle.

The Magnetic Encoder Dynamics, CLK regulation, by re-writing the Magnetic Encoded rule. By delaying pattern outputting (FPGA FSM). High speed sampling of the Magnetic CLK events can provide information on how much the phase is varied across a track. The actuator that will be located on the HGA and driven to compensate for location is not available yet. However a secondary reading signal coming from the sensor located to track displacements will be located at the position sensor capable of reading position displacements with an accuracy of 1 nm with a bandwidth of 50MHz. The reading of the position signal can

be sampled a frequency close to the FSM pattern generator BW. Modifications to the FSM will be performed on base of the basic building blocks already recognized for the correct and robust acquisition of the signal. These are the results of our current set-up, in particular pay attention to the parallel writing capability of the electronics, and that we have been able to demonstrate lines smaller than 30nm. It is the purpose of the next system configuration to stabilize a process for the high throughput reality of the system presented here.

Our approach, a new low-cost, high-throughput approach to maskless nanolithography uses an array of "plasmonic lenses" that 'fly' above the surface to be patterned, concentrating short-wavelength surface plasmons into sub-100 nm spots. Since these nanoscale spots are only formed in the near field, makes it very difficult to scan the array above the surface at high speed. To overcome this problem we have designed a self-spacing air bearing that can fly the array just 20 nm above a disk that is spinning at speeds of between 4 and 12 m/s, and have experimentally demonstrated patterning with a linewidth of 80 nm. Implemented FPGA Pattern Generator, Reduced electronic time delay uncertainty to 1.6ns, Demonstrated 50nm arbitrary pattern writing capability. Installed parallel writing module for multiple lenses. Demonstrated the first Parallel Plasmonic Lithography Result. Studied and Designed a W/R Control Unit for HDD. Coded Tasks for the FPGA-Based CCN. Magnetic Encoder Interface and Control Routines. Control setup for the preliminary pulsed laser based lithography platform (PIL-Pico) towards prototyping, upgraded PIL-Pico with parallel writing capability and dynamic FH control module. Demonstrated capability of $\tilde{2}0$ nm feature size for both lines & dots. Demonstrated arbitrary pattern writing at $\tilde{5}0$ nm linewidth. Demonstrated first plasmonic parallel arbitrary pattern writing. Demonstrated arbitrary pattern writing at $\tilde{3}0$ nm linewidth. With the fabrication of quasi-3D push-pin design for sub 20nm resolution, the setup of the integration scheme for PNL prototype system using an interferometer approach, a base-stage design, a pre-focusing sub-system, a disk servo system design, and ultimately the upgrade of the FPGA model would keep improving the characteristics of the PNL prototype system.

Bibliography

[277] Shinji Okazaki. “Resolution limits of optical lithography”. In: *Journal of Vacuum Science & Technology B: Microelectronics and Nanometer Structures* 9.6 (1991), pp. 2829–2833.

[278] Hwan J Jeong et al. “The Future of Optical Lithography.” In: (1994).

[279] John Melngailis. “Focused ion beam technology and applications”. In: *Journal of Vacuum Science & Technology B: Microelectronics and Nanometer Structures* 5.2 (1987), pp. 469–495.

[280] EB Cooper et al. “Terabit-per-square-inch data storage with the atomic force microscope”. In: *Applied Physics Letters* 75.22 (1999), pp. 3566–3568.

[281] Richard D Piner et al. “” Dip-pen” nanolithography”. In: *Science* 283.5402 (1999), pp. 661–663.

[282] P Vettiger et al. “The MillipedeMore than thousand tips for future AFM storage”. In: *IBM Journal of Research and Development* 44.3 (2000), pp. 323–340.

[283] TR Groves and RA Kendall. “Distributed, multiple variable shaped electron beam column for high throughput maskless lithography”. In: *Journal of Vacuum Science & Technology B: Microelectronics and Nanometer Structures* 16.6 (1998), pp. 3168–3173.

[284] Mark A McCord. “Electron beam lithography for 0.13 μm manufacturing”. In: *Journal of Vacuum Science & Technology B: Microelectronics and Nanometer Structures* 15.6 (1997), pp. 2125–2129.

[285] Masato Muraki and Susumu Gotoh. “New concept for high-throughput multielectron beam direct write system”. In: *Journal of Vacuum Science & Technology B: Microelectronics and Nanometer Structures* 18.6 (2000), pp. 3061–3066.

[286] R Fabian Pease et al. “Prospects for charged particle lithography as a manufacturing technology”. In: *Microelectronic engineering* 53.1 (2000), pp. 55–60.

[287] Rajesh Menon et al. “Maskless lithography”. In: *Materials Today* 8.2 (2005), pp. 26–33.

[288] Khalid Salaita et al. “Massively Parallel Dip–Pen Nanolithography with 55 000-Pen Two-Dimensional Arrays”. In: *Angewandte Chemie* 118.43 (2006), pp. 7378–7381.

[289] R Fabian Pease. "Maskless lithography". In: *Microelectronic Engineering* 78 (2005), pp. 381–392.

[290] RH Ritchie. "Plasma losses by fast electrons in thin films". In: *Physical Review* 106.5 (1957), p. 874.

[291] William L Barnes, Alain Dereux, and Thomas W Ebbesen. "Surface plasmon subwavelength optics". In: *Nature* 424.6950 (2003), pp. 824–830.

[292] C Genet and TW Ebbesen. "Light in tiny holes". In: *Nature* 445.7123 (2007), pp. 39–46.

[293] Nicholas Fang et al. "Sub–diffraction-limited optical imaging with a silver superlens". In: *Science* 308.5721 (2005), pp. 534–537.

[294] Werayut Srituravanich et al. "Plasmonic nanolithography". In: *Nano letters* 4.6 (2004), pp. 1085–1088.

[295] Xiangang Luo and Teruya Ishihara. "Surface plasmon resonant interference nanolithography technique". In: *Applied Physics Letters* 84.23 (2004), pp. 4780–4782.

[296] Zhaowei Liu et al. "Focusing surface plasmons with a plasmonic lens". In: *Nano letters* 5.9 (2005), pp. 1726–1729.

[297] Ekmel Ozbay. "Plasmonics: merging photonics and electronics at nanoscale dimensions". In: *science* 311.5758 (2006), pp. 189–193.

[298] David B Bogy and C Singh Bhatia. "Design and dynamics of flying height control slider with piezoelectric nanoactuator in hard disk drives". In: *Journal of Tribology* 129 (2007), p. 161.

[299] YF Han, B Liu, and XY Huang. "High air-bearing stiffness slider design". In: *Journal of Magnetism and Magnetic Materials* 303.2 (2006), e76–e80.

[300] Eiichi Ito et al. "TeOx-based film for heat-mode inorganic photoresist mastering". In: *Japanese journal of applied physics* 44 (2005), p. 3574.

[301] Mark I Stockman. "Nanofocusing of optical energy in tapered plasmonic waveguides". In: *Physical review letters* 93.13 (2004), p. 137404.

Chapter 4

Graphene Elecro-optic Modulator

4.1 Introduction

High-Density Information Processing has been efficiently performed by the existent Complementary Metal Oxide Semiconductor (CMOS) technology. In fact, data rates at which we can process information have started to outpace those we use to communicate it among microcontrollers, memory, peripheral devices and connectors. This happens because the interconnections are made from Copper, and this metal cannot keep up with the speed of the electrical variations of the signal. On the other side, high-density information transportation is performed using Fiber optics. By these means, we achieve speeds sufficing and open room for the continuous improvements of High Density Information Processing. It is estimated that billions of optical interconnects will be needed if we were to use fiber interconnections inside microprocessors. Current optical interconnection technology is not made from Silicon thus devices remain bulky, expensive, and difficult to manufacture, and assemble. They cannot be made from Silicon because the commonly used physical effects are very weak or nonexistent. The two major effects are the electro-optic effect, used in lithium niobate based high-speed modulators; and stimulated emission, used in indium phosphide lasers (the source of the optical signal).

Here we will concentrate in the modulation of a signal, thus finding ways to compensate for the electro-optic effect deficiencies of Silicon. Current approaches use the strong free carrier effect to modulate light. Approaches based on this effect designed carefully cross-section configurations to engineer efficient optical modulators. In fact, important recent results rely on controlling free carriers with semiconductor devices. In the case of the silicon modulator, charges are injected by a metal oxide semiconductor (MOS) capacitor to cause a phase shift in the optical input. This chapter states the importance of "siliconizing" photonics for information transport. It reviews the state of the art in silicon-based optical modulators including a brief explanation on the diverse performance metrics for the ideal "CMOS fabrication compatible" optical modulator. Once this is clear, Graphene will be presented and evidence confirming our new approach based on Graphene will show itself important, not

only for the current technology but for the future one Graphene-based nanotechnology.

4.2 Silicon Photonics for Optical-Interconnectors

Optical technology is poised to revolutionize short-reach interconnects [304]. The workhorse of optical interconnects are optical modulators and the most promising technology is based on silicon photonics because it lowers the cost for higher performance [305][306]. The main challenges that Silicon has are its low electro-optic coefficient and its low light-emission efficiency. Engineering efforts have allowed satisfactory optical modulation by the use of resonators or interferometers in very special C-MOS like designs. Still, the balance among different performance metrics sets additional constraints principally in space and in bandwidth for the best designs [307] [308].

The most likely insertion points for integrated photonics into systems will be in places where an extreme amount of data is required to travel in a very small space, for example, in microprocessor data buses or in the backplane of server racks [309]. There have been several advances in the field of integrated photonics in the last few years, most of them directed towards the telecommunication industry at 1.55-?m. The principal goal is the monolithic integration of silicon very large scale integration (VLSI) electronics with silicon nanophotonics on a single silicon chip in commercial state-of-the-art CMOS silicon-on-insulator (SOI) production plant. Photonics-electronics interface will take advantage of current CMOS infrastructure and progress [Reed]. The use of optics for interconnectors has been contemplated not only because offers greater bandwidth, but also, because offers the possible practical benefits.

Silicon is a compelling platform for both practical and technical reasons. From an economic perspective, the benefit is the infrastructure, toolsets, and knowledge that have been developed for silicon microelectronics. Continuous development based on Silicon is expected to remain into the near future if silicon photonics maintain a degree of compatibility with the microelectronics already in process at these facilities. In addition to "drafting" on microelectronic progress, silicon photonics will also benefit from the techniques under development in micromachining, such as those used for micro-electromechanical-systems (MEMS) devices. These techniques can be used to create silicon optical benches for hybrid assemblies or to simplify assembly through the direct attachment of fibers and external light sources by using different coupling mechanical mechanisms. The greatest benefit of silicon photonics is the promise of integration of different types of devices into the silicon platform. Materials such as silicon dioxide support passive devices to route light but does not have high-speed active devices to manipulate light. Active materials such as indium phosphide require re-growths to integrate different types of devices reducing considerably the yield in the fabrication process. Silicon, on the other hand, has both active and passive capabilities and the potential to integrate them with much higher yield. Photonic devices could even be monolithically integrated with electronics if CMOS compatibility is maintained, there will be less optical loss due to the elimination of fiber interfaces, and we will be able to process light in ways that

could never be done and at costs low enough to allow these devices to become as common as transistors.

Silicon Optical Modulator

An optical modulator is a device that is used to modulate a light beam propagating either in free space or in an optical waveguide. These devices can alter beam parameters such as amplitude, phase or polarization. Modulators can be also classified as either electro-refractive or electro-absorptive. Applying an electric field to a material may change its real and imaginary refractive indices. A change in the real part of the refractive index (Δn) is known as electro-refraction, whereas a change in the imaginary part of the refractive index (κ) is known as electro-absorption.

The primary electric field effects that are traditionally useful in semiconductor materials for causing either electro-absorption or electro-refraction are the Pockels effect, the Kerr effect and the Franz-Keldysh effect. Unstrained pure crystalline Si does not exhibit linear electro-optic (Pockels) effect and the refractive index changes due to the Franz-Keldysh effect and Kerr effect are very weak at the telecommunications wavelengths of 1.3 μm and 1.55 μm (references [311], [312]).

In Silicon, the complex effective refractive index of the structure is varied in order to produce a phase or intensity modulation. The main methods to alter the refractive index in Si are the thermo-optic effect and the plasma dispersion effect. The thermo-optic effect can be used only up to 1 MHz modulation frequency, too slow for the high frequencies required by modern telecommunications applications. The free carrier dispersion effect is used to change electrically both the real refractive index and the optical absorption coefficient.

Soref and Bennett [331] studied the refractive index change Δn from absorption measurements for a wide range of electron and hole densities, over a wide wavelengths spectrum. Changes in both the refractive index and absorption generated the following expressions for Silicon at a wavelength of 1.55 μm.

It was calculated that a change in carrier density on the order of $510^{17} cm^{-3}$ results in a Δn of $\sim 1.6610^{-3}$ at a wavelength of 1.55 μm. A reduction in intensity due to the absorption of free carriers is also observed [314]. The free-carrier concentration in Si electro-optic devices can be varied by injection, accumulation, depletion, or inversion of carriers. P-i-n diodes [310] [311] and metal-oxide semiconductor field-effect-transistors [312] [313] may be employed for this purpose.

In a MOS structure (for all configurations) the variation of a large concentration is possible within few tens of nanometers beneath the insulated gate region. A small overlap between the optical mode and the non-equilibrium charge distribution in the waveguide is created, leading to a small effective index variation. Additional advantages are negligible dc power consumption and by localizing the refractive index change under the gate electrode, no carrier confinement methods (isolation trenches in a p-i-n diode) are needed. Also, the micron-size MOS-based high index-contrast SOI waveguide for high-speed electro-optic

modulation is designed for strong light confinement. This enhances the effect of small index changes, enabling an ultra-compact structure with high modulation depth.

The accumulation condition scheme provides high modulation depth for very low power consumption. Switching time is calculated to be 1.29 ns, limited by carrier diffusion only (a carrier injection process). The use of a MOS diode should lead to higher speed operation since the carrier distribution in the semiconductor is governed by a drift mechanism (electric field).

State of the Art in Silicon-based Optical Modulators

We have discussed how changes in the refractive index induce absorption in Silicon. The process of inducing absorption directly modulates the intensity of the propagating mode. To date, proposed Silicon-based optical modulators using a MOS configuration under accumulation conditions lead to the modification of the refractive index and result in a phase shift in the propagation of the optical mode. The advantage of this configuration is the high modulation speed [332], as there are no slow carrier generation and/or recombination processes involved. However, the change in the refractive index is small and in order to induce a significant modulation depth a very long structure, on the order of millimeters, is required. Two options are available for converting a change in refractive index into intensity modulation. First, the refractive index change can shift the relative phase of two propagating waves such that they constructively or destructively interfere. A Mach-Zehnder interferometer (MZI) can be used to realize this. Second, placing a resonant structure in the device constrains the induced refractive-index change to happen according to the resonant condition, thus permitting the device to be switched on- and off-resonance states at any wavelength.

Recently, an optical modulator based on an MOS configuration and a silicon waveguide Mach-Zehnder interferometer has demonstrated modulation speeds exceeding 10 Gb/s [333]. Although this device remains the fastest silicon optical modulator reported so far it is only useful as a discrete device due to its large size, on the order of millimeters. In order to reduce power consumption and device footprint, it was shown that the size of the modulator can be reduced by embedding the waveguide into a high-Q resonator [334] [335] [336] [337] [338]. This reduction in size is performed to the expense of drastically narrowing the bandwidth and increasing the temperature sensitivity, which constitutes one of the major disadvantages of using resonators in the design of modulators [339]. Modulators have been improved dramatically with an increase in bandwidth from the MHz to the multi-GHz regime [108].

More recently, extensive research is being performed on alternative modulation mechanisms in other materials compatible with silicon, such as germanium, to achieve a better optical modulator. The quantum-confined Stark effect (QCSE) is an electric-field-induced change in the optical absorption. In fact, the Franz-Keldysh effect is the limit of the QCSE as the quantum-well layers increase in thickness. The QCSE has spectrally abrupt and stronger changes in the absorption coefficient [307], and it is measured in quantum well devices in which the electron and hole confinement provided by the barriers allows for exciton enhancement of the optical absorption. However, to use these effects on a silicon platform

we need a second material, which adds complexity to the fabrication of the device. The first demonstration of the QCSE in pure Ge quantum wells and Ge-rich SiGe barriers on Si was carried in reference [343]. Structures exhibiting the QCSE were integrated into modulator devices, demonstrating electro absorption modulators [46]. This experiment provides enough evidence to envision high speed, efficient QCSE modulators in the future although with complex fabrication requirements. Further modulation options are available by creating hybrid materials of silicon and other photonic materials, or through the manipulation of the crystalline material.

Performance Metrics

There exist various figures of merit used to characterize a modulator. Some of these are modulation speed and depth, optical bandwidth, insertion loss, area efficiency (footprint) and power consumption.

The modulation speed or bandwidth is the most important figure of merit for an optical modulator. The speed of a modulator is commonly characterized by its ability to carry data at a certain rate. Modulation bandwidth is defined by the frequency at which the modulation is reduced to 50% of its maximum value.

The modulation depth or extinction ratio is defined as the ratio of Imax, Maximum transmitted intensity, to Imin, the minimum transmitted intensity. It is expressed in decibels as 10log(Imax/Imin). A large modulation depth is used in long-distance transmission, affordable bit error rates and receiver sensitivity. A modulation depth of > 7 dB is preferred for interconnectors.

Insertion loss accounts for the optical power passively lost (reflection, absorption and/or mode-coupling losses) when the modulator is added to the photonic circuit. It contributes to the link budget (receiver sensitivity) and to the overall losses in the system. For example, submicron waveguides (to increase performance) add an increase in loss from coupling and modal interaction with sidewall roughness.

The energy per bit or power per bit is the energy expended or the power consumption in producing each bit of data. Adoption of optical interconnects might be justified to some extend if power consumption is not higher than that of electrical interconnects. Future systems will need to have power consumptions of less than 1 pJ per bit.

The performance metrics of an interconnect system are linked in a simple way, making it easy to trade-off performance among areas. For example, the performance enhancements gained by reducing the cross-section of a device should be evaluated against any increase in loss that results. Also, a small modulator will result in a small extinction ratio, but also small footprint and power consumption. Thus, it is possible to optimize performance for a given application.

4.3 Graphene-based Optical Modulator

In the previous sections we presented the motivation underlying the need of having a small CMOS-compatible device capable of modulating optical pulses in a broad frequency range. We understand the configuration that best uses the plasma dispersion effect in a Silicon waveguide to provide a change of phase in the transmitted signal. New materials can provide what Silicon needs in such a configuration to improve its performance. Here we present a new approach based on the superior properties of graphene (a single atomic layer of graphite) for achieving a strong optical modulation of a mode in a Silicon waveguide. Instead of inducing a free carrier density change in Silicon, we use a graphene based capacitor-like structure to vary charge density in a region where the optical mode is confines its energy. We demonstrate an efficient optical modulation that combines large bandwidth with small footprint and low operational voltage. Furthermore, the design is fully compatible with standard CMOS technology but even better it is coupling Silicon photonics to carbon electronics. This chapter starts by presenting graphene, its electronic structure, and its optical properties. Secondly, the design of the device, its fabrication process and its characterization for proper measurement are explained. Optical Measurements and Results are discussed. Conclusions and further work is presented last.

Tuning Optical transitions in Graphene

Graphene is a single atomic 2-dimensional system composed of carbon atoms arranged in a hexagonal honeycomb lattice. The most remarkable property of graphene is the linear energy dispersion, implying a vanishing effective mass, a high Fermi velocity (1/300 of the speed of light), and a high electrical mobility of approximately 200,000 cm2/Vs for a free sheet of both electrons and holes [44], [96], [318], [320] [321]. Moreover, despite being only a single atom layer, it can absorb photons broadband from the visible to the infrared spectral range. The strength of the inter-band transition in graphene is one of the largest in all known materials [320], [104][322]. Multiple graphene layers absorb additively and most important the absorption range of the system can be tuned by changing the Fermi energy level using an external gate field [321][322]. Not only does graphene possesses superior light absorption, carrier mobility, current carrying capability, and thermal conductivity, it can also readily incorporate electrical coupling as in field-effect devices [315] and p-n junctions [105][106] [347].

The special behavior of graphene arises due to its two-dimensional (2D) structure that confines electrons in a single atomic layer and its low density of states (DOS) near the Dirac point, which causes the Fermi energy (EF) to shift significantly with variation of the carrier density. Graphene is the first known truly two-dimensional solid but its uniqueness also rests on the fact that it has a singular band structure: its valence and conduction bands touch each other [348]. In the absence of doping, the Fermi level in graphene lies at an energy which belongs to both bands and corresponds to the Bloch states in the corners of the hexagonal Brillouin zone of the honeycomb crystal. This defines graphene as a gapless

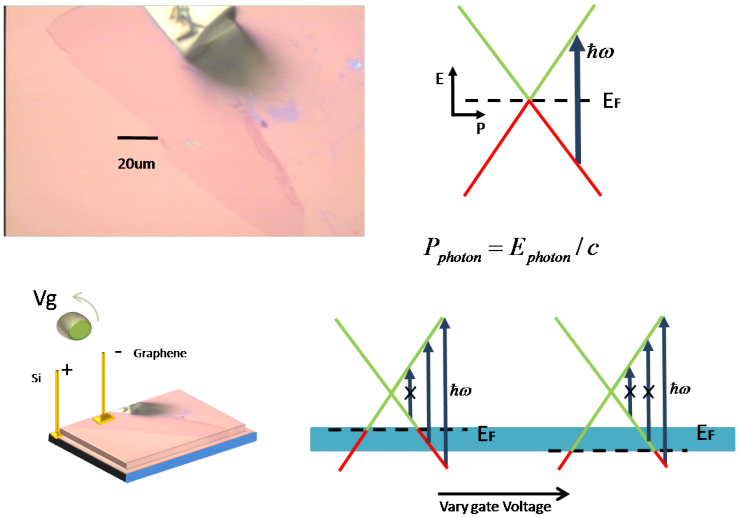

Figure 4.1: *Graphene interband transitions modulated by means of Electric Field.* A, A monolayer of graphene 130um long, B, Electron from occupied state to empty state happen by vertical transitions due to momentum conservation.

semiconductor, making a continuous variation of carrier density from electrons to holes possible. For a zero chemical potential one cone of each pair is fully occupied whereas the other is completely empty. Through application of an external potential [95] the states in the upper unoccupied cone can be populated with electrons and by reversing the sign of the potential, holes can be introduced in the lower energy cone. Hence, an applied voltage changes the charge-carrier density in graphene by $n = \alpha(V + V_0)$ and accordingly shifts E_F , where $E_F = sgn(n)\hbar\nu_F\sqrt{\pi|n|}$. Here, positive (negative) n means electron (hole) doping, ν_F is the Fermi velocity, $\sim 710^{10} cm^{-2}V^{-1}$(estimated from a simple capacitor model), and V_0 is the offset voltage caused by natural doping. Figure 4.1 shows the modulated transitions on graphene. The shift in E_F due to the altered electron density results in a modification of the light absorption in graphene. For example, a lowering of E_F eliminates optically induced transitions (and therefore absorption) originating from initially occupied electronic states [321].

Device Concept: Design and Fabrication

In the following, we utilize the effect that the light absorption of graphene can be modified by changing the Fermi energy level EF with an external gate field. Based on the absorption change we demonstrate an efficient optical modulator that combines large bandwidth with small footprint and is fully compatible with standard CMOS technology.

An overview of our optical modulator is schematically shown in Figure 4.2. We fabricated a 50-m-long Silicon ridge waveguide using conventional nanofabrication processes on a Silicon-on-Insulator (SOI) wafer (see methods section). For light coupling in and out of

the waveguide we used grating couplers optimized for 1500 nm wavelength. The waveguide has a 90 degree bend with the only purpose of increasing the signal-to-background ratio of our detection system. For applying voltage bias to the waveguide a narrow Silicon bridge to a contact pad was included. In a further step a 30-nm-thick Aluminum oxide layer was deposited using Atomic Layer Deposition (ALD). This layer will act as the gate oxide to insulate the graphene from the Silicon waveguide, enabling us to use the Silicon as gate electrode. The scanning electron microscopy image of the fabricated modulator is shown in Fig. 4.2(a). The image shows the Silicon waveguide and the Graphene sheet that is covering the waveguides, but was removed from the nearby Silicon electrodes (for details see the appendix). The electrical connections resulting from our process can be found in Fig. 4.2(c). The electrical contact for applying an external voltage bias are realized by directly contacting one electrode to the Graphene sheet and a second to the Silicon contact pad which is connected by a Silicon bridge to the waveguide. A digital source-meter instrument is used both as a highly stable DC voltage source and a current meter.

Optical Field Distribution and absorption coefficient

Several types of waveguides with different geometries and light-guiding mechanisms can be used in silicon. In general, the geometry of the waveguide depends on the device in which the waveguide is incorporated. Waveguides with large cross-sectional dimensions are usually integrated in devices requiring propagation over relatively short straight paths with no bends while waveguides with smaller cross-sectional dimensions are used in devices requiring long lengths. Waveguides with large cross-sectional dimensions are usually easier to couple to the input and output of a typical $10 - \mu m$ core fiber. They require a large bending radius, however, and therefore, devices based on waveguides are usually discrete since on-chip integration is difficult. Waveguides with smaller cross-sectional dimensions suffer from high coupling losses due to the difference in size between the mode of a fiber and that of a waveguide. Their small dimensions, however, enable ultracompact devices to be integrated on-chip. Also, as we describe below, their high-confinement nature offer the ability to enhance light in small regions, enabling novel active devices like modulators and amplifiers by effectively enhancing the optical properties of silicon in these regions.

The most standard waveguides used for silicon photonics are channel waveguides and ridge waveguides. In channel waveguides, the guiding layer is completely surrounded by a cladding layer, while in ridge waveguides, the guiding layer consists of a slab with a dielectric ridge on top embedded between two low-index-of-refraction layers (the top layer can also be left uncladded). The dielectric ridge creates an effective-high-index region just below the ridge, with a slightly higher effective index than the index of the slab. In both the channel and the ridge waveguides, light is confined due to total internal reflection between the high- and low-index-of-refraction region. The typical cross-sectional dimensions of these two waveguide configurations are determined by the effective refractive index n_{eff} in the guiding region, which determines the degree of light confinement in the core. Channel waveguides typically have submicrometer cross-sectional dimensions due to their larger effective index

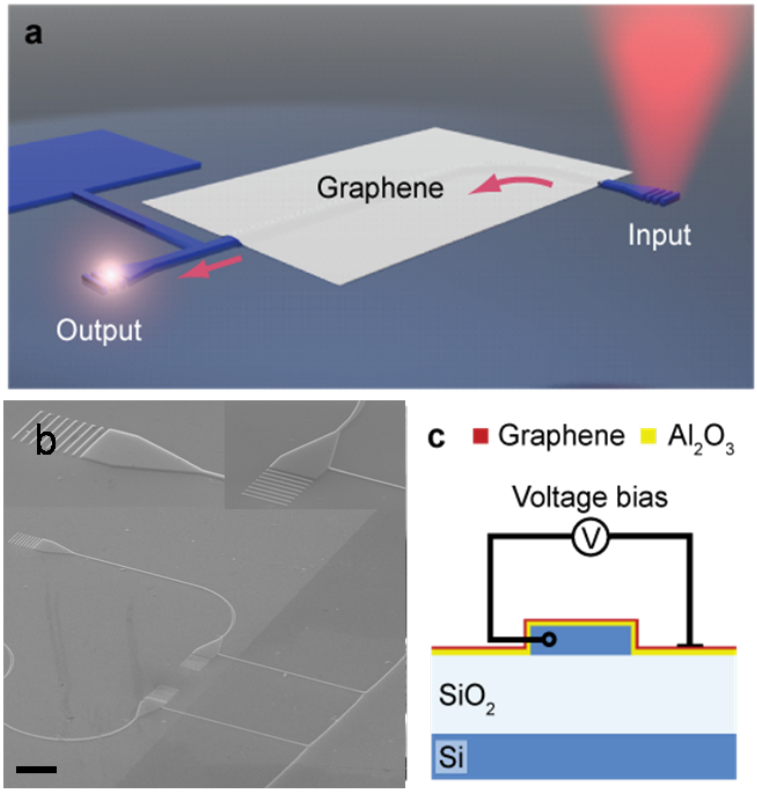

Figure 4.2: *Schematic diagram showing the configuration of a graphene-based electro-optic modulator using silicon-on-insulator technology.* A. Silicon waveguide is fabricated on a SOI wafer, Aluminum Oxide is used as gate oxide. Thickness determines the Power usage of the dispositive. Typical values in our measurements for the gate oxide thickness are from 6 to 20nm. B. An SEM image of a working device. Graphene can be seen as, it was removed from the Silicon electrodes but left on top of the Silicon waveguides. C. Cross-sectional view of the waveguide. The thickness of the Silicon Oxide on the SOI wafer is 1.6um, whole Silicon in the waveguide has a thickness of 250nm.

($n_{eff} \sim 3$). Ridge waveguides, in contrast, enable relatively large optical modes, on the order of a few micrometers, to be confined in silicon without sacrificing single-mode operation [335], [336], despite the fact that the high index contrast between silicon (core) and oxide or air (cladding) seems to imply a small mode size. This is due to the ridge-waveguide geometry that induces a relatively low effective index ($n_{eff} \sim 2$) [306].

The waveguide exhibits single mode operation for both TE and TM polarization modes in the wavelength range of 1500 nm. Optical coupling is achieved by using gratings and a taper at the ends of the waveguide. The best performance of the modulator can be obtained for a large overlap of the optical mode with the gated graphene layer. Figure 4.3a shows the optical field distribution for a quasi-TM mode in the waveguide structure obtained by eigenmode

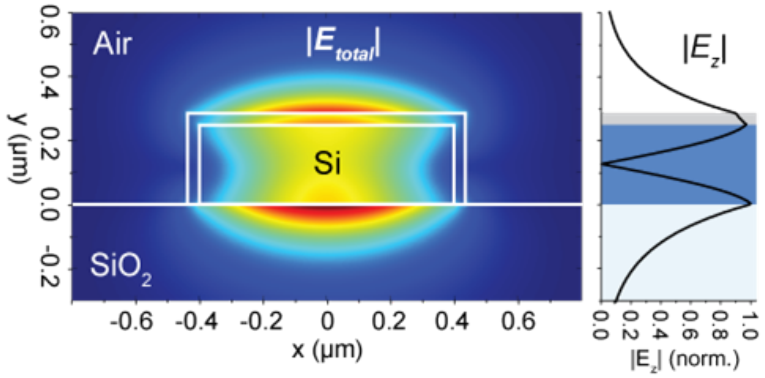

Figure 4.3: *The optical field distribution of our ridge waveguide.* The Electric component along the propagation of the waveguide is shown on the side. As can be seen, the interface with graphene is optimized for a better interaction between the optical mode and graphene, where the charge carrier density fluctuations can be electrically controlled.

analysis. For the chosen geometry the mode shows strong localization of the electric fields near the top (air) and bottom (substrate) interface. Note, the interface to the air half space is covered by a 30-nm-thick cladding layer of aluminum oxide to electrically separate the graphene from the Silicon. Graphene as a 2D material possesses strongly anisotropic material properties. Only light with the electric field in-plan with the graphene will experience a strong absorption. This leads to the conclusion that only the electric field component of the optical mode in the x-z plane at the top waveguide interface can be influenced by the absorption. The quasi-TM mode from Figure 4.3a has a strong component in y and z direction but not in x direction. Hence, mainly the z component (Figure 4.3b) of the electric field (in propagation direction) will determine the performance of the modulator. However, this field component is strong at the interface top interface where the charge carrier density of graphene can be tuned by using as the back gate doped Silicon waveguide underneath the aluminum oxide.

Based on the electromagnetic field distribution for the optical mode in the waveguide and its spatial overlap with the graphene layer we calculate the absorption coefficient for the waveguide mode by

$$\alpha_{WG} = \frac{\frac{\omega}{2}\int Im\{\varepsilon(x,y)\cdot E(x,y)\cdot E^{*}(x,y)\}dxdy}{\frac{1}{2}\int Re\{E(x,y)\times H^{*}(x,y)\}dxdy} \tag{4.1}$$

where $E(x,y)$ and $H(x,y)$ are the electric and magnetic fields, respectively, and ω the angular frequency of the light. Since the imaginary part of the permittivity tensor determines the power loss in the system we have to assign a reasonable permittivity value to the graphene sheet. Based on Ref. 18 we estimate the absorption coefficient for a single layer graphene to be $\alpha_g = 4.410^9 cm^{-1}$ for a wavelength of 1500 nm and in-plane electric field vector.

From this value we determine an anisotropic permittivity whereas we are only interested in the imaginary part (see Eq. 4.1) and neglect the real part. Under the assumption that $Re(n_g \approx 1)$ we obtain for the permittivity of a graphene layer in the x-z plane imaginary part of $Im(\varepsilon_g^{xx} = Im(\varepsilon_g^{zz} = 10.4)$ and $Im(\varepsilon_g^{yy} = 0)$. In our calculation we assume that only the top surface of the waveguide (x-z plane) is covered with graphene and contributes to the absorption. Since all other materials have an negligible imaginary part in α, we can estimate the absorption coefficient for the fundamental waveguide mode as $\alpha_{WG} = 358cm^{-1}$. In the case the loss of the graphene can be completely removed by modifying the Fermi energy level with the voltage bias a $50\mu m$ long waveguide would lead to a change in the transmission of -7.7 dB ($0.154dB \cdot \mu m^{-1}$).

4.4 Graphene Electro-optic Modulator Fabrication

The fabrication of graphene-based electro-optic modulators uses Silicon on Insulator (SOI) wafers as the starting substrate. Electron-beam lithography is used to define the Silicon waveguide, gratings and electrode. By using an electron-beam (e-beam) evaporator, Chromium was deposited on the defined windows to act as mask for the anisotropic Silicon etch step which was performed in a parallel plate plasma etching system using SF6 as the etching gas. Once the Chromium mask is removed, Aluminum Oxide (10nm) is deposited using Atomic Layer Deposition (ALD) process. Graphene is transferred from its Cupper-based graphene synthesis substrate. A second electron-beam lithography step is used to define windows to etch the graphene resting on top of the Silicon electrodes. An electrode of Cr/Au (10nm/50nm) is deposited on graphene by using e-beam evaporator. The sample was wire-bonded to a sample-holder by using an ultrasonic wedge wire bonder for Al-1% Si wire with 0.00125" in diameter. Figure 4.4 shows few steps of the concluding fabrication process.

Figure 4.5 shows characterization pictures of or device. Graphene is Raman confimed, as well as AFM and SEM to guarantee its proper operation before wirebonds and device test.

4.5 Experimental Results

We used a femtosecond synchronously pumped optical parametric oscillator as a tunable light source to determine the performance of the modulator at different wavelengths. The beam with less than 1 mW power was focused on the grating coupler to launch the quasi-TM mode in the waveguide. The light from the output coupler was imaged in back reflection to a charge-coupled device (CCD) camera to measure the output intensity. Figure 4.6 shows the dependence of the optical transmission through our device on the gate-voltage for a $50\mu m$ long waveguide at 1,540 nm. The transmission is normalized with respect to the maximum transmission at negative voltage bias. For our measurements we connected the graphene layer to ground and a negative voltage was applied to the Silicon waveguide (back gate).

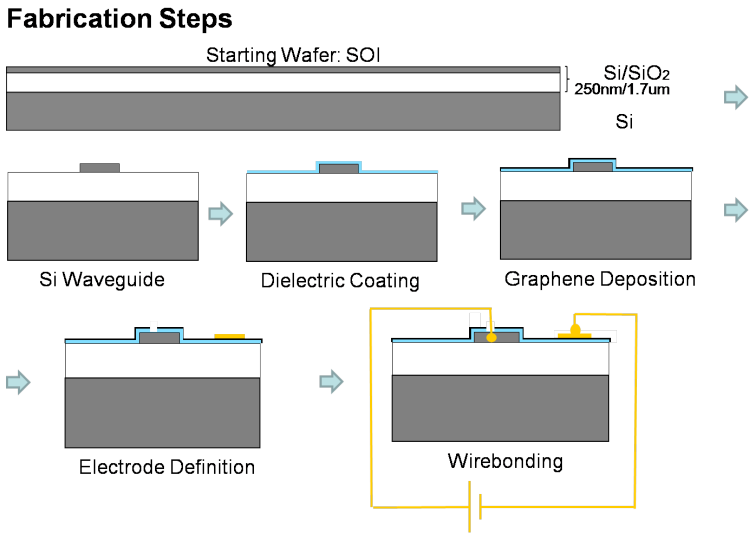

Figure 4.4: *Fabrication details of the Graphene-based Eleoctro Optic Modulator.* SOI wafer is patterned using Electron-beam lithography to define the Silicon waveguide. Anisotropic Silicon etching defined the waveguide in Silicon. Aluminum Oxide (10nm) is deposited using Atomic Layer Deposition (ALD). Graphene subsequentely transferred and the device is wirebonded to the sample holder.

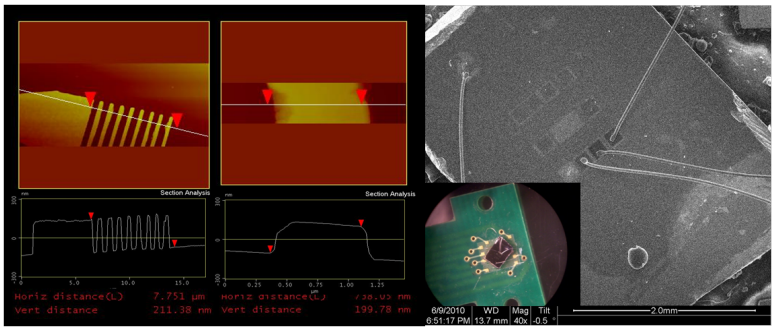

Figure 4.5: *AFM and SEM pictures of our device.* A, AFM pictures of the gratings and waveguide cross-section on Silicon. B, Shows an SEM picture of the wirebonded device. In the inset an optical picture of the sampleholder ready for measurement is also shown.

We observe a strong change of the transmitted intensity for a voltage bias of $-2V$. This sharp drop in optical transmission for voltages $> -2V$ results from the increased absorption coefficient of graphene which leads to a strong attenuation of the optical field during the propagation. Within a range of 5 V for the voltage bias a modulation of -6 dB is observed for only 50 μm propagation length. This value is in good agreement with our estimation based on the absorption loss of the graphene. The high modulation over short propagation lengths allows devices with small footprint size that can be modulated by electrical signals

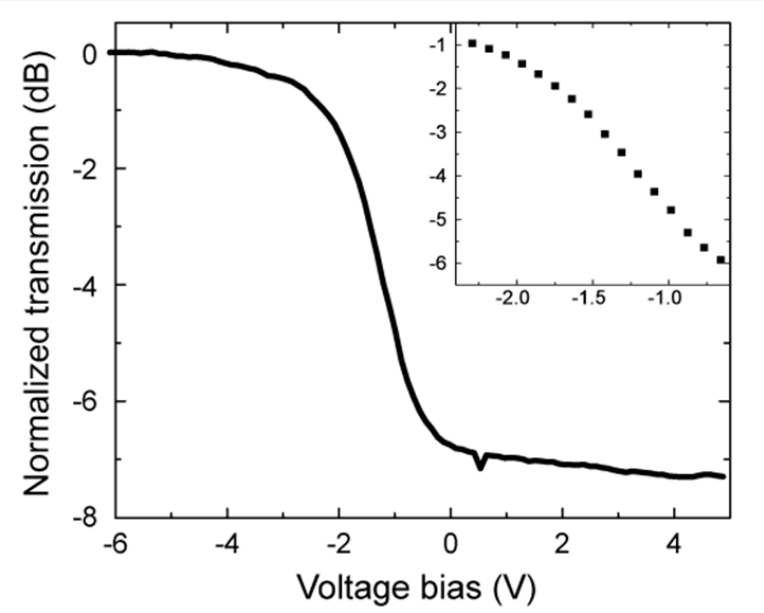

Figure 4.6: *Transmission change with respect to Bias Voltage of the Graphene-based electro-optic Modulator in 50um long Silicon waveguides* As shown in Figure 4.4 at a wavelenght of lamda = 1.54um. Transmission change occurs in a sharp 0.2/V applied. The inset shows better resolution in the 0 to -3 V

and are robust to mechanical changes at the same time.

As mentoned earlier, a modulator based on graphene will be immune to changes in the temperature of the substrate. Moreover, the configuration of our system can be easily modified to adapt suspended graphene configuration.

Also, Graphene–a sheet of carbon atoms linked in a honeycomb structure–transports electrons tens of times faster than III-V semiconductors. That means that graphene modulators could work at extremely high frequencies, making them highly efficient at detecting light and transporting the resulting electrons to an external circuit. The material also absorbs wavelengths ranging from visible to infrared, whereas thin layers of III-V semiconductors don't absorb many infrared frequencies Changes Figure 4.7 shows the frequency response at different wavelengths, ranging from 1,430 to 1,560 nm. Since the gratings for the waveguide are designed for the wavelength 1500nm, a wider range of wavelengths is not covered. But, a different grating design should relocate the expected contrast in another wavelength range.

4.6 Conclusion

The inclusion of graphene as a switchable absorbent media into Silicon photonics devices allows the design of efficient and broadband optical modulators. With proper optimization of the structure's size and geometry, ultrafast devices with modulations speeds comparable to

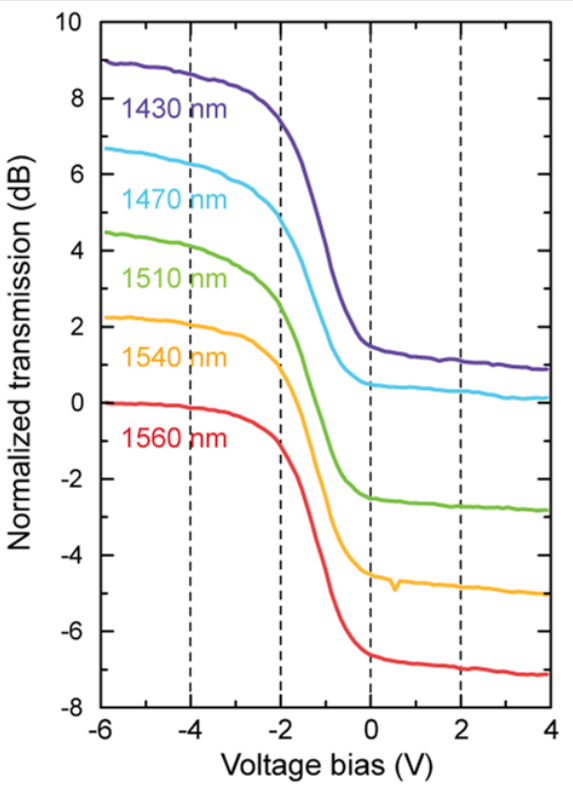

Figure 4.7: *Wavelength dependence from 1430 to 1560 using a gratting designed for 1550 nm.* The performance of the device depends on the grating period and not on the material used for modulation. For other frequencies, smaller or larger than the range, the transmission is reduced only due to the grating design.

traditional electronic devices should be within reach. The design is fully CMOS-compatible and allows the use of standard semiconductor fabrication processes. Due to the unique properties of Graphene the device operates in a broad frequency spectrum and is more robust against environmental temperature changes than resonator based designs. In addition, one can envision, the future of electronics and of photonics by having one of the most attractive materials in nature, graphene on the most efficient and useful substrate in nature, Silicon.

The channel and ridge waveguides described above are based on the principle of total internal reflection, where light is concentrated in the high-index-of-refraction region of the waveguide. In addition to these waveguides, a silicon platform, due to its especially high index of refraction (in contrast to glass materials, for example), enables other novel types of waveguides where light can be confined in low indices of refraction regions (as air). These are photonic crystal waveguides and slot waveguides, Which are not to be discussed here, a good reference is written by Lipson et.al. [306] Silicon offers an ideal platform for creating photonic crystals with complete band gaps due to its high index of refraction. These optical waveguides are usually formed by removing materials from a 2-D photonic crystal, for creating channels

in the crystal through which light can propagate. In the plane of the crystal, light can interact with graphene and interact in additional novel devices.

Bibliography

[304] Richard A Soref. "Silicon-based optoelectronics". In: *Proceedings of the IEEE* 81.12 (1993), pp. 1687–1706.

[305] Graham T Reed et al. "Silicon optical modulators". In: *Nature Photonics* 4.8 (2010), pp. 518–526.

[306] Michal Lipson. "Guiding, modulating, and emitting light on silicon-challenges and opportunities". In: *Journal of Lightwave Technology* 23.12 (2005), p. 4222.

[307] JE Zucker et al. "Miniature Mach-Zehnder InGaAsP quantum well waveguide interferometers for 1.3 mu m". In: *Photonics Technology Letters, IEEE* 2.1 (1990), pp. 32–34.

[308] Jeffrey S Cites and Paul R Ashley. "High-performance Mach-Zehnder modulators in multiple quantum well GaAs/AlGaAs". In: *Lightwave Technology, Journal of* 12.7 (1994), pp. 1167–1173.

[309] M Fetterman, C-P Chao, and SR Forrest. "Fabrication and analysis of high-contrast InGaAsP-InP Mach-Zehnder modulators for use at 1.55-μm wavelength". In: *Photonics Technology Letters, IEEE* 8.1 (1996), pp. 69–71.

[310] O Leclerc et al. "Polarisation-independent InP push-pull Mach-Zehnder modulator for 20 Gbit/s soliton regeneration". In: *Electronics Letters* 34.10 (1998), pp. 1011–1013.

[311] Tatemi Ido et al. "Ultra-high-speed multiple-quantum-well electro-absorption optical modulators with integrated waveguides". In: *Lightwave Technology, Journal of* 14.9 (1996), pp. 2026–2034.

[312] T Fujiwara, A Watanabe, and H Mori. "Measurement of uniformity of driving voltage in Ti: LiNbO/sub 3/waveguides using Mach-Zehnder interferometers". In: *Photonics Technology Letters, IEEE* 2.4 (1990), pp. 260–261.

[313] Ed L Wooten et al. "A review of lithium niobate modulators for fiber-optic communications systems". In: *Selected Topics in Quantum Electronics, IEEE Journal of* 6.1 (2000), pp. 69–82.

[314] MM Howerton et al. "Fully packaged, broad-band LiNbO¡ sub¿ 3¡/sub¿ modulator with low drive voltage". In: *Photonics Technology Letters, IEEE* 12.7 (2000), pp. 792–794.

[315] KS Novoselov et al. "Electric field effect in atomically thin carbon films". In: *Science* 306.5696 (2004), pp. 666–669.

[316] KS Novoselov et al. "Two-dimensional gas of massless Dirac fermions in graphene". In: *nature* 438.7065 (2005), pp. 197–200.

[317] Yuanbo Zhang et al. "Experimental observation of the quantum Hall effect and Berry's phase in graphene". In: *Nature* 438.7065 (2005), pp. 201–204.

[318] Phaedon Avouris, Zhihong Chen, and Vasili Perebeinos. "Carbon-based electronics". In: *Nature nanotechnology* 2.10 (2007), pp. 605–615.

[319] Andre K Geim and Konstantin S Novoselov. "The rise of graphene". In: *Nature materials* 6.3 (2007), pp. 183–191.

[320] RR Nair et al. "Fine structure constant defines visual transparency of graphene". In: *Science* 320.5881 (2008), pp. 1308–1308.

[321] Feng Wang et al. "Gate-variable optical transitions in graphene". In: *Science* 320.5873 (2008), pp. 206–209.

[322] ZQ Li et al. "Dirac charge dynamics in graphene by infrared spectroscopy". In: *Nature Physics* 4.7 (2008), pp. 532–535.

[323] S Marchini, S Günther, and J Wintterlin. "Scanning tunneling microscopy of graphene on Ru (0001)". In: *Physical Review B* 76.7 (2007), p. 075429.

[324] Elena Loginova et al. "Evidence for graphene growth by C cluster attachment". In: *New Journal of Physics* 10.9 (2008), p. 093026.

[325] Peter W Sutter, Jan-Ingo Flege, and Eli A Sutter. "Epitaxial graphene on ruthenium". In: *Nature materials* 7.5 (2008), pp. 406–411.

[326] Qingkai Yu et al. "Graphene segregated on Ni surfaces and transferred to insulators". In: *Applied Physics Letters* 93.11 (2008), pp. 113103–113103.

[327] Alfonso Reina et al. "Large area, few-layer graphene films on arbitrary substrates by chemical vapor deposition". In: *Nano letters* 9.1 (2008), pp. 30–35.

[328] Keun Soo Kim et al. "Large-scale pattern growth of graphene films for stretchable transparent electrodes". In: *Nature* 457.7230 (2009), pp. 706–710.

[329] Xuesong Li et al. "Large-area synthesis of high-quality and uniform graphene films on copper foils". In: *Science* 324.5932 (2009), pp. 1312–1314.

[330] Richard Soref and J Larenzo. "All-silicon active and passive guided-wave components for λ= 1.3 and 1.6 μm". In: *Quantum Electronics, IEEE Journal of* 22.6 (1986), pp. 873–879.

[331] RICHARDA Soref and BRIANR Bennett. "Electrooptical effects in silicon". In: *Quantum Electronics, IEEE Journal of* 23.1 (1987), pp. 123–129.

[332] CA Barrios and M Lipson. "Modeling and analysis of high-speed electro-optic modulation in high confinement silicon waveguides using metal-oxide-semiconductor configuration". In: *Journal of applied physics* 96.11 (2004), pp. 6008–6015.

[333] Ansheng Liu et al. "A high-speed silicon optical modulator based on a metal–oxide–semiconductor capacitor". In: *Nature* 427.6975 (2004), pp. 615–618.

[334] Qianfan Xu et al. "Micrometre-scale silicon electro-optic modulator". In: *Nature* 435.7040 (2005), pp. 325–327.

[335] FY Gardes et al. "High-speed modulation of a compact silicon ring resonator based on a reverse-biased pn diode". In: *Optics express* 17.24 (2009), pp. 21986–21991.

[336] Po Dong et al. "Low V¡ sub¿ pp¡/sub¿, ultralow-energy, compact, high-speed silicon electro-optic modulator". In: *Optics express* 17.25 (2009), pp. 22484–22490.

[337] Jong-Bum You et al. "12.5 Gbps optical modulation of silicon racetrack resonator based on carrier-depletion in asymmetric pn diode". In: *Optics Express* 16.22 (2008), pp. 18340–18344.

[338] Michael R Watts et al. "Ultralow power silicon microdisk modulators and switches". In: *Group IV Photonics, 2008 5th IEEE International Conference on*. IEEE. 2008, pp. 4–6.

[339] Vilson R Almeida et al. "All-optical control of light on a silicon chip". In: *Nature* 431.7012 (2004), pp. 1081–1084.

[340] Shun Lien Chuang. *Physics of Optoelectronic Devices (Series in Pure and Applied Optics)*. New York: Wiley, 2009.

[341] J Schmidtchen et al. "Low loss singlemode optical waveguides with large cross-section in silicon-on-insulator". In: *Electronics Letters* 27.16 (1991), pp. 1486–1488.

[342] Richard A Soref, Joachim Schmidtchen, and Klaus Petermann. "Large single-mode rib waveguides in GeSi-Si and Si-on-SiO¡ sub¿ 2¡/sub¿". In: *Quantum Electronics, IEEE Journal of* 27.8 (1991), pp. 1971–1974.

[343] Yu-Hsuan Kuo et al. "Quantum-confined Stark effect in Ge/SiGe quantum wells on Si for optical modulators". In: *Selected Topics in Quantum Electronics, IEEE Journal of* 12.6 (2006), pp. 1503–1513.

[344] B Huard et al. "Transport measurements across a tunable potential barrier in graphene". In: *Physical review letters* 98.23 (2007), p. 236803.

[345] JR Williams, L DiCarlo, and CM Marcus. "Quantum Hall effect in a gate-controlled pn junction of graphene". In: *Science* 317.5838 (2007), pp. 638–641.

[346] KS Novoselov et al. "Unconventional quantum Hall effect and Berrys phase of 2π in bilayer graphene". In: *Nature Physics* 2.3 (2006), pp. 177–180.

[347] Francesco Bonaccorso et al. "Graphene photonics and optoelectronics". In: *Nature Photonics* 4.9 (2010), pp. 611–622.

[348] Riichiro Saito, Gene Dresselhaus, Mildred S Dresselhaus, et al. *Physical properties of carbon nanotubes*. Vol. 4. Imperial college press London, 1998.

[349] KI Bolotin et al. "Temperature-dependent transport in suspended graphene". In: *Physical review letters* 101.9 (2008), p. 096802.

Chapter 5

Surface microelectrode EM Ion-trapping for SQIP

5.1 Introduction

In this chapter we describe our efforts in the development of scalable devices for quantum information processing (QIP) based in the manipulation of atomic ions using electromagnetic trapping potentials [383], [371], [396]. Ions as quantum bits (qubits) can be trapped by the use of segmented electrodes [378]. Such electrodes may lie in a flat surface so that microfabrication methods could be used for its scalable production [402] [376] [356] [377] [360] [362] [381]. By doing so, not only we can improve the techniques for ion trapping and manipulation towards the development of quantum information processing but also represents an experimental playground for the study of ion interaction with the trap surface (environment) that acts as a thermal bath through vibrational coupling seen as population changes (motional heating) and dephasing (trap frequency fluctuations). Consequences of understanding the surface-ion interactions might allow for better design trade-offs to provide ion-motion flexibility, low motional heating rates and high trap frequencies. In addition, as will be described later, we are able to study the effects of electronic noise near surfaces, a scientific and technological challenge spanning across many fields of experimental knowledge.

Motional heating is caused by electromagnetic background radiation due to voltage fluctuations in the material close to the trapping region, assumed to be fundamentally excited by the thermal motion of the electrons inside the conductors, i.e. Johnson noise [414]; however, no surface electrode microtrap has been able to report this noise measurement before. It is hindered in experiments by "anomalous" noise sources which are greater and thus perturb measurements with different dynamics. In order to study the causes of this extra noise, and how can reduce it, we measure heating rates. To measure heating rates, an ion needs to be in an initial state for which we know its temperature, thus we cool a trapped ion to its ground state. We allow for its heating by turning off the cooling beams for different waiting times, then probe strength of the motional sideband [402] [368] or the strength of

the ion-fluorescence [410]. Once the heating rates have been measured, selected cleaning methods and surface treatment will be performed on the surface, and measure heating rates to confirm a trend.

We document fabrication details of a new kind of trap, different from conventional designs due to few reasons. First, by defining the electrodes on the supporting dielectric with high aspect ratio trenches, the trap can be thoroughly washed before the electrode material is deposited as thin film coat with two angle-sided evaporations. As a result, the PR has been removed completely and it uses less electrode material (one order of magnitude less) facilitating epitaxy. Also, because the high aspect ratio walls required to reduce stray electric fields form the dielectric were patterned on the supporting substrate, coating with our electrode material provides a similar effect as if the electrodes were purely metallic. Different kinds of metals can be deposited including copper, aluminum, gold, platinum, palladium, etc. Second, as presented in Chapter 1, the surface structure plays an important role and thus we modify the crystalline conformation of it by in-situ annealing and other surface treatments included cleaning methods, growth of protective layers or oxides.

To be able to change the grain size of the metal surface used as an electrode, we use an specific aluminum alloy, which annealed increases its grain size by three orders of magnitude. This way, the coherence length of the interaction between ion and electrode surface is expected to be larger, thus reducing decoherent effects in the system.

In addition, the surface can be modified by growing graphene on top of it, using an slightly modified CVD technique that allows for smooth (reduced surface roughness) metal electrodes. The properties of graphene, such as thermal conductivity and chemical inertness could allow for a novel fabrication method, which can reduce the heating rates when compared to conventional surface ion traps. When grown on Copper traps, apparently negligible surface oxidation hints at protected interaction with the environment. Metals such as platinum and palladium were graphene-coated as well.

The organization of this chapter goes as follows: First, we motivate the readers by describing the fundamentals behind ion-trap quantum computers by condensing the reviews [371] [413]. Second, we focus mainly on the motion dynamics of a trapped ion (nonlinear) and its manipulation for interaction in the quantum regime for information purposes. Third, we review conventional and describe our fabrication methods of surface electrode traps. Before presenting experimental results on heating rate measurements, we give a short review of the trap interconnection electronics and tools installed in the experimental setup for surface characterization and evaluation. Towards our understanding of heating rates, we review internal and motional state manipulation.

Ion-trap Quantum Computing

Trapped ions are currently one of the most advanced approaches towards achieving a quantum computer. The fundamental issues of ion trap quantum computing are described in reference [413]. Manipulation and control of single ions is detailed in reference [387]. Applications of entangled ions are reviewed by [396]. Experimentally, long before its conceptu-

alization for quantum computation applications, four D'Vicenzo criteria were demonstrated with trapped ions: initialization [411], read-out of internal electronic states [393] [405] [352], long coherence times [355] and laser cooled crystals of many ions serving as qubit registers [367] [412] [399] [398]. Then, the ion-trap quantum computer was conceptualized by Cirac and Zoller in 1995 [358] and experimentally implemented by Wineland's group at NIST the same year [391].

Quantum computation can be performed by coupling ions via their collective motional degree of freedom, a two-qubit interaction required to fulfill the DiVicenzo requirements. In the proposal by Cirac and Zoller, the quantum information of one ion is swapped to the common motional degree of freedom of the ion string [358], then an operation conditioned on the motional-state can be carried out on a second ion before the quantum information is swapped back from the motion to the first ion. Reference [371] reviews this idea as other methods to implement multi-qubit gates. Other important achievements are the obtention of two-qubit gates [365] [387], entanglement of four ions [404], decoherence of free space [382] and a simulated nonlinear beam-splitter [388].

5.2 Ion-trap Electrodynamics

Atomic ions can be trapped by designed electromagnetic fields. For studies at low energy, two types of traps are used, the Penning trap, which uses static electric and magnetic fields, the Paul or rf-trap which uses ponderomotive forces generated by inhomogeneous oscillating fields. These traps are discussed in several reviews [363] [364] [361] [407] and a book [369]. Here, we review one kind, particularly useful in our context, the linear Paul trap.

A conventional design for a linear RF Paul trap [399] [379] is shown in Figure 5.1. It is like a quadrupole mass filter with additional static electric potentials at both ends. The trap consists of four parallel linear electrodes, equally separated from the trap axis and from its two nearest neighbors. Two opposite (about the trap axis) electrodes are driven by an RF potential of the form $V_0 cos(\Omega_T t) + U_r$ and the other two "control" electrodes are connected to RF ground (or to a DC Control Potential for stability purposes). This scheme supports a quadrupolar RF field for ponderomotive confinement in the radial directions (rf potential is constant as a function of z(axis)), a potential of the form:

$$\Phi \simeq \frac{(V_0 cos(\Omega_T t) + U_r)}{2}(1 + \frac{x^2 - y^2}{R^2}) \tag{5.1}$$

Additional lateral confinement is provided by applying static potentials U_0 on segmented control electrodes, as shown in the picture inset. This provides a static harmonic well in the z-direction of the form:

$$\Phi_s = \kappa U_0(z^2 - \frac{1}{2}(x^2 + y^2)) = \frac{m}{2q}\omega_z^2(z^2 - \frac{1}{2}(x^2 + y^2)) \tag{5.2}$$

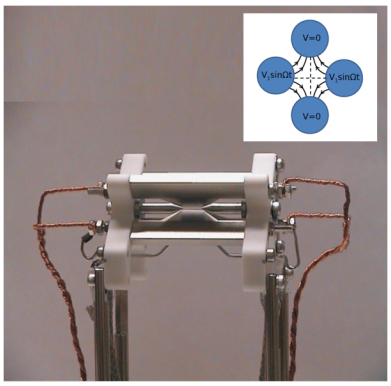

Figure 5.1: *Linear RF Paul trap of standard, four-rod geometry* The potential at the trapping region in the center of the trap is approximated quadratic with a constant curvature. The inset shows the equal-pseudo-potential contours of the trap. Picture taken from reference [361]

where, $\omega_z = \sqrt{(2\kappa q U_0)/m}$. κ is a geometric factor, m and q are the ion mass and charge, and ω_z is the oscillation frequency for a single ion or for the center of mass (COM) of a collection of ions along the z-direction. Equations 5.1 and 5.2 are the lowest order terms in the expansion of potentials for the electrode configuration in Figure 5.1.

When the size of the ion or the amplitude of ion motion is comparable to the spacing between electrodes or spacing between rod segments, higher order terms become important. However, for small oscillations of the COM mode, by using the harmonic approximation, the action of the potentials of 5.1 and 5.2 on the motion along the x- and y- directions can be described by the classical Mathieu Equation (5.3).

$$\begin{aligned} \frac{d^2x}{d\zeta^2} + (a_x + 2q_x\cos(2\zeta))x = 0 \\ \frac{d^2y}{d\zeta^2} + (a_y + 2q_y\cos(2\zeta))y = 0 \end{aligned} \tag{5.3}$$

where,

$$\begin{aligned} \zeta &\equiv \Omega_T t/2 \\ a_x &= \frac{4q}{m\Omega_T^2}\left(\frac{U_r}{R^2} - \frac{\kappa U_0}{z_0^2}\right) \\ a_y &= -\frac{4q}{m\Omega_T^2}\left(\frac{U_r}{R^2} + \frac{\kappa U_0}{z_0^2}\right) \\ q_x &= -q_y = \frac{2qV_0}{\Omega_T^2 m R^2} \end{aligned}$$

The solutions to equation 5.3 are obtained using the Floquet theorem. Typically, $a_i < q_i \ll 1, i \in \{x, y\}$. The solution is given by :

$$u_i(t) = A_i(\cos(\omega_i t + \phi_i)(1 + \frac{q_i}{2}\cos(\Omega_T t) + \frac{q_i^2}{32}\cos(2\Omega_T t)) + \beta_i \frac{q_i}{2}\sin(\omega_i t + \phi_i)\sin(\Omega_T t)) \quad (5.4)$$

where, u is x- or y- direction , A_i depends on initial conditions and $\omega_i = \beta_i \frac{\Omega_T}{2}, \beta_i \simeq \sqrt{a_i + \frac{q_i^2}{2}}$ is the frequency of this "secular" motion (large oscillation amplitude).

In this treatment, micromotion is neglected (terms oscillating at $\Omega_T, \Omega_{2T}, \Omega_{4T}$), understood as superimposed periodic motion with amplitude proportional to the radial secular motion of the ion with respect to the trap center in the radial direction, with smaller amplitude excursions. The ion behaves as if it was confined in a harmonic pseudo-potential Φ_P, or ponderomotive potential of the form:

$$q\Phi_P = \frac{1}{2}m\omega_r^2(x^2 + y^2), \omega_r \simeq \frac{qV_0}{\sqrt{2}\Omega_T m R^2} = \frac{q_x \Omega_T}{2\sqrt{2}} \quad (5.5)$$

where, ω_r is the secular frequency in the radial direction. Ions can then be confined near the z axis of the trap by having $\omega_r \gg \omega_z$, thus forcing the ions to the axis of the trap facilitating individual addressing with laser beams. Spacing between individual ions in this string is governed by a force balance along the z direction due to Φ_s and the mutual Coulomb repulsion of the ions. Implementations of this four-rod design were achieved using macroscopic rods [394][399] and inside edges of slots cut into pairs of alumina wafers [401]. Other designs proposed [406] [392] [351] [370] [374] [353]. All configurations work well but require macroscopic machining and an elaborated assembly, thus large-scale fabrication is not so feasible.

The inset of figure 5.1 displays the equal-pseudo-potential contours of a four-rod linear RF Paul trap. The potential in the center of the trap is approximated as quadratic with constant curvature (independent of the direction in the x-y plane). This pseudo-potential confines ion motion to two dimensions (space coordinates), and its curvature (the second derivative with respect to space coordinates) at this location is the oscillation frequency. The local maximum of the trapping potential forms a saddle equilibrium point, which is predominant at large displacements from the trap center, providing escape trajectories for energetic ions. Therefore after being trapped, ions are immediately cooled so that its energy never exceeds the provided trapping barrier, $\sim 1eV$.

5.3 Surface electrode micro-traps

To incorporate scalable microfabrication methods, the quadrupole electrodes are projected on a single-layer surface. The four-electrode design may be implemented for which a trapping minimum exists above the trap center and between the center two electrodes. Control potentials stabilize the motion of charged particles through the trapping region while maintaining a stable minimum at every point along the trajectory.

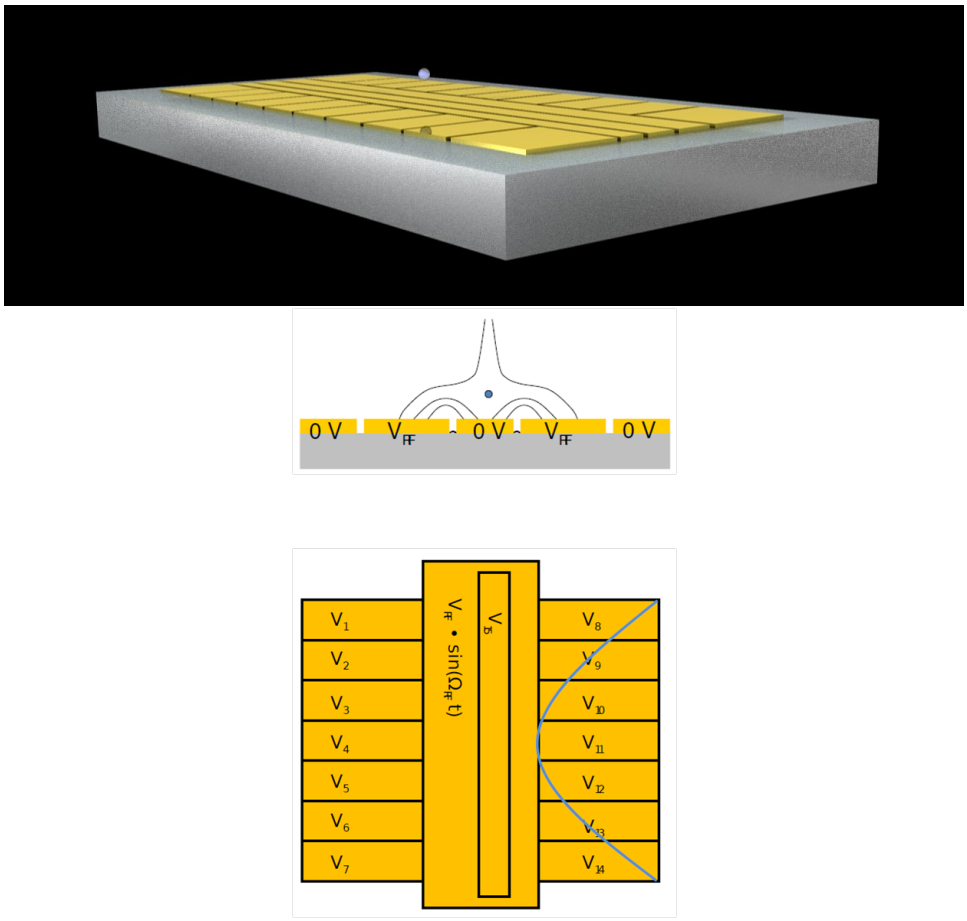

Figure 5.2: *Surface electrode architecture for Ion Trap Quantum Information Processing* RF (time-varying) and DC Static potentials are provided through the use of the central (longitudinal) electrodes and lateral (transverse) electrodes.

Typically, a five-wire configuration is used instead, as shown in Figure 5.2. In this configuration, the center and outer electrodes are at RF ground and the two other electrodes support the RF potential. Mirror symmetry through the plane containing the center electrode and perpendicular to the substrate plane locates the trap axis either above or below the center electrode, leaving the two outer electrodes segmented for longitudinal confinement and control. Ion separation is easier if the center electrode is segmented, however, the induction of control potentials to electrodes without disturbing the trapping RF potential requires of a more complicated connection. Segmentation then is only for the outer control electrode for axial confinement. The five-wire design supports a static potential with two major trap axes, perpendicular and parallel to the substrate (x, y) with the third axis (z) along the longitudinal direction of the wires. The two directions define the major trap axes for the combination of the static potential and RF pseudo-potential.

The distance from the surface to the trapping axis is controlled by scaling electrode size and spacing. The relative lateral sizes of the electrodes rotate the major axes of the trap allowing for laser beam access for Doppler-cooling of ion's motion[375]. Distance between ions can be controlled by adjusting the potential of electrodes near the center of the trapping region. The location and strength of the trapping domain depends on the electrode structure in the lateral direction. Scaling relations numerically obtained by means of pseudopotential calculations were reported in Reference [389] suggesting how geometry affects ion-surface spacing. Recognized tradeoffs for the best trapping performance include ions' motional frequencies drop as the external potential becomes constant. Smaller splitting electrode's size increases the minimum motional frequency during the separation reducing the ion-electrode distance.

The minimum frequency ω_{min} is approximately inversely proportional to the separation from the ions to the nearest control electrode [439]. Effects of surface proximity on ion-heating are reported in [408]. To minimize kinetic excitation of the ions' motional modes, motional heating due to stray fluctuating charges, and to maximize the operation speed of the trap it is intended to increase the minimum frequency as much as it is possible.

5.4 Trap fabrication

Compared to fabrication methods reported in previous Chapters, ion-trap's methods require of extra-careful selection of techniques, tools and chemicals to be used. Residuals left in the surface of the trap could influence vibrational-mode heating of the ions and spoil trap performance during experiments.

The electrode is typically a metal deposited using e-beam evaporation, sputtering, or electroplating processes. Gold is the typical choice due to its relative surface cleanliness. Copper without and with significant surface oxide is also being studied. In-situ surface modification, either by cleaning or dirtying, is performed using O2 or N2 plasmas, UV radiation exposure.

The support of the electrodes must be made of low RF-loss cross-section material with thickness similar to the lateral electrode spacing, ∼few μm to allow for optical access. Smooth surfaces and good adhesive properties to metal films. Fused silica and quartz have low RF loss and its etching is possible using conventional methods. Materials such as aluminum nitride, sapphire, alumina, and diamond, are also useful, however, etching of the latter three is slow. We refer to [389] for a wider review on typical substrate and electrode materials for surface electrode trap fabrication.

Interfaces formed between dielectrics and metal electrodes hold charge which perturb the trapping field. To reduce this effect, trenches undercutting the metal electrodes can be etched into the substrate more than a few times the width of the space between the electrodes, or by electroplating the electrodes to a height few times larger than the inter-electrode spacing.

Our trap fabrication

In our traps we adopted design considerations to reduce ion's motion perturbations. As pictured in Figure 5.3 we keep the dielectric substrate far from the electrode surface, thus reducing noise due to electron accumulation. We achieve this by high-aspect-ratio trench etching of the electrode structure into the substrate. This provides of depth to the created trapping well improving ion's stability, thus longer interaction times (ion lifetimes).

The dielectric substrate is previously patterned with the electrode structure in order to support the metallic electrode as a thin film. Since only a thin film of the material is used to coat the electrode surface and walls (of trenches separating two electrodes). This modification reduces the amount of conductive material used, reducing power consumption and material costs, among the mentioned ion-related benefits.

Quartz is the substrate selected due to its relatively faster etching rate and low cost, compared to Sapphire or Diamond. We use Freon-based chemistry on an inductively coupled plasma reactive ion etching system (ICP RIE)[415] to etch high aspect ratio walls on Silicon, but also possible and dedicated for SiO_2 substrates (marvell nanolab:sts2). Vertical walls, high aspect ratios, good uniformity, and reasonable etching selectivity have been achieved with thick photoresist masking. RIE processes use main etch precursor gasses such as SF6, C4F8 or CHF3 and secondary gases O2, H2, Ar or He to improve stability, etching selectivity or penetration of etching ions.

Although the etching of Silicon, which is very similar has high aspect rations, the plasma etching of quartz has limited depth. Simpler masking schemes and tools for its selective etch are needed. Hard masks, with low sputter yield, such as those provided by aluminium oxide (Al2O3) could be useful to etch SiO2 with very high etch selectivity due to their ability to form non-volatile aluminium fluorides which reduce hard mask thickness [416]. Such a hard mask does not need to be removed, or if so, only to conserve the roughness of the quartz substrate.

Unfortunately, Al2O3-ALD masks for deep etching of SiO2 are still a relatively new process and non-volatile aluminium fluoride residuals created during the etch. Thus, we stabilize an alternate process based on masks made out of conventional thick and hard baked photoresist working for depths down to $\sim 20\mu m$. The process is depicted in Figure 5.3. Starting with a Quartz substrate, standard piranha and RCA clean. Coating of standard thick photoresist (SPR220, $\sim 10\mu m$), hard-baking (120 C, 30min) for improved etch selectivity. An extra PR hardening step using low-Power SF6 plasma makes the outer surface of the PR teflon-like, tougher to physical bombardment.

During quartz etch, low powers are used due to the heat accumulated by quartz, which locally burns the Photoresist, making its removal almost impossible. Higher etching powers (less etching time) were possible by bonding [417] a "carrier" 6 inch Si wafer, which serves as a heat sink. Reduced effects of PR burning were observed, however the complexity added by introducing the bonding step increased our fabrication time considerably, compared to time-segmented low power etching with long waiting times (cooling steps) in between etching steps.

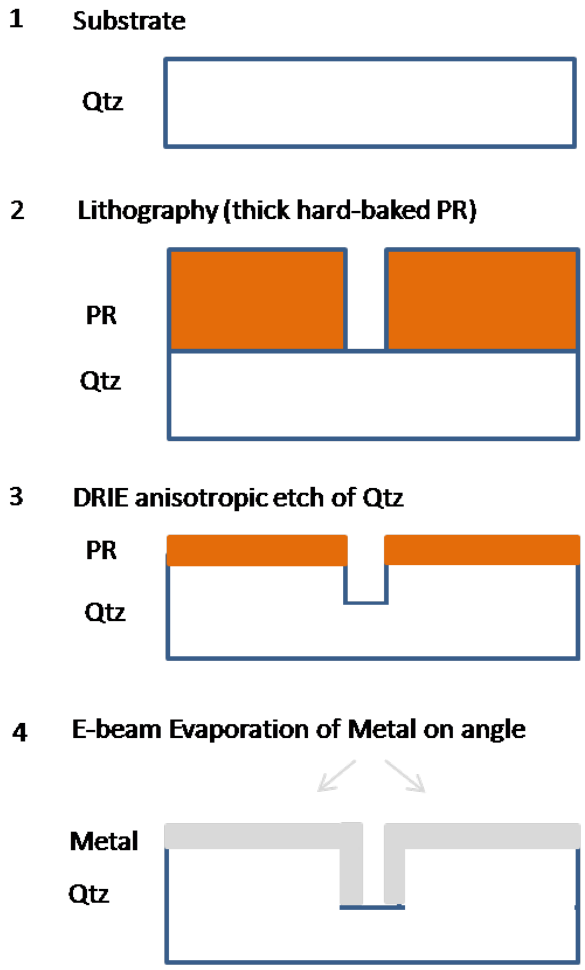

Figure 5.3: *Fabrication steps of our surface electrode traps.* Quartz substrate is DRIE for High aspect ratio patterns, which delimit the domain of our electrodes. Electrode material is e-beam deposited on an angle (to avoid shortcut between electrodes). Deposition on an angle; A. Shortcut at the bottom, B.No shortcut

Trench depths $\sim$ 20um can be obtained by using CF_4 based ICP DRIE. Other plasma etching techniques such as parallel plate plasma etching (nanolab: ptherm) was tested as well, however, although the ecthing rates were faster, the substrate and walls were considerably rougher than the ICP DRIE technique. Once the pattern has been transferred, we remove photoresist residues by cleaning the wafer thoroughly with piranha again. Here, we ensure no contaminants remain on the surface, not even burned photoresist. Since PR outgasses at relatively low temperatures and we suspect that local Temperatures might increase due to RF heating, baking or other processes, making it possible source for additional ion motion perturbation.

Our thin film metal electrode is deposited using conventional e-beam deposition at pres-

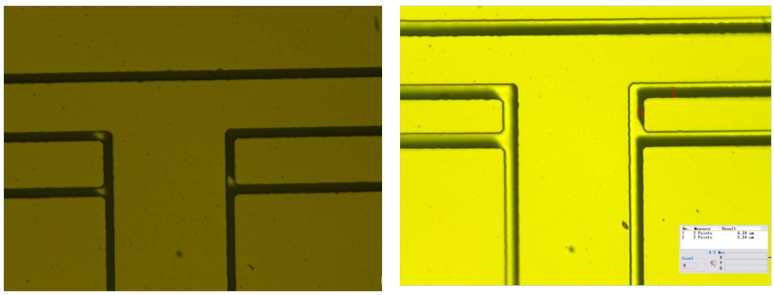

Figure 5.4: *Electrode material is e-beam deposited on an angle.* Shortcut at the bottom of the trench is recognized at whatever corner in the electrode paths of the device under an optical microscope. This is to avoid shortcut between neighboring electrodes). A. Good trap: Does not have a Shortcut, B. Bad trap: Does have a shortcut

sures $\sim 1 - 3 \times 10^{-6}$ Torr. The deposition occurs on an angle, so that only the top surface and trench walls are coated, taking care that the bottom is left clean so that the electrodes separated by the trench do not shortcut at each other. This also ensures that the metal coated wall extends the conductive surface down to the feet of the trench, providing the high aspect ratio needed to reduce stray electric fields from the dielectric. Adhesion of the metal to the dielectric is improved by depositin previously few nanometers of chromium or titanium layers. We have deposited gold, platinum, copper and palladium. Optical images, taken after this step are shown in figure 5.4 to clarify the bad (short-cut) and good (no short-cut) samples after deposition on an angle point. These pictured traps are coated with Gold, approximately 600nm (2 sides x 300nm).

Once the thin film electrode is deposited, we wirebond the trap to a conventional chip carrier with aluminum, gold or palladium wires (higher melting point is best for high Temperature baking procedures, albeit the higher resistivity). Each trap electrode is tested for shortcuts in conventional micro-stage point-probe setups. Lastly, capacitors (noise filters) are mounted in the chip carrier and wirebonded as well (not shown in this figure). Typically, DC electrodes are grouped to save space, reduce trap complexity, allow for other (or less) connections, depending on the experimental use of the trap. After we have prepared the trap, we install it in the experimental setup. Trap preparation (starting from wirebonding) is best done in a particle-free environment, just before installed inside the UHV chamber.

Trap fabrication can be further improved by removing the need of using chemicals and or photoresists. It is still under research removal of residuals left from the use of photoresist on surfaces. We use fused quartz chip and create the electrode pattern with a combination of excimer-laser weakening and HF-etching (done by Translume, Ann Arbor, MI). After etching, the quartz chip is cleaned in Piranha solution at 120°C, and evaporated a metal film combination in an e-beam evaporator with vacuum better than 3×10^{-6} mbar, without allowing the aluminum surface to oxidize in air. We mounted the trap on a chip carrier and baked it in the vacuum system at 160°C for three weeks, to achieve vacuum better than 10^{-10} mbar.

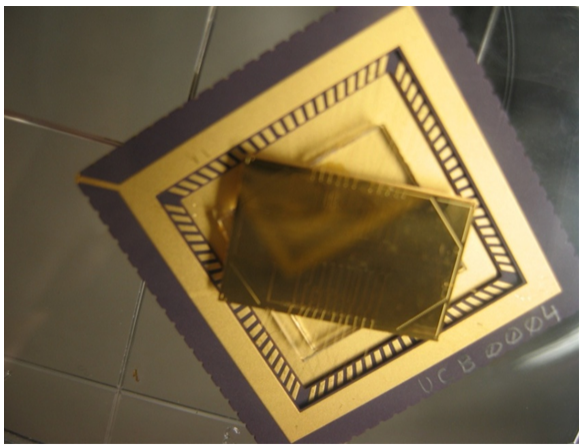

Figure 5.5: *A Surface electrode gold trap* Ready to be placed inside the chamber for its characterization.

We have documented the most conventional trap we are using for measurements in the Lab. The use of standard fabrication methods indicates that scalability of this kind of trap is possible. Improved if high aspect ratios could be easier to achieve. Our trap's most important advantage relies in its surface modification or simply, the re-use of substrate, useful for additional surface trap configurations as the quartz is cleaned and the pattern electrode definition remains untouched.

5.5 Surface structural modification

Aluminum Alloy Trap

As introduced in 1, additional changes in the surface structure would allow us to understand ion-electrode interaction depending on surface properties of the trap. It seems possible to improve the interaction quality between the trapped ion and the electrode surface by having the surface behave as a large grain of unique (or less diverse) crystalline orientations than as a collection of smaller grains of different orientations. In addition, an easier surface characterization results since it is easier to make analytical noise models for single crystal surfaces. As a consequence of such modification, we expect to observe different coherent lengths than those provided by typical metal electrodes (grain size is $\sim$ the thin-film thickness).

Based on references [423][424] we evaporate a trap surface made out of sandwiched Alluminum and Copper films (of 15 nm Ti, 500 nm Al, 10 nm Cu, 15 nm Ti, 500 nm Al, 20 nm Cu,) to form Aluminum-Copper alloy (w. 0.04 Cu). If kept under annealing temperatures below the solubility limit (to reduce surface roughness), the annealed surface form secondary grains of sizes 3 orders of magnitude larger than those of non-annealed Aluminum-Copper alloy or other metallic thin films of the same thickness. In order to perform the annealing

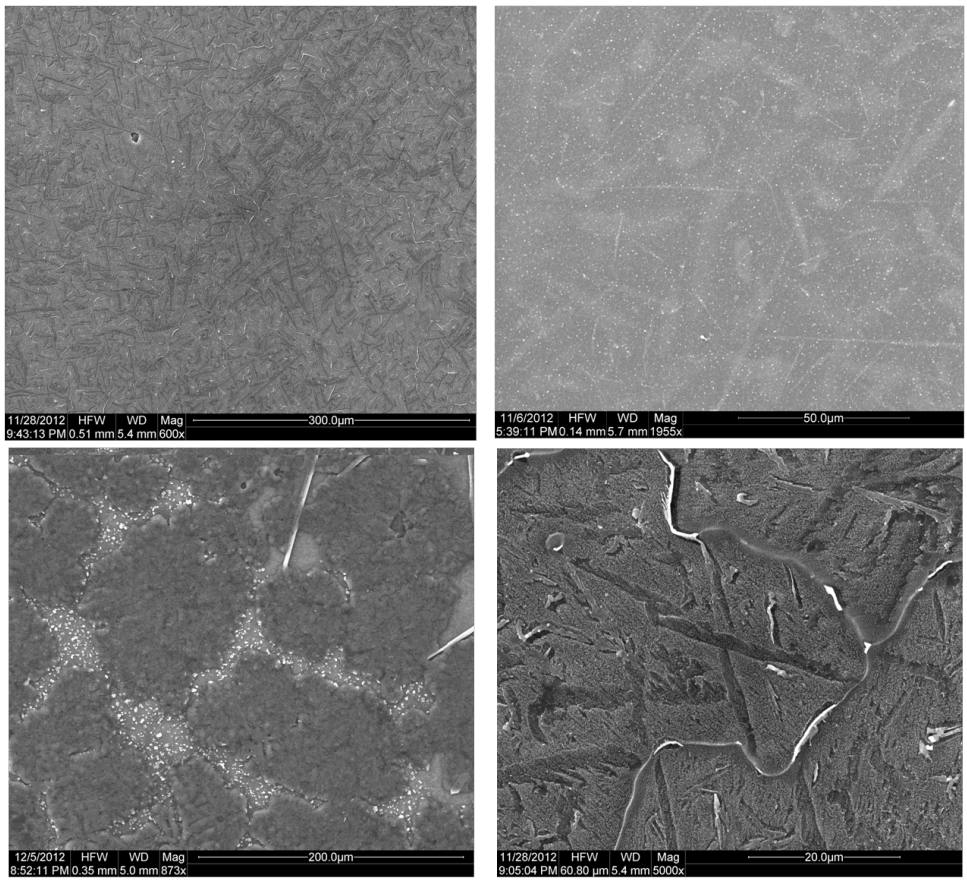

Figure 5.6: *Grain boundaries exposed* Keller's reagent was used to etch the top-most layer of the alloy, exposing the grains. This reagent etches faster along the grain boundaries, an easy way to stabilize the process and confirm the expected grain size has increased.

under controlled environment, we attach to the trap, a heater made out of Palladium. this way, trapping can be performed before and after any structural change on its initial surface characteristics, measured by surface science analytical tools installed.

Finally, since this trap has initially separated layers (Cu - Al) before annealing and ion interaction occurs mostly with the surface, we assume (and experimentally corroborate by AES in the last section of this chapter) that the trap is a Cu trap first, then an Alluminum alloy after annealed. Due to this, we have two traps we are able to measure, from which, the Cu trap is able we get reduced ion heating rates.

To make sure grains are formed, we look for grain boundaries to account for annealing completion. However, under optical microscope, SEM or AFM, grain domains do not appear as obvious. This is due to the fact that all grain activity is submerged under a finer, sand-like surface inhibiting us from observation. Techniques such as X-ray diffraction (XRD) would provide from the needed information to characterize the annealed/non-annealed material

differences and give a precise orientation of all grains near the trapping region [425]. However, its use is elaborated due to tool complexity and safety issues. A one-time measurement is enough for what we want it for, however, for the purpose of process stabilization we use Keller's reagent etchant solution to expose grains in an easier way. The etchant has a faster etching rate at the grain boundaries, thus allowing to quantitatively determine whether the alloy has a characteristic change in grain size after being annealed. Figure 5.6 shows the same sample (before and after annealing) exposing its grain boundaries, invisible before the etchant solution.

Figure 5.7shows an SEM picture of the mounted and annealed trap once the top surface has been removed).As can bee seen near the electrode of the heater, aluminum alloy grains have precipitated from the trap due to an accidental increment in the Temperature, liquifying the surface, evacuating through the wires of the heater. The characteristic (100) face of aluminum is recognized in a 50 μm sized grain. Confirmed by using X-ray diffraction technique (not included here). SEM allows for an extraordinary easy way to check for trap shortcuts. Figures 5.7 and 5.8 show SEM pictures of an Al-Cu trap. As can be appreciated, image contrast is lost once the electrodes are shortcut. In figure 5.8 the shortcut is provided with a wire for the last electrode.

Graphene-surface Trap

Surface mechanisms limit trapping lifetime, thus reducing the number of operations possible under same conditions. Periodic cleaning alleviates these effects at the cost of additional complexity in carried processes and installed systems. New configurations for the trap to reduce surface contamination are still under active research. Materials with surface properties capable of slightly modifying the trapping potential are of use in order to tailor surface properties for the best trapping performance.

Graphene, as an electrode material would enable for such a configuration due to its fascinating properties satisfying most trap design requirements. Graphene is attractive not only due to extremely high electrical and thermal conductive properties, but because graphene possesses a chemically inert surface, thus contaminants would be less prone to be adsorbed by it. Since Graphene can be grown in any low RF-loss material substrate, Quartz substrates can be selected as well, thus the series of steps are alike. Quartz (SiO2) can be etched with high etching selectivity using inductively coupled plasma, as mentioned before. In order to reduce additional contaminants, graphene is CVD-grown on thin or thick layers of metal deposited at an angle using the recipe reported by reference [426]. The metal might be removed or not by using the proper etchant.

We characterize the quality and the number of layers of graphene as in the previous chapter. Reference [99] describes the differences between the 514 nm Raman spectra of graphene and bulk graphite. The two most distinctive features are the G peak at $1580cm^{-1}$ and the Gprime band at $2700cm^{-1}$, present in graphite samples. In defected graphite, phonons give rise to a peak at $1350cm^{-1}$ known as the D peak. The Gprime peak is also known as the 2D peak as well. Absence of defects understood when no D peak is observed (D

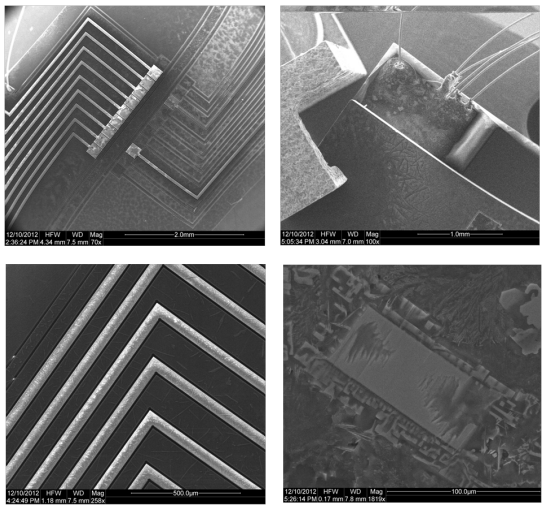

Figure 5.7: *SEM pictures of Aluminum alloy trap* A,B.) trap details C.) Trap as is mounted on the heater with wirebonds. D.) Aluminum single crystal (100) orientation [440] and XRD-confirmed.

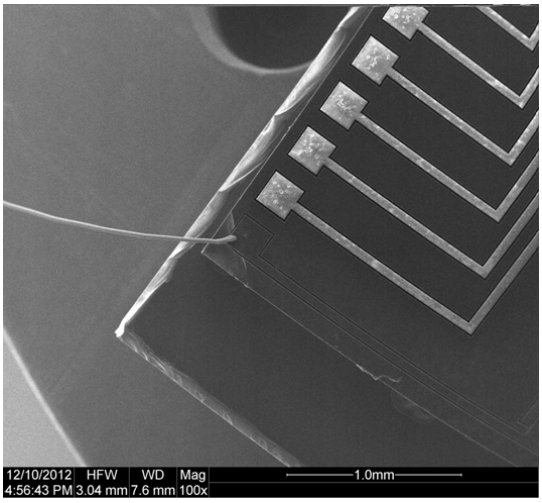

Figure 5.8: *SEM picture of our Alluminum alloy trap.* SEM imaging allows us for a quick way to check for shortcuts, definitely easier than with probes, but less informative since we need to check for shorts between DC electrodes. Also, the measurement of electrode resistance is important when designing the proper filters for each electrode

peak is only observed at the edges of the sample). Figure 5.9 shows the significant changes in shape and intensity of the 2D peak of graphene between surfaces containing graphene and no-graphene.

However, CVD grown Graphene needs of extra careful characterization since the number of layers cannot be extracted from contrast between Raman peaks [99] [426]. From reference

[426] CVD-grown graphene Raman spectrum exhibits lack of long order along the c direction contrary to highly ordered structure of graphite seen in the Raman spectrum for exfoliated HOPG layers. Lorentzian fitting on the shape of the 2D band allow to differentiate single-layers, bilayers and trilayers of graphene in the HOPG samples, where Monolayer graphene has a single and sharp Lorenztian peak. However, for CVD grown graphene on SiC and metal surfaces, monolayer, bilayer and trilayer of graphene exhibit a single and sharp Lorentzian-shaped peak. Due to this, the 2D peak line shape is not enough to identify the number of layers in CVD grown graphene. Combination of AFM and Raman spectroscopy to show that the IG/I2D ratio provides a good estimation of the number of layers is used instead. We determined that our samples consist of 1-3 graphene layers. In order to mask the growth in a graphene CVD furnace we used stainless steel clamps, so that we have areas with and without graphene. Due to the high temperatures (1100 C) and the furnace spatial limitations, only high-melting point materials can be used to mask graphene growth.

Graphene can be grown in ebeam-evaporated copper and platinum surfaces after annealing have reconfigured the polycrystalline orientation of mentioned surfaces into a (111) face. Graphene is grown using the recipe for copper film growth or sputtered platinum [427]. This solution is less expensive due to target costs for sputtering tools. Two traps were fabricated using these substrates. In figure 5.10 we show a quartz/graphene trap. After removing all copper from the surface, left with only a dark (absorbing) graphene layer on the substrate. Figure 5.9 shows an AFM picture of the surface. The step observed step is 2.684 nm thick. The raman signals from the two regions is noticeable different in its surface roughness. Both places contain graphene of different quality.

After graphene was grown, a number of defects were recognized as possible experimental drawbacks. First, all carbon atoms that are not conforming the graphene layer, but are still on the surface might perturb loading rates and trapping life due to collisions. Also, due to the high Temperatures required for the growth, sufficient material was evacuated from the the metallic surface so that surface roughness has increased considerably. Over-pressurizing the CVD chamber could allow for less metal evacuation and thus not degrade the quality of the surface, however characterization of such growth is required. Even when you could remove these two factors, the cleanning methods which are used and seem to work would need to completely damage the surface of this trap.

5.6 Trap interfacing

As required, the trap is connected to external electronic equipment and controlling systems through extra careful coupling of electronic systems maximizing signal integrity protection. A noise spectrometer is used to measure how noisy signals propagate and affect the multiple electronic systems in the environment. Ultimately located inside a Faraday cage, our trap is to be completely isolated from its environment and interfaced physically only through DC and RF wires. A wide array of robust quantum optics tools allow for the controlled preparation of an ion's initial state, its manipulation and a high fidelity readout of the final

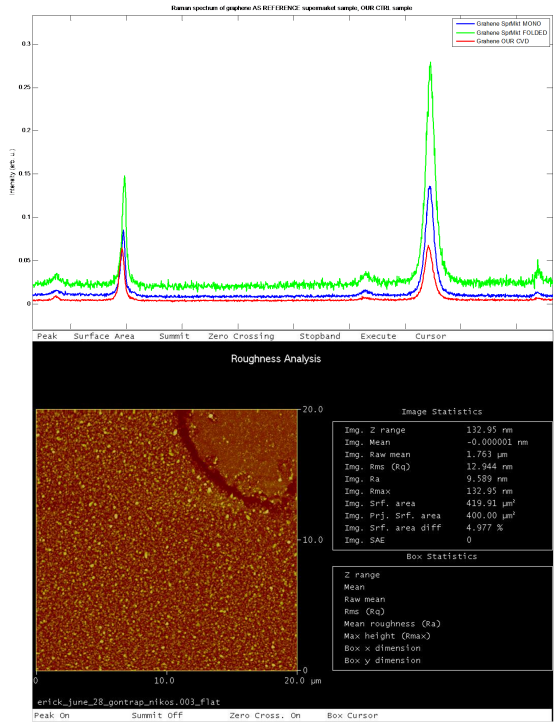

Figure 5.9: *Raman and AFM characterization of our graphene-based surface electrode ion trap* As expected and presented, the G and 2D peaks are characteristic Raman fingerprint of graphite materials, AFM thickness measurement and characterization.

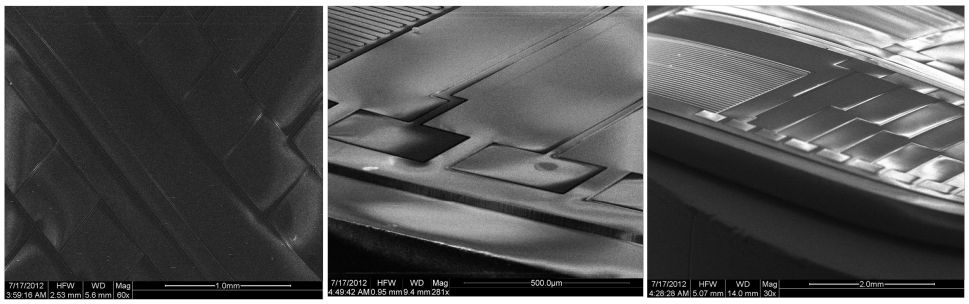

Figure 5.10: *Graphene on Quartz trap.* After removal of the Copper underneath, a sheet of graphene stays on the substrate. The characteristic absorption and Raman peaks indicate Graphene signature.

state.

The interconnection occurs depending on the source of the signal and its frequency of oscillation (RF or DC). The DC voltages are generated by low-noise digital-to-analog converters (AD660), passing through a sixth-order low-pass filter with insertion loss at frequencies above 200 kHz. The last filtering stage resides inside vacuum, and consists of 47μF

(X7R dielectric) capacitors on the printed circuit board which supports the chip carrier with the trap, as well as 0.6 nf (X7S dielectric) capacitors, which are wire-bonded on the chip carrier. The experiment control and counted readout of the detector is done with a field programmable gate array (FPGA). The entire vacuum system, including the electronics for the radio-frequency and static trapping potentials resides inside a Faraday cage providing more than 40 dB of attenuation for electromagnetic fields in the range of frequencies between 200 kHz and 1 MHz, at which we have performed trap noise measurements. Filters allow for the reduction of noise on bands that are of our interest. Matching of system's impedances is necessary to improve coupling requirements. Ground loops are possible and its elimination is very important in the reduction of noise in the system. Distinguishing the characteristic noise in the wiring is needed (channels pervaded by 60Hz noise, MHz noise, etc) since it helps understand the noise in the wiring and keep noisy channels away from clean channels, for the power line. Figure 5.11 shows the sphere setup. The ion trap is mounted on a rotatable manipulator as depicted in the figure 5.11b. When the trap is facing the positive y direction, the trap surface faces a retractable-reentrant viewport with a large NA ($\sim$0.3) objective for ion fluorescence collection, and the chamber operates as an ion trapping chamber. When the detection viewport is retracted, the Ar+beam from the ion gun is incident at 45o with respect to the y axis. The trap can be rotated by any angle around the z axis to adjust the angle of incidence of the Ar+ions on the trap surface. When the trap chip is rotated to face in the negative y direction, it faces the Auger/LEED unit, which allows to characterize the elemental composition of the trap surface. A residual gas analyzer (RGA) with its axis at 45 degrees with respect to y on the yz plane is also present.

5.7 Trapping Experiments

A resistive oven is used to produce a beam of neutral calcium atoms and it is aimed so that the beam propagates parallel to the surface, along the axis of the trap. The neutral calcium atoms are photo-ionized with a two-photon process using 375nm and 422nm tuned lasers from the ground state to the continuum (Ionization limit of 6.1130 eV)

The experiment is conducted by first loading a 40Ca+ ion in the segmented surface trap using two-stage photo-ionization at 422 nm and 375 nm. The radial trap frequencies are approximately 2.2 MHz and 3 MHz and the axial trap frequencies between 200 kHz and 980 kHz. To allow for simpler dynamics, each system needs to be tuned to its cleanest state for interaction, i.e. at its highest Q possible. This can be experimentally achieved using a resonator interfaced to the RF-signal. Trapping frequencies $\sim \frac{\Omega_T}{2\pi}$ are amplified to $\sim$1-2 W and sent to a helical resonator in a quarter-wave configuration to step up the amplitude to $\sim$100 V. This is fed to the RF electrodes of the trap, with capacitance at the RF feed-through of $\sim$ 20-30 pF.

To control the electronic and motional states of the ion we require of high frequency and intensity stability of the light mode used, which we achieve using acousto-optical modulators. The lasers are referenced to an ultra-stable cavity and a PID controller is used to tune the

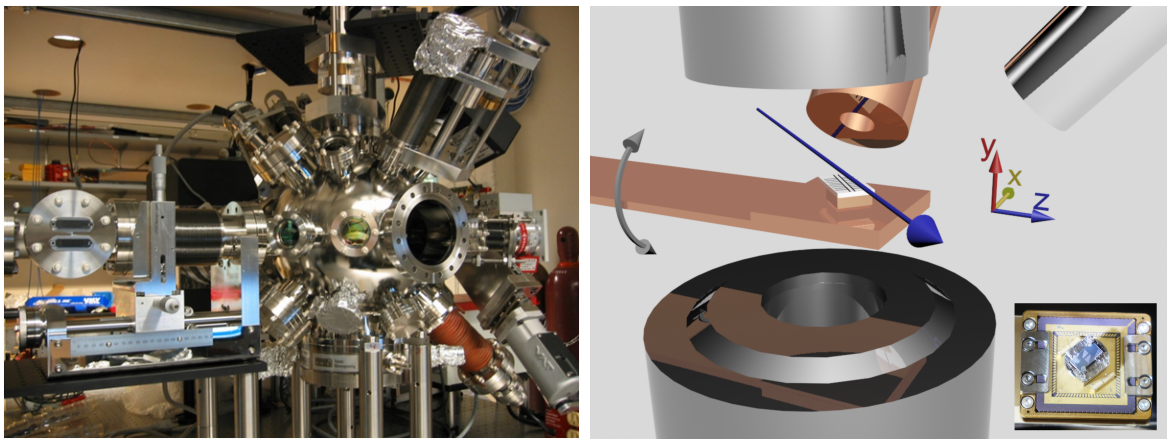

Figure 5.11: *The sphere* A chamber equipped with most of the useful surface science tools for the study of the surface of our traps. The chamber integrates a surface trap (center) attached to the filter board on a 180 degree rotational holder, an Auger spectrometer (bottom), a Ar+ gun (Hensinger Scientiffic IS-40C-PC, behind, xy plane, copper), an observation channel (above), a 300 l/s ion pump (Star Cell, not shown) and a residual gas analyzer (upper right). The laser direction indicated by the blue arrow has a 7=degree tilt along the axial direction of the trap. A picture of the mounted Al-Cu trap is shown in the lower right corner.

cavity length for the required ultra-narrow linewidth. Reference [390] provides a good review of the setup with excellent figures, from which we borrow 5.12, 5.13, and 5.14 detailing the RF helical resonator, optical setup in another UHV chamber called "the octagon". Also pictured, the PID control of lasers using the Pound-Drever Hall method [441].

DC control electrodes need of RF grounding capacitors and other filters. These are typically installed on a separate board called "filter board", which is under constant calibration and adjustment. With these components, control electrode voltages can be changed such that ions can be transported in segmented traps. Routines of its transport an other important pulse sequences are controlled through the use of FPGAs and a Graphic User Interface running python-supported experimental software for the easy management of operations, calculations, plot display, etc. Only by doing so, the experiments get more complicated as we perform previous ones with the click of a button. Since time is a big factor in these experiments, saving time must be practiced.

Internal and Motional Quantum State Manipulation

Motional Quantum State

An ion trapped in a ponderomotive potential (Equation 5.5) can be seen as an ordinary time independent harmonic oscillator with modifications for laser-cooling [380](J. I. Cirac, 1994). In the quantum domain, micromotion may be understood as a breathing motion mode (at the

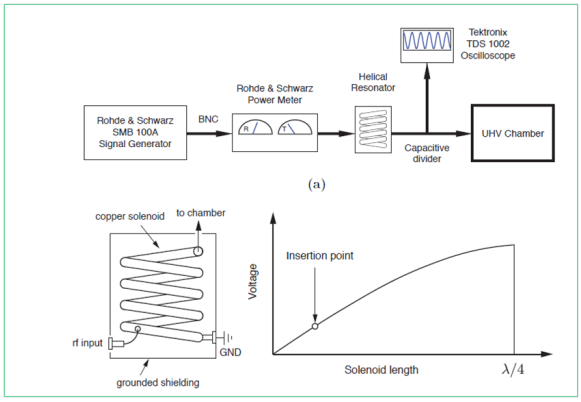

Figure 5.12: *RF signal Setup.* A helical resonator is used to amplify the RF signal and improving its Q. Picture taken from [390].

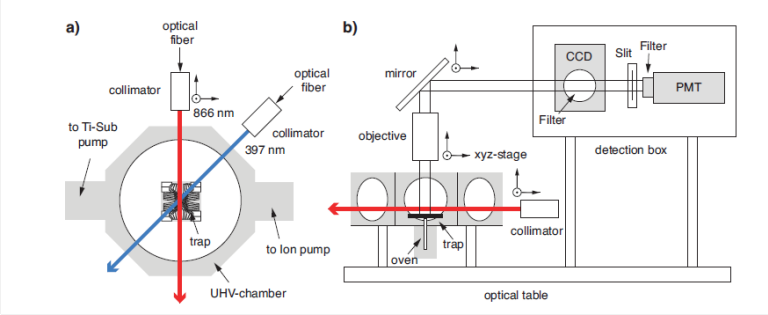

Figure 5.13: *Optical Setup* Laser access to the chamber is possible through the glass view mirrors. Optical fibers are aligned just outside the chamber mounted on a suspended optical breadboard. Lasers are for Cooling, Detection, Re-pumping and Qubit operations. Picture taken from [390].

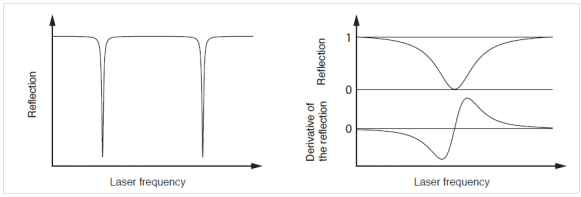

Figure 5.14: *Lasers are Intensity stabilized by using the Pound-Hall method.* A PID controller is used to tune the cavity for a high Q. Picture taken from [390].

drive frequency Ω_T) separated spectrally from the secular motion of the ion's wavefunction (at frequencies ω_x) and ω_y) in Eq. 5.5. We will consider only resonant interaction at secular frequencies (average over motion components at drive frequency Ω_T)). Thus, the pseudo-potential secular motion can be approximated as an oscillator in a static potential.

Motion of a single ion, or a normal mode of its collective motion, is described by the

Hamiltonian 5.6:

$$H_{osc} = \hbar\omega_\imath \hat{n}_\imath \tag{5.6}$$

where, $\imath \in x, y, z$, $\hat{n}_\imath = a_\imath^\dagger a_\imath$ and $a^\dagger$ and $a_\imath$ are the harmonic oscillator raising and lowering operators, respectively. The operator for the COM motion in the z-direction is given by $z = z_0(a + a^\dagger)$, with: $z_0 = \sqrt{\hbar/2m\omega_z}$ as the spread of the zero-point wavefunction. That is, $z_0 = \sqrt{\langle 0|z^2|0\rangle}$, where $|n\rangle$ is the nth eigenstate (Fock state) of the Harmonic oscillator. Pure states of motion can then be written as in Equation 5.7:

$$\Psi_{motion} = \sum_{n=0}^{\infty} C_n e^{-n\omega_\imath t}|n\rangle \tag{5.7}$$

Internal Quantum State

To describe the interaction with two internal levels of an ion, we ensure internal states are non-degenerate and use resonant excitations to couple only to two levels at a time. It is a practice, to use the two-level representation of the analogous spin 1/2 magnetic moment in static magnetic field as equivalent representation [397] [418]. In this equivalent representation, a "fictitious" magnetic moment $\mu = \mu_M S$, where S is the spin operator (S=1/2), is placed in a "fictitious" magnetic field $B = B_0\hat{z}$. The Hamiltonian can be written as 5.8:

$$H_{internal} = \hbar\omega_0 S_z \tag{5.8}$$

Here, S_z is the operator for the z component of the spin and $\omega_0 \equiv -\mu_M B_0/\hbar$. Typically, internal resonant frequencies are much larger than any motional mode ($\omega_0 \gg \omega_z$).

We label internal eigenstates as $|M_z\rangle = |\uparrow\rangle$ and $|\downarrow\rangle$ representing "spin-up" and "spin-down" respectively, and for convenience, will assume $\mu_M < 0$ so that the energy of the $|\uparrow\rangle$ state is higher than the $|\downarrow\rangle$ state. A general pure state of the two-level system is then given by

$$\Psi_{internal} = c_\downarrow e^{i\frac{\omega_0 t}{2}}|\downarrow\rangle + c_\uparrow e^{-i\frac{\omega_0 t}{2}}|\uparrow\rangle \tag{5.9}$$

where, $|c_\downarrow|^2 + |c_\downarrow|^2 = 1$. In our case, the two-level system is that of the ground state and a single (for our purposes) excited state of an atomic ion.

The basic Hamiltonian

The basic Hamiltonian of two-level systems interacting with a quantized harmonic oscillator via laser light is pictured in Figure 5.15. Detailed discussion is found in references [413] [387].

The Hamiltonian for a trapped single ion interacting with near resonant laser light (taking into account that only two levels of the ion and one vibrational mode (oriented along the

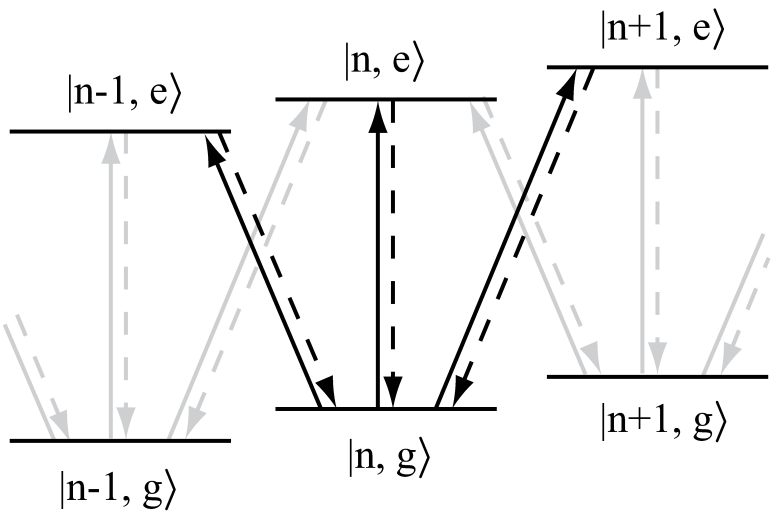

Figure 5.15: *Energy Level Scheme of single trapped ion in harmonic trap* Carrier and Sideband transitions.

z direction)) under the Lamb-Dicke approximation (valid for cold tightly bound ion strings $\eta\sqrt{\langle(a+a^\dagger)^2\rangle} \ll 1$) is described by equation 5.10:

$$H = \hbar\Omega\{\sigma_+ e^{-i(\Delta t-\varphi)} + \sigma_- e^{i(\Delta t-\varphi)} + i\eta(\sigma_+ e^{-i(\Delta t-\varphi)} - \sigma_- e^{i(\Delta t-\varphi)})(ae^{-i(\omega_i t)} + a^\dagger e^{i(\omega_i t)})\} \quad (5.10)$$

Three laser detuning Δ cases are of particular interest (see Figure 2.15): $\Delta = 0$and $\Delta = \pm\omega_t$ provided the second rotating wave approximation (RWA) applies (only one transition is relevant at a time).

In the Hamiltonian describing the carrier transition ($\Delta = 0$), only the electronic states of the ion are changed. In the Hamiltonian describing the blue sideband transition $\Delta = +\omega_t$, a motional quantum is created and excitation of the electronic state of the ion. Within this two-level system, Rabi flopping occurs, with frequency described by equation 5.11:

$$\Omega_{n,n+1} = \sqrt{n+1}\eta\Omega, \Omega_{0,1} = \eta\Omega = \Omega_+ \quad (5.11)$$

where, n describes the number of motional quanta (phonons). The blue sideband Rabi frequency is defined with with 0,1 describing flopping between the $|g,0\rangle$ and the $|e,1\rangle$ state.

In the Hamiltonian describing the red sideband transition $\Delta = -\omega_t$, a phonon is destroyed, and excitation of the electronic state with Rabi flopping at the Rabi frequency 5.12:

$$\Omega_{n,n-1} = \sqrt{n}\eta\Omega \quad (5.12)$$

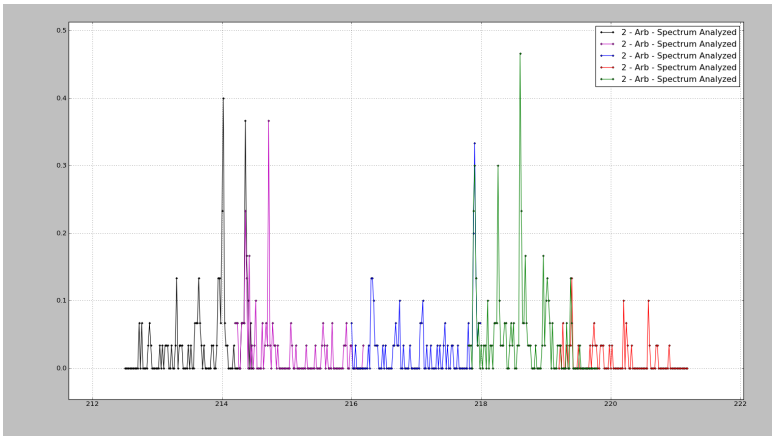

Figure 5.16: *Laser Detuning for Carrier, Blue and Red sideband transitions.* These are experimental spectrum lines obtained during heating rate studies using the 729nm technique. Due to drifts in the system, these lines shift as the experiment is taking place, thus a continuous monitoring is practiced in order to compensate for the effect. Labels are missing but corresponding to the multiple transitions available, described in reference [444]

Driving sideband transitions as fast as possible during quantum operations is desirable, however due to Lamd-Dicke factors, the rotating wave approximation is not satisfied for frequencies $\Omega \sim \omega_t$.

Detection of Internal States

To discriminate between two electronic states with detection efficiencies ~ 1 we use the "electron shelving technique" [442] [393] [405] [352] [395] [359]. This is done by coupling the ground state $|S\rangle$ to the metastable $|D\rangle$ using a weak transition and to the state $|P\rangle$ withan stronger transition. The weak transition is used for coherent manipulations, and the measurement of the occupation of the $|D\rangle$ state is done by driving the strong transition with a laser. No fluorescence is observed if the atom is in the $|D\rangle$ state, while on the $|S\rangle \leftrightarrow |P\rangle$ photons are scattered. By repeatedly preparing the ion state and measuring fluorescence the $|D\rangle$ state occupation can be determined.

The internal state of the ion is indicated by presence or lack of light scattering correlated to ion's internal state. This is accomplished using appropriately polarized laser beams tuned to a transition which scatters or not photons depending on internal states of the atom. Efficiency of this "cycling" transition is studied in [413].

The ion is excited on the $S_{1/2}(m_j = +1/2) \leftrightarrow D_{5/2}(m_j = -3/2)$ transition with a narrow band laser (see Fig. 5.17) and simultaneously the D level is coupled to the $P_{3/2}$ level with a broad band laser at 854 nm. In this way the population of the $S_{1/2}(m_j = +1/2)$ state is effectively coupled to the rapidly decaying $P_{3/2}(m_j = -3/2, -1/2)$ levels while the $S_{1/2}(m_j = +1/2)$ level is not touched.

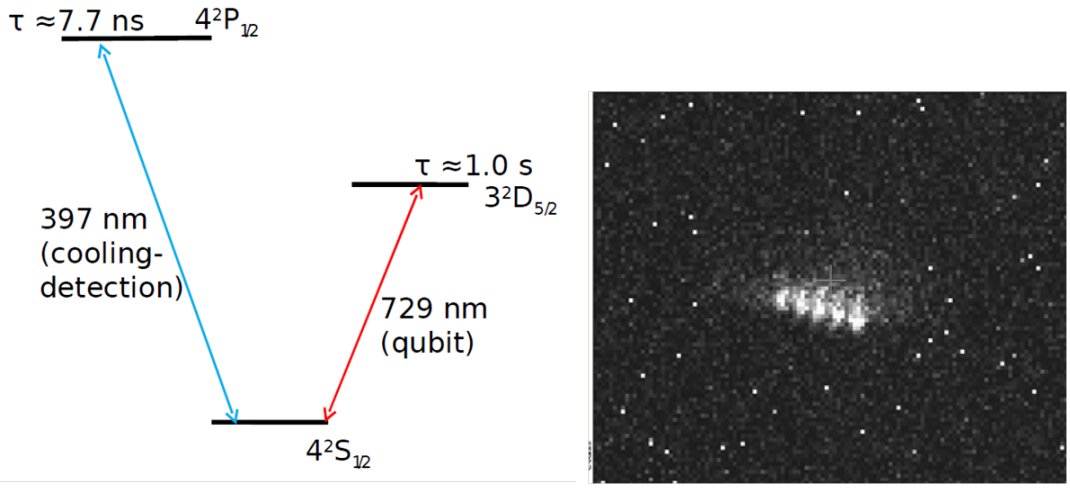

Figure 5.17: *Detection and qubit encoding* Cooling, Detection and S-D manifold (Qubit encoded) Simplified state diagram. Five trapped ions loaded (Screen pictures from our CCD camera interfaced through a GUI experimental control software). One trapped ion is loaded for heating rate studies.

The ion does not fluoresce under irradiation of light on the $S_{1/2} \rightarrow P_{1/2}$ and $D_{3/2} \rightarrow P_{1/2}$ transitions if its valence electron is in the $D_{5/2}$ state. If the electron, however, is in either the $S_{1/2}$, $P_{1/2}$ or $D_{3/2}$ state, the ion will scatter approximately $10^7 - 10^8$ photons/s. A lens system collects typically $10^{-3} - 10^{-2}$ of this fluorescence light such that with a photomultiplier tube (quantum efficiency $\sim 30\%$) about 30 photons/ms can be detected.

In Figure 5.18, Rabi oscillations are pictured. Mathematically, we can describe the effect of resonant radiation inducing such a coupling by a rotation $R^C(\theta, \phi)$ acting on the state vector $\alpha|0\rangle + \beta|1\rangle$ (reference [419]):

$$R^C(\theta,\phi) = exp(i\theta/2(e^{i\phi}\sigma_+ + e^{-i\phi}\sigma_-)) = Icos(\theta/2) + i(\sigma_x cos\phi - \sigma_y \sin\phi)\sin(\theta/2) \quad (5.13)$$

$$R^C(\theta,\phi) = \begin{pmatrix} \cos(\theta/2) & ie^{i\phi}\sin(\theta/2) \\ ie^{-i\phi}\sin(\theta/2) & \cos(\theta/2) \end{pmatrix} \quad (5.14)$$

where, the lowering and raising operators are:

$$\sigma_+ = \begin{pmatrix} 0 & 1 \\ 0 & 0 \end{pmatrix}, \sigma_- = \begin{pmatrix} 0 & 0 \\ 1 & 0 \end{pmatrix} \quad (5.15)$$

And, the Pauli-spin matrices are:

$$\sigma_x = \begin{pmatrix} 0 & 1 \\ 1 & 0 \end{pmatrix}, \sigma_y = \begin{pmatrix} 0 & -i \\ i & 0 \end{pmatrix} \quad (5.16)$$

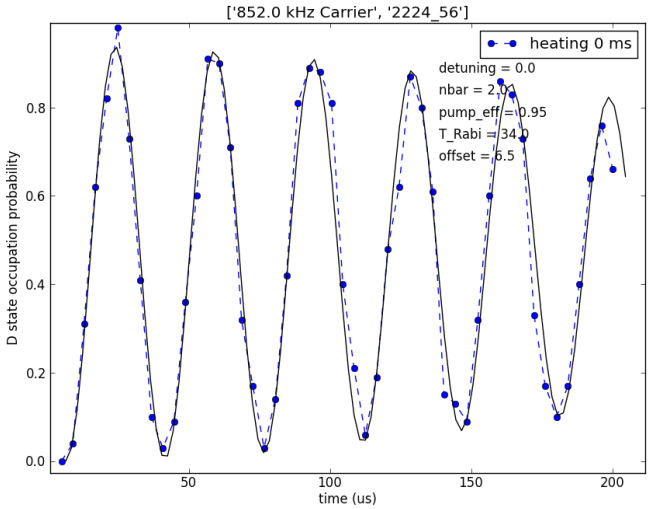

Figure 5.18: *Rabi Oscillations.* Experimental Rabi oscillations. A laser field resonant with the carrier transition of frequency ω_{qubit} drives transitions with Rabi frequency Ω_{eff} where the motional state is not changed. Initial condition to heating rates studies, zero waiting time

Relevant control parameters in the ion trap experiments are the pulse area $\theta = \tau$ (Rabi frequency, pulse length τ) and the phase of the laser field ϕ. These control parameters can be conveniently controlled with an acousto-optical modulator in double-pass configuration [420] by phase and amplitude modulation of the Rf field driving the acousto-optical modulator.

The angles θ and ϕ specify the rotation. The visualization of this evolution is aided by the use of Bloch sphere with logical $|0\rangle$ (energetically higher state) located at the North pole and the $|1\rangle$ (energetically lower state) located at the South pole. In the Bloch picture, the angle ϕ denotes the axis of rotation in the equatorial plane and θ the rotation angle, or pulse area. Any linear combination of σ_x and σ_y operations can be implemented with laser pulses. Rotations around the z axis can be decomposed into rotations around the x and the y axis. All rotations on the qubit can be shifted by $-\Delta\phi$ to achieve a rotation about the z axis by $\Delta\phi$. Far detuned laser beams can shift the relative energy ΔE of the eigenstates (AC-Stark effect) by $\Delta E = \Omega^2/2\Delta$. Thus, after a time $t = \hbar\Delta\phi/\Delta E$ the desired phase shift is acquired.

Detection of Motional States

The motional degrees of freedom of the ions serve as the quantum bus among ions. Manipulation of the motion of single ions is described in reference [387]. A single ion coupled to a single motional mode is studied. If the laser field is detuned by the trap frequency towards higher energies, the blue sideband is excited, carrying the following operation

$$R^{+}(\theta,\phi) = exp(i\theta/2(e^{i\phi}\sigma_{+}a^{\dagger} + e^{-i\phi}\sigma_{-}a)) \tag{5.17}$$

The atomic flip operators, annihilation and creation of a phonon at trapping frequency ω acting on the motional quantum state, where θ is related to the strength and duration of the pulse and ϕ is the relative phase between the optical field and atomic polarization. Here, the electronic and motional degree of freedom change. Similarly, for the opposite detuning the red sideband can be excited.

Figure 5.16 shows a spectrum of a single trapped $^{40}Ca^{+}$ ion near the qubit transition. At a detuning of $\pm 1MHz$, the red and the blue axial sidebands appear, respectively. At a detuning of $\pm 5MHz$, radial sidebands and higher order sidebands are visible. For the applied laser power and excitation time, the carrier transition is strongly saturated while the sidebands are only weakly saturated. This indicates that the sideband transitions are weaker than the carrier transition as it is expected from Eq. 5.11 and 5.12.

5.8 Heating rates

Ion manipulation above the surface of the trap leads to heating of its motional modes [401]. Cooling steps have been implemented to alleviate this effect during transport [413] [383] [400] [354] [350]. An increase in heating rates localized at ion loading regions suggests surface contamination is a possible cause. Smaller traps seem to enhance the sensitivity of the motional modes.

In our measurements noise induced from outside sources may be reduced by shielding and proper grounding. Less noise means greater sensitivity (signal to noise ratio, SNR as a figure of merit). However, there exists a fundamental source of noise which is an intrinsic result of the thermal jitter of the charge carriers and the quantization of charge, known as Johnson noise. Additional heating of the ion's motional modes is provided by a contribution of factors such as the thermal electronic noise from the metallic fluctuating patch potentials, and other unknown sources. These sources have heating rates that scale as some power of the distance between the ion and the electrodes [408] [421]. By testing the scaling of heating rates according to ion proximity to trapping surface, information on the dynamics of dominant sources could be retrieved.

Johnson noise heating cause fluctuations in the field at the ion. Heating rates scale as $\frac{1}{d^3}$ for $d \ll d_S$. For $d \gg d_S$, the heating rate should scale as $1/d^2$ [408] [421] [414]. where d is the distance from ion to electrode and d_S is the skin depth of the electrode metal [421].

Anomalous heating is a source of noise provided by aggregated films or impurity atoms adsorbed on trap electrodes, metal surfaces and amorphous dielectrics. Chapter 1 describes its possible influence on ion motional-state heating. It has been measured having high rates [401] [408] and found 3 orders of magnitude higher than those from Johnson noise considerations [391] [413].

Reference [428] uses the patch potential model [408] to describe the measured scaling of $1/d^4$ if the size of the patches is smaller than d. The electric field noise heating the ion

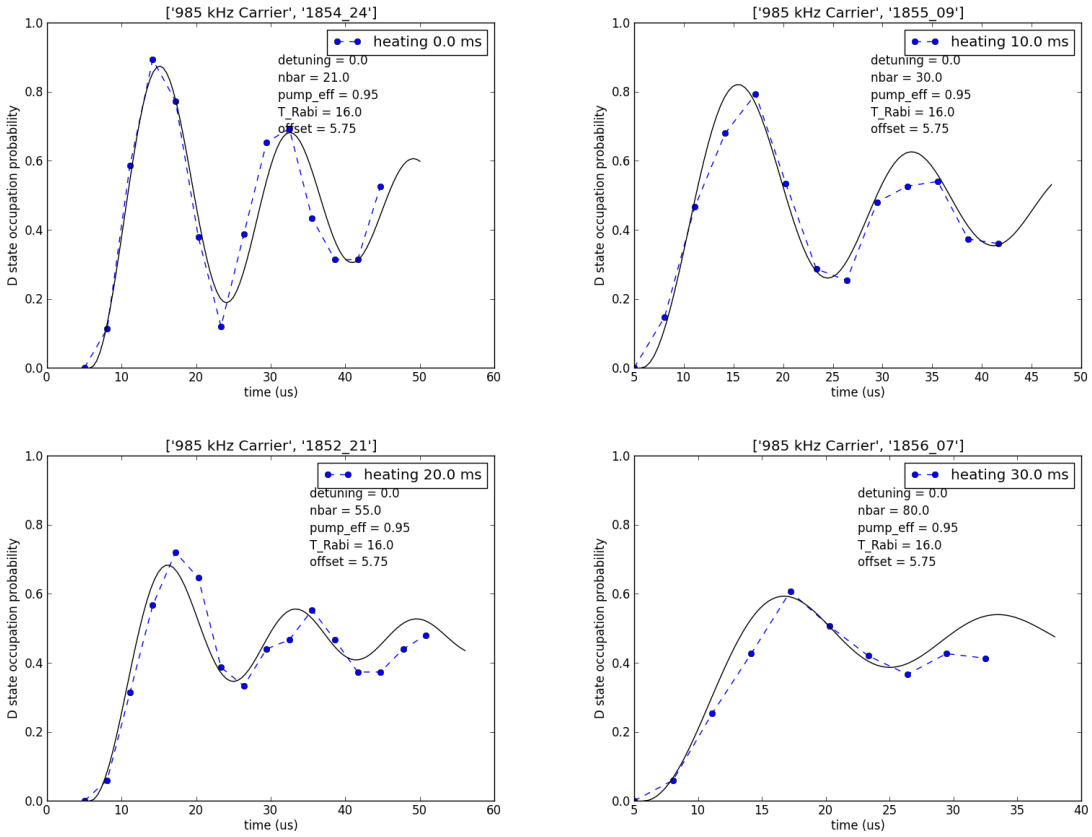

Figure 5.19: *Rabi oscillations for different heating times.* For longer waiting times, decoherence starts to kick in. 5-parameter fits to the evolution in solid color. Evolutions are differentiated by a change in phonons absorbed by the ion, thus increasing its energy

motion is caused by both, large number of randomly fluctuating sources, each scaling with source-ion separation as an electrical dipole field. The spectral density of this anomalous heating noise is expected to scale as 1/f with frequency. We can estimate the density of electrical dipole sources on trap electrode surfaces giving rise to the heating rates reported in the literature.

In order to measure heating rates, we use laser cooling (near resonant excitation of an atomic transition) methods to reduce the kinetic energy of the trapped ions. This is because, out of all methods available to cool a trapped ion, only laser cooling does it down to the quantum regime. Typically two limiting cases are treated since in the rest frame of the oscillating ion, the laser frequency appears frequency-modulated with the trap frequency. Also, the strength of the sidebands depend on the amplitude of the ionic motion.

The first of this two limiting cases applies when the trap frequency ω is small compared to the decay rate Γ of the atomic transition used for cooling, then the spacing of the sidebands is smaller than the absorption width of the transition, thus sidebands cannot be resolved.

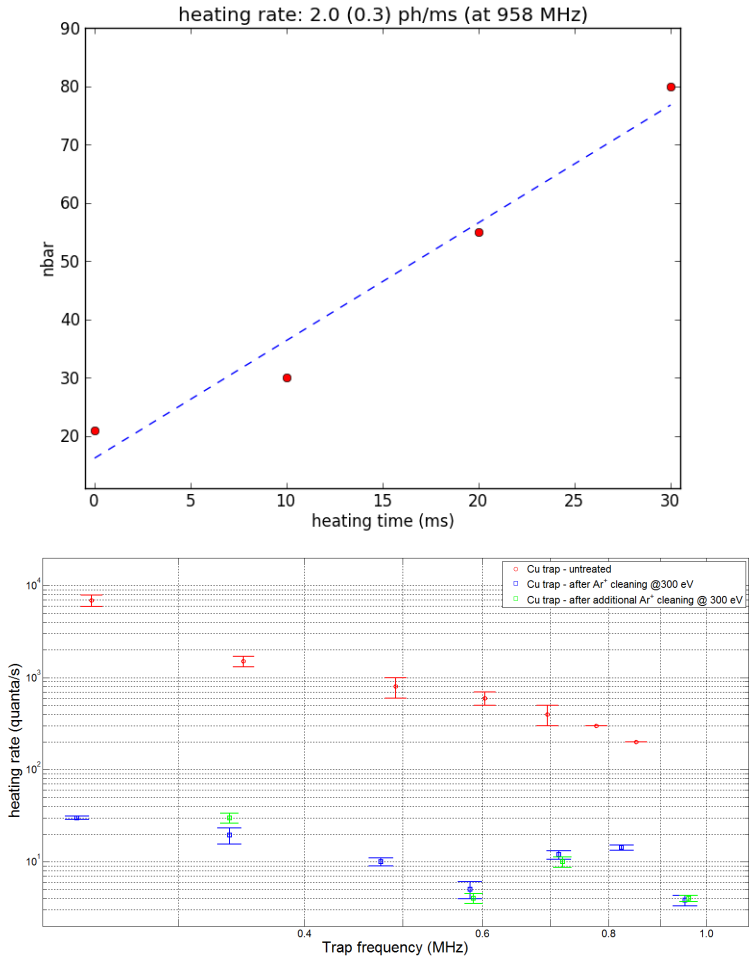

Figure 5.20: *Heating rates* A.) Extracted from the liner increase with heating time. Phonon number is extracted from the fits in the 4 previous figures. B.) Plot of heating rates in Copper trap before and after treatment with our cleaning methods. Cleaning methods improve heating rates

In this regime, the velocity of the ion changes slower compared to the atomic transitions of the atom (absorption and emission processes) so that we can assume that ion's momentum changes instantaneously. The trapped ion then behaves like a free-particle seeing a time-dependent Doppler-shifted laser frequency. This velocity-dependent radiation pressure provides the so called Doppler cooling. Heating rates are typically measured using Doppler cooling as is described in reference [410]. In this scheme, the motional energy of the ion is extracted from the increased Doppler shift on a trapped ion with increased kinetic energy, reflected as a change in its fluorescence. By allowing the ion to heat up when turning the Doppler cooling laser off during increasing waiting times τ_{OFF}, the record of changes in fluo-

rescence as the ion cools down after turning the Doppler cooling laser on allows to determine the energy taken by the ion while in τ_{OFF}, and extract the ion heating rate from there. This method is used in situations with negligible micromotion. If not so, Doppler broadening has to be taken into account to determine ion energy from changes in fluorescence and extract the micromotion contribution as done in [422]. One can avoid implicit assumptions by measuring heating rates for the three motional modes. Doppler cooling of atoms is very similar to Brownian motion and can be cast into the Fokker-Plank equation. The atom random-walks in momentum space with a linear drift and a constant diffusion coefficient, known as Ornstein-Uhlenbeck process. In stationary state, this momentum distribution has a Gaussian shape, thus a thermal distribution results from the energy level occupation.

The second limiting case applies when the trap frequency ω is large compared to the decay rate Γ of the atomic transition (and the laser linewidth), then the spacing of the sidebands is larger than the absorption width of the transition, thus sidebands can be resolved. In this regime, we can tune our laser to an specific band. If the energy of the absorbed photons is smaller than the mean energy of the spontaneously emitted photons (tune to the lower motional sideband of the transition), the kinetic energy of the ion shrinks since each excitation to an upper level is accompanied by a reduction in the vibrational quantum number. Depending on the experimental conditions, this cooling method is required as a second cooling step to complement Doppler cooling to prepare the ion in a pure state of motion [444]. In this scheme, the $S_{1/2} \leftrightarrow D_{5/2}$ transition is used for sideband cooling on a quadrupole transition. The natural lifetime of the $D_{5/2}$ level is approximately one second, therefore the upper level has to be quenched by coupling it to the quickly decaying $P_{3/2}$ level to have acceptable cooling rates. This quadrupole transition is split using magnetic field into ten different transitions. A three-level system can be approximated by choosing the $S_{1/2}(m = -1/2) \leftrightarrow D_{5/2}(m = -5/2)$ transition for sideband cooling and coupling the upper level to the $S_{1/2} \leftrightarrow P_{3/2}(m = -3/2)$ level.

Details on the combined use of these two cooling methods and its use in measuring heating rates is further discussed in reference [444]. We cool the ion to the Doppler limit on the $S_{1/2} \leftrightarrow P_{1/2}$ transition with a laser at 397 nm, using an additional laser at 866 nm to depopulate the metastable $D_{3/2}$ level. In addition, when the ion heating rate is below a few hundred quanta/s, we can reliably cool the ion close to the motional ground state doing sideband cooling on a quadrupole transition at 729 nm. High heating rate values are obtained with Doppler-cooled ions, and lower heating rate values with sideband-cooled ions.

We use spectroscopy on the $S_{1/2} \leftrightarrow D_{5/2}$ quadrupole transition to probe motional heating of the ion. A magnetic field of 2 G is applied perpendicular to the propagation direction and polarization of the 729 nm beam defines the quantization axis. An optical pumping pulse from the 729 nm laser prepares the ion in the $S_{1/2}(m = -1/2)$ state. All the lasers are then switched off for a certain duration, during which the ion heats up due to electric field noise at the ion. To probe the number of quanta acquired during this period, we drive Rabi flops between the $S_{1/2} \leftrightarrow D_{5/2}(m = -5/2)$ states. A fit to a model of the two level ion in a thermal state of motion interacting with the light field yields the average phonon occupation $\bar{n}$. By measuring $\bar{n}$ at different waiting times we extract the motional heating

rate $\bar{n}$. Alternatively, as noted above, for low heating rates, sideband cooling is used to drive the ion to its ground state of motion. The motional quanta is deduced by comparing the transition strengths of the red and blue sidebands as $\bar{n} = \frac{R}{R+1}$ where R is the ratio of the red to the blue sideband. By inserting a variable waiting time before each measurement of $\bar{n}$ we determine $\dot{\bar{n}}$.

Figure 5.19 displays the Rabi oscillations of the carrier frequency for 4 waiting times (0ms, 10ms, 20ms, 30ms) used to extract our heating rate measurement of an standard Gold trap fabricated using our methods. As we can see from the plots, as the waiting time increases decoherence effects start being noticeable. Initially, we measured the heating rates of the ion after trap installation and chamber bake-out. Figure 5.20b shows the heating rates obtained for 7 different axial frequencies, with heating rates in the quanta/s range. The frequency scaling of these heating rates is $\dot{\bar{n}} \sim f^{-2.57(0.2)}$. The noise spectral density corresponding to this trap is $S_E \approx (V/m)/\sqrt{Hz}$. When ploted as in figure 5.20, ion energy linear increase with heating time is observed as expected under the assumptions of the model such as negligible micromotion. This is one data point of the many we extracted on the same trap after several months of continuous work on filter boards, faraday cages, ground loops, signal integrity protection, cleaning and dirtying methods to study changes on the surface.

5.9 Argon cleaning and Auger electron Spectra (AES)

Particularly important is our further surface study by taking an AES of the surface before and after any surface treatment, detailing the exact composition of the surface. Figures and show the Auger spectrum of the trap surface, taken using 2 keV electrons. The dominant features are the carbon (LVV) and oxygen (KLL) peaks, while smaller peaks due to copper (KLL), and a small trace of aluminum (KLL) are visible.

In chapter 1 we mentioned that depth profile of a surface can be extracted by a combination of AES and sputtering as detailed in [144] [149]. The topography, as well as elemental composition information of the surface is important to correlate spatial and chemical data. For surface analytical purposes, Auger spectroscopy can be used to detect any element we have included in our fabrication steps, as well as any resulting from reaction at the surface or outgassing from the chamber walls (such as when baking). This can give us a clearer picture of how our processes change the surface and the environment. Low resolution is enough for our surface analysis since most elements we use are separated quite well in the spectrum.

Figures 5.21 and 5.22 display the Gold trap and Copper trap Auger spectra results, respectively, after typical surface treatment processes have been implemented on them. The starting condition of our trap is assumed clean, unless we sputter from it part of its substrate in order to trace well how our cleaning methods remove the intended species observed in previous AES readings.

As can be seen from the spectra, the Gold trap goes through 4 typical cleaning methods used in ion trapping and from which we are able to derive important conclusions. First, initial spectra (green) is taken after the initial bakeout is performed, in which high temperature

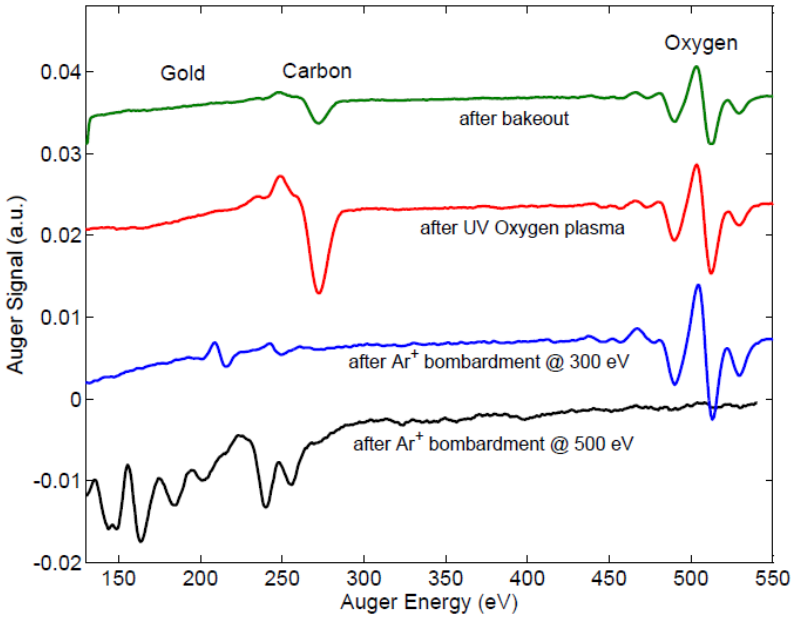

Figure 5.21: *Auger Electron Spectroscopy (AES) for Gold traps.* As observed, Carbon is the initial contaminant. Cleaning methods employed and subsequent surface residual compositions are pictured.

aids the removal organic materials from all walls through outgassing and further pumping. As we can see in the AES spectra Carbon is adsorbed by the gold surface and Gold is not a peak. Then after, we perform UV Oxygen plasma to clean the Carbon from the surface. The spectra taken indicates that there is an enhanced presence of oxygen in the chamber, Carbon removal is not efficient, and and seems to be forming carbon based compounds. To remove these, we emply Argon ion bombardement (sputtering) from which we extract the Gold peak, since its presence has been promoted by the bombardment. Also, we see there is even more Oxygen than before, hinting on the possible CO composition of those Carbon peaks. Further increase in Argon bombardment power removes the oxygen from the surface, but as well, it damages the surface, from which we extract a very complex composition based on Gold.

From this measurements on Gold, we are able to extract the main elements present in our surfaces. Carbon, as seen in the AES remains reactive and a big role player in typical cleaning methods. From this, we conclude a Graphene trap which has remains of Carbon on the surface (what we expect to have after CVD) will be extremely difficult to clean. The remaining Carbon on the surface will make impossible the trapping and the cleaning, since its removal without burning graphene will be extremely difficult.

In figure 5.22, AES spectra for our Cu-Al trap is shown. As mentioned, before annealing, the trap surface is mainly Copper, as is clearly shown by the AES spectra. In subsequent steps, see figure 5.20b and 5.22 we cleaned the trap using energetic Ar+ ions, and measured

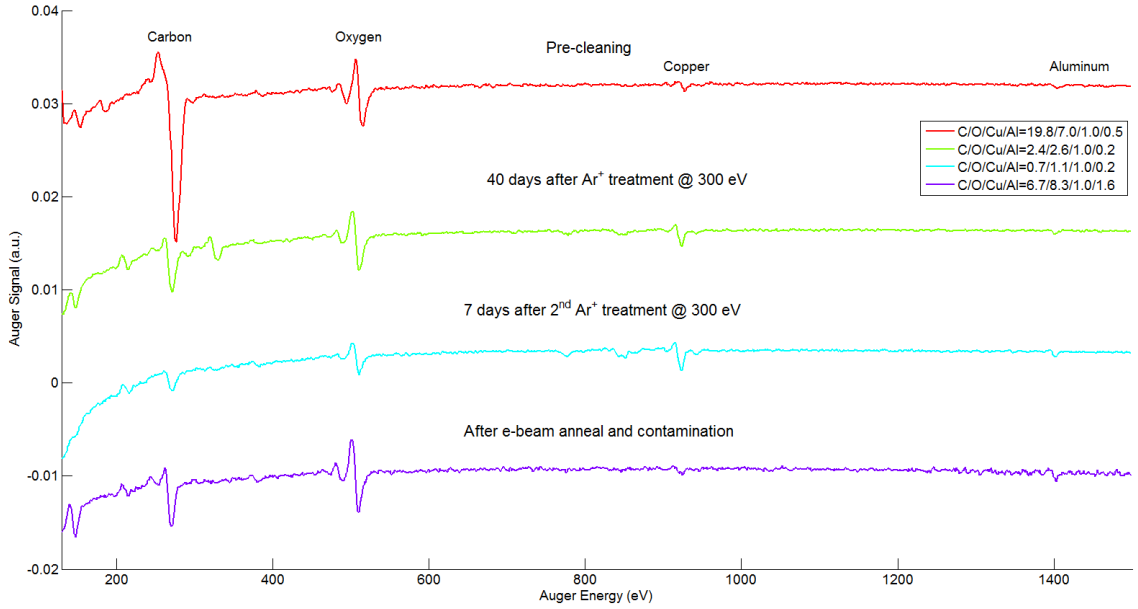

Figure 5.22: *Auger Electron Spectroscopy (AES) for Al-Cu traps.* Al-Cu traps, mainly a Cu trap as the surface composition clearly states. Cleaning methods employed and subsequent surface residual compositions are pictured.

heating rates, as well as Auger spectra from the trap surface. We performed heating rate measurements 2 days and 40 days after surface cleaning, and we recorded Auger spectra 7 days and 40 days after cleaning. In order to minimize the effect of contamination of the trap surface from the electron filament on the heating rates, we always recorded heating rates prior to collecting Auger spectra. The ion energy during cleaning was 300 eV, the angle of incidence was perpendicular to the trap surface, and the beam fluence was $xAr+/cm^2$ sec. We carried out one cleaning step for a total of few minutes, resulting in an estimated removal of few nm of material from the surface. The cleaning was followed by a 40 day wait, during which the trap was operated on a weekly basis. At the end the 40 days, we recorded the heating rate measurements shown in Fig. 5.20b and the Auger spectrum shown in Figure 5.22. This was followed by additional few min of Ar+ion cleaning (using same conditions as before), a heating rate measurement 2 days after cleaning, see Fig. 5.22, and a final Auger spectrum recorded 7 days after cleaning, see Fig. 5.22.

The cleaning resulted in a reduction of the ion heating rate by a factor between 15 and 200 compared to the uncleaned trap, and a change of the spectral characteristics of the noise in the frequency range 200 kHz to 1 MHz. The ion heating rates measured 2 days after cleaning the trap are consistent with the values measured 40 days after cleaning, despite the difference in carbon and oxygen content of the surface, seen in the Auger spectra. This indicates that copper surfaces do not need to be atomically clean to achieve the level of noise measured in our trap. The heating rates in the cleaned trap decrease with frequency for frequencies

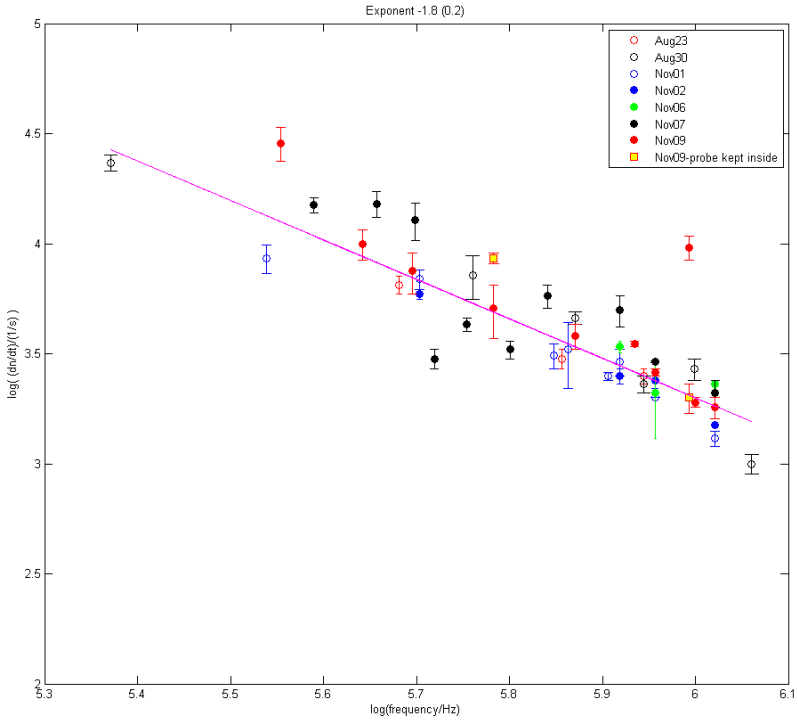

Figure 5.23: *Summary of heating rate measurements for Gold trap.* Heating rates as phonon/s versus working frequency. Our Gold traps fell well within the average trend, even after surface treatment methods.

between 200 kHz and 500 kHz, and at higher frequencies they show a broad maximum centered around 700 kHz. The initial drop-off with frequency has scaling $\dot{\bar{n}} \sim f^{-1.95(0.28)}$. The peak at higher frequencies is reminiscent of resonant behavior.

In figures 5.23 and 5.24, heating rates are presented as a rate of change of phonons per second of time. Scaled by the working frequency in a logarithmic scale to extract a linear relationship. All points in this figure are heating rate measurements on the Gold trap during the detailed dates. During a period of three months, the heating rate results did not change considerably, possibly due to noisy electronics of our DC electrodes. Our trap remained limited within the same region no matter what cleaning methods we used for the Gold trap.

It is instructive to compare the electric field noise measured in this work with noise measured on other traps. To take into account the generally observed spectral dependence of the noise $S_E \sim f^{-\alpha}$, with $\alpha \sim 1$, it is useful to plot the product ωS_E, where ω is the frequency at which the noise was measured. In Fig. 5.24 we summarize ωS_E versus the closest ion-electrode distance, for a number of trap noise measurements reported in the literature. To compare between ion traps with different dimensions, we scale the noise as

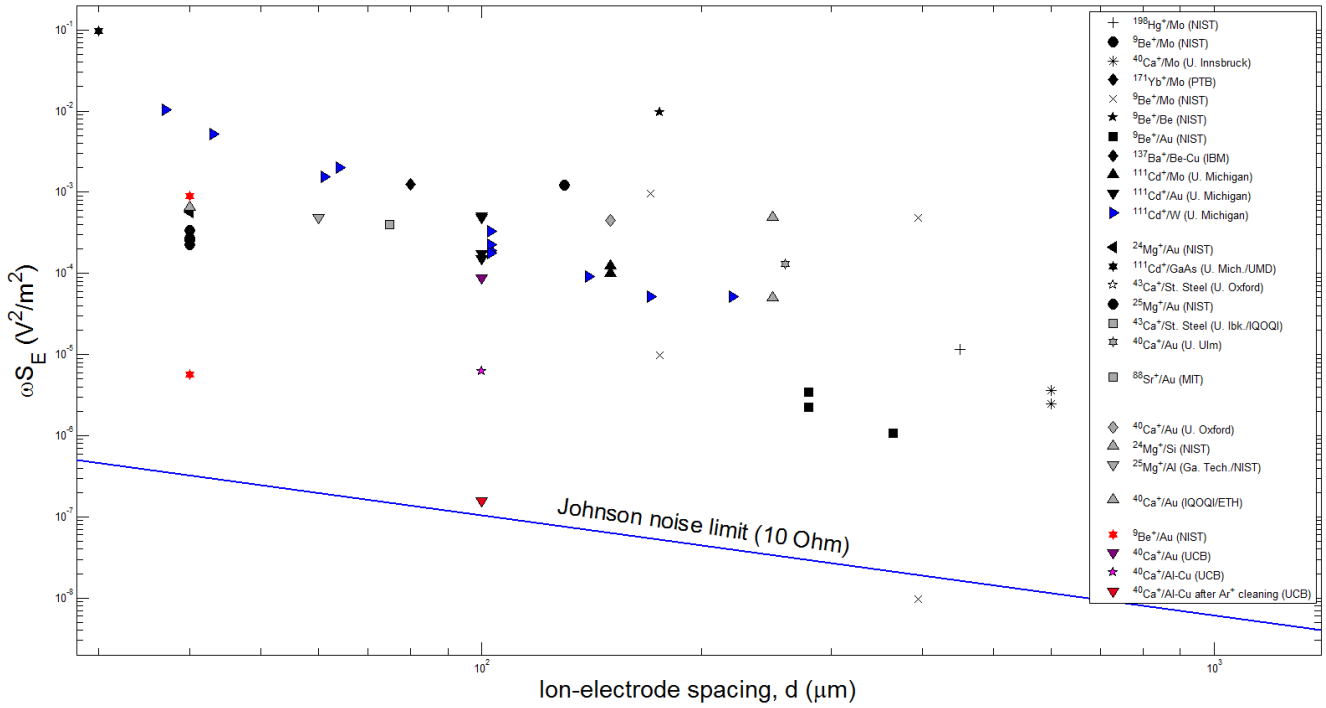

Figure 5.24: *Summary of heating rate measurements for our traps compared to the rest* Representative noise spectral densities for different traps found in the literature [422], plotted versus ion-trap distance d. The ion species, trap electrode material and Temperature (when different than room temperature) are specified. Our Gold traps fell well within the average trend, but the Cu-Al trap, after surface treatment methods falls in the limits of Johnson noise

$S_E \sim d^{-4}$, which is expected for noise arising from independently fluctuating electrical-dipole sources of anomalous heating from the surface. The exact scaling includes geometry dependent prefactors, but the d^{-4} law serves as an acceptable rough guide, and it allows for direct comparison between traps with a planar electrode geometry. $1/f$ noise is attributed to systems with a Debye-type relaxation, and a distribution of relaxation rates. Details on this please refer to reference [422]. By plotting in the same way all other noise spectral densities for traps found in the literature, plotted versus ion-trap distance d we can see that our noise values measured prior to surface cleaning of our trap are lower than those reported at room temperature for other traps with similar dimensions. Also, the noise values measured after surface cleaning are comparable to the lowest heating rates measured at cryogenic temperatures.

5.10 Conclusion

We have reviewed relevant information about fundamental mechanisms behind ion-traps. For a complete description please refer to [413] and [371]. Our review focus on the physics behind the Hamiltonians for quantization of motion and internal electronic states of the trapped ion. We associated ion interaction with EM fields, generated and detected with purposes of driving transitions that change in oscillation frequency according to the Energy discrete levels. The trapping potential is harmonic and ion motional states spectrum are treated similar to that of a multidimensional harmonic oscillator. We also have reviewed the possibility of performing single-qubit rotations and its visualization in the Bloch sphere.

Trapped ion experiments allow us to study the interaction with the trapping surface by measuring heating rates. Models explaining such sources of noise such as the "patch potential" have been reviewed to describe the dependance on ion-surface distance. Heating rates were measured for different surfaces (Gold, Cu-Al)

Our surface electrode geometry consisting of a metal thin film deposited on a previously patterned insulating substrate is a clean and promising candidate to achieve large scale quantum information processing due to the relatively easy procedure to fabricate and adjust its surface structural properties. Also, the cleanest trap achieved so far (lowest heating rates, and close to Johnson noise limit)

Electric field noise and charge noise are present in many other systems such as NEMS [429], single spin detectors [430], single electron transistors [432], Josephson qubits [433], superconducting coplanar resonators [434], [435] [436], and quantum dots [437] [438]. The trapping potential could be controlled so that we address the motional state-to-state transitions using electric fields of appropriate frequency, amplitude, duration, and phase so that the motion of ions could be controlled adiabatically. Thus, its evolution can be controlled using FPGA based electronic interfaces, and the system selectively addressing each ion should be very similar to the one presented in Chapter 4.

Bibliography

[350] Murray D Barrett et al. “Sympathetic cooling ofˆ{9} Beˆ{+} andˆ{24} Mgˆ{+} for quantum logic”. In: *Physical Review A* 68.4 (2003), p. 042302.

[351] PA Barton et al. “Measurement of the lifetime of the 3dˆ{2} D_ {5/2} state inˆ{40} Caˆ{+}”. In: *Physical Review A* 62.3 (2000), p. 032503.

[352] JC Bergquist et al. “Observation of quantum jumps in a single atom”. In: *Physical review letters* 57.14 (1986), pp. 1699–1702.

[353] DJ Berkeland and MG Boshier. “Destabilization of dark states and optical spectroscopy in Zeeman-degenerate atomic systems”. In: *Physical Review A* 65.3 (2002), p. 033413.

[354] BB Blinov et al. “Sympathetic cooling of trapped Cdˆ{+} isotopes”. In: *Physical Review A* 65.4 (2002), p. 040304.

[355] JJ Bollinger et al. “A 303-MHz frequency standard based on trapped Be¡ sup¿+¡/sup¿ ions”. In: *Precision Electromagnetic Measurements, 1990. CPEM’90 Digest., Conference on*. IEEE. 1990, pp. 264–265.

[356] CE Pearson et al. “Experimental investigation of planar ion traps”. In: *Physical Review A* 73.3 (2006), p. 032307.

[357] Claude Cohen-Tannoudji, Bernard Diu, and Frank Laloë. *Quantum Mechanics, 2 Volume Set*. 2006.

[358] Juan I Cirac and Peter Zoller. “Quantum computations with cold trapped ions”. In: *Physical review letters* 74.20 (1995), pp. 4091–4094.

[359] Richard J Cook. “V Quantum Jumps”. In: *Progress in optics* 28 (1990), pp. 361–416.

[360] DR Leibrandt et al. “Demonstration of a scalable, multiplexed ion trap for quantum information processing”. In: *Quantum Information & Computation* 9.11 (2009), pp. 901–919.

[361] DJ Wineland, Wayne M Itano, and RS Van Dyck Jr. “High-resolution spectroscopy of stored ions”. In: *Adv. At. Mol. Phys* 19.1 (1983), pp. 135–187.

[362] DTC Allcock et al. “Implementation of a symmetric surface-electrode ion trap with field compensation using a modulated Raman effect”. In: *New Journal of Physics* 12.5 (2010), p. 053026.

[363] HG Dehmelt. "Radiofrequency spectroscopy of stored ions I: Storage". In: *Adv. Atom. Mol. Phys* 3 (1967), pp. 53–72.

[364] HG Dehmelt. "Radiofrequency spectroscopy of stored ions II: Spectroscopy". In: *Adv. At. Mol. Phys* 5 (1969), p. 109.

[365] B DeMarco et al. "Experimental demonstration of a controlled-NOT wave-packet gate". In: *Physical review letters* 89.26 (2002), p. 267901.

[366] Louis Deslauriers et al. "Scaling and suppression of anomalous heating in ion traps". In: *Physical review letters* 97.10 (2006), p. 103007.

[367] F Diedrich et al. "Observation of a phase transition of stored laser-cooled ions". In: *Physical review letters* 59.26 (1987), pp. 2931–2934.

[368] RJ Epstein et al. "Simplified motional heating rate measurements of trapped ions". In: *Physical Review A* 76.3 (2007), p. 033411.

[369] Pradip K Ghosh. *Ion traps*. Clarendon press Oxford, 1995.

[370] GR Guthöhrlein et al. "A single ion as a nanoscopic probe of an optical field". In: *Nature* 414.6859 (2001), pp. 49–51.

[371] Hartmut Häffner, Christian F Roos, and Rainer Blatt. "Quantum computing with trapped ions". In: *Physics Reports* 469.4 (2008), pp. 155–203.

[372] H Häffner et al. "Double Penning trap technique for precise g factor determinations in highly charged ions". In: *The European Physical Journal D-Atomic, Molecular, Optical and Plasma Physics* 22.2 (2003), pp. 163–182.

[373] JP Home et al. "Deterministic entanglement and tomography of ion–spin qubits". In: *New Journal of Physics* 8.9 (2006), p. 188.

[374] L Hornekær et al. "Structural properties of two-component Coulomb crystals in linear Paul traps". In: *Physical review letters* 86.10 (2001), pp. 1994–1997.

[375] Wayne M Itano and DJ Wineland. "Laser cooling of ions stored in harmonic and Penning traps". In: *Physical Review A* 25.1 (1982), p. 35.

[376] J Britton et al. "A microfabricated surface-electrode ion trap in silicon". In: *arXiv preprint quant-ph/0605170* (2006).

[377] Jaroslaw Labaziewicz et al. "Suppression of heating rates in cryogenic surface-electrode ion traps". In: *Physical review letters* 100.1 (2008), p. 013001.

[378] J Chiaverini et al. "Surface-electrode architecture for ion-trap quantum information processing". In: *arXiv preprint quant-ph/0501147* (2005).

[379] Jürgen Drees and W Paul. "Beschleunigung von Elektronen in einem Plasmabetatron". In: *Zeitschrift für Physik* 180.4 (1964), pp. 340–361.

[380] JI Cirac et al. "Laser cooling of trapped ions: The influence of micromotion". In: *Physical Review A* 49.1 (1994), p. 421.

[381] JM Amini et al. "Scalable ion traps for quantum information processing". In: *arXiv preprint arXiv:0909.2464* (2009).

[382] David Kielpinski. "Entanglement and decoherence in a trapped-ion quantum register". PhD thesis. University of Colorado, 2001.

[383] David Kielpinski, Chris Monroe, and David J Wineland. "Architecture for a large-scale ion-trap quantum computer". In: *Nature* 417.6890 (2002), pp. 709–711.

[384] Niels Kjærgaard et al. "Isotope selective loading of an ion trap using resonance-enhanced two-photon ionization". In: *Applied Physics B* 71.2 (2000), pp. 207–210.

[385] Jaroslaw Labaziewicz et al. "Temperature dependence of electric field noise above gold surfaces". In: *Physical review letters* 101.18 (2008), p. 180602.

[386] D Leibfried et al. "Quantum dynamics of single trapped ions". In: *Reviews of Modern Physics* 75.1 (2003), p. 281.

[387] Dietrich Leibfried et al. "Experimental demonstration of a robust, high-fidelity geometric two ion-qubit phase gate". In: *Nature* 422.6930 (2003), pp. 412–415.

[388] D Leibfried et al. "Trapped-ion quantum simulator: experimental application to nonlinear interferometers". In: *Physical review letters* 89.24 (2002), p. 247901.

[389] N Daniilidis et al. "Wiring up trapped ions to study aspects of quantum information". In: *Journal of Physics B: Atomic, Molecular and Optical Physics* 42.15 (2009), p. 154012.

[390] G Littich. "Electrostatic Control and Transport of Ions on a Planar Trap for Quantum Information Processing". PhD thesis. University of California, Berkeley, 2011.

[391] Chris Monroe et al. "Demonstration of a fundamental quantum logic gate". In: *Physical Review Letters* 75.25 (1995), pp. 4714–4717.

[392] HC Nägerl et al. "Ion strings for quantum gates". In: *Applied Physics B: Lasers and Optics* 66.5 (1998), pp. 603–608.

[393] Warren Nagourney, Jon Sandberg, and Hans Dehmelt. "Shelved optical electron amplifier: Observation of quantum jumps". In: *Physical Review Letters* 56.26 (1986), pp. 2797–2799.

[394] JD Prestage, Go J Dick, and L Maleki. "New ion trap for frequency standard applications". In: *Journal of Applied Physics* 66.3 (1989), pp. 1013–1017.

[395] R Blatt and P Zoller. "Quantum jumps in atomic systems". In: *European Journal of Physics* 9.4 (1988), p. 250.

[396] Rainer Blatt and David Wineland. "Entangled states of trapped atomic ions". In: *Nature* 453.7198 (2008), pp. 1008–1015.

[397] Richard P Feynman, Frank L Vernon, and Robert W Hellwarth. "Geometrical representation of the Schrödinger equation for solving maser problems". In: *Journal of Applied Physics* 28.1 (1957), pp. 49–52.

[398] MG Raizen et al. "Ionic crystals in a linear Paul trap". In: *Physical Review A* 45.9 (1992), p. 6493.

[399] MG Raizen et al. "Linear trap for high-accuracy spectroscopy of stored ions". In: *Journal of Modern Optics* 39.2 (1992), pp. 233–242.

[400] Harald Rohde et al. "Sympathetic ground-state cooling and coherent manipulation with two-ion crystals". In: *Journal of Optics B: Quantum and Semiclassical Optics* 3.1 (2001), S34.

[401] MA Rowe et al. "Transport of quantum states and separation of ions in a dual rf ion trap". In: *arXiv preprint quant-ph/0205094* (2002).

[402] Signe Seidelin et al. "Microfabricated surface-electrode ion trap for scalable quantum information processing". In: *Physical review letters* 96.25 (2006), p. 253003.

[403] Marek Šašura and Vladimir Bužek. "Cold trapped ions as quantum information processors". In: *journal of modern optics* 49.10 (2002), pp. 1593–1647.

[404] CA Sackett et al. "Experimental entanglement of four particles". In: *Nature* 404.6775 (2000), pp. 256–259.

[405] Th Sauter et al. "Observation of quantum jumps". In: *Physical review letters* 57.14 (1986), pp. 1696–1698.

[406] CA Schrama et al. "Novel miniature ion traps". In: *Optics communications* 101.1 (1993), pp. 32–36.

[407] RC Thompson. "Spectroscopy of trapped ions". In: *Adv. Atom. Molec. Opt. Phys* 31 (1993), p. 63.

[408] QA Turchette et al. "Heating of trapped ions from the quantum ground state". In: *Physical Review A* 61.6 (2000), p. 063418.

[409] MI Dyakonov. "State of the art and prospects for quantum computing". In: *arXiv preprint arXiv:1212.3562* (2012).

[410] JH Wesenberg et al. "Fluorescence during Doppler cooling of a single trapped atom". In: *Physical Review A* 76.5 (2007), p. 053416.

[411] DJ Wineland et al. "Double-resonance and optical-pumping experiments on electromagnetically confined, laser-cooled ions". In: *Optics letters* 5.6 (1980), pp. 245–247.

[412] David J Wineland et al. "Atomic-ion Coulomb clusters in an ion trap". In: *Physical review letters* 59.26 (1987), pp. 2935–2938.

[413] David J Wineland et al. "Experimental issues in coherent quantum-state manipulation of trapped atomic ions". In: *arXiv preprint quant-ph/9710025* (1997).

[414] DJ Wineland and HG Dehmelt. "Principles of the stored ion calorimeter". In: *Journal of Applied Physics* 46.2 (1975), pp. 919–930.

[415] Kirt R Williams, Kishan Gupta, and Matthew Wasilik. "Etch rates for micromachining processing-Part II". In: *Microelectromechanical Systems, Journal of* 12.6 (2003), pp. 761–778.

[416] K Kolari. "High etch selectivity for plasma etching SiO¡ sub¿ 2¡/sub¿ with AlN and Al¡ sub¿ 2¡/sub¿ O¡ sub¿ 3¡/sub¿ masks". In: *Microelectronic Engineering* 85.5 (2008), pp. 985–987.

[417] H Moriceau et al. "Overview of recent direct wafer bonding advances and applications". In: *Advances in Natural Sciences: Nanoscience and Nanotechnology* 1.4 (2010), p. 043004.

[418] C Cohen-Tannoudji and B Diu. *Laloë (1977) Quantum Mechanics*.

[419] Michael A Nielsen and Isaac L Chuang. *Quantum computation and quantum information*. Cambridge university press, 2010.

[420] EA Donley et al. "Double-pass acousto-optic modulator system". In: *Review of Scientific Instruments* 76.6 (2005), pp. 063112–063112.

[421] Carsten Henkel, Sierk Pötting, and Martin Wilkens. "Loss and heating of particles in small and noisy traps". In: *Applied Physics B* 69.5-6 (1999), pp. 379–387.

[422] N Daniilidis et al. "Fabrication and heating rate study of microscopic surface electrode ion traps". In: *New Journal of Physics* 13.1 (2011), p. 013032.

[423] A Gangulee and FM d'Heurle. "Anomalous large grains in alloyed aluminum thin films I. Secondary grain growth in aluminum-copper films". In: *Thin solid films* 12.2 (1972), pp. 399–402.

[424] A Gangulee and FM d'Heurle. "Anomalous large grains in alloyed aluminum thin films II. Electromigration and diffusion in thin films with very large grains". In: *Thin Solid Films* 16.2 (1973), pp. 227–236.

[425] N Tamura et al. "Submicron x-ray diffraction and its applications to problems in materials and environmental science". In: *Review of scientific instruments* 73.3 (2002), pp. 1369–1372.

[426] Ariel Ismach et al. "Direct chemical vapor deposition of graphene on dielectric surfaces". In: *Nano letters* 10.5 (2010), pp. 1542–1548.

[427] Byung Jin Kang et al. "Monolayer graphene growth on sputtered thin film platinum". In: *Journal of Applied Physics* 106.10 (2009), pp. 104309–104309.

[428] Alexander Shnirman et al. "Low-and high-frequency noise from coherent two-level systems". In: *Physical review letters* 94.12 (2005), p. 127002.

[429] Mo Li, Hong X Tang, and Michael L Roukes. "Ultra-sensitive NEMS-based cantilevers for sensing, scanned probe and very high-frequency applications". In: *Nature nanotechnology* 2.2 (2007), pp. 114–120.

[430] HJ Mamin et al. "Detection and manipulation of statistical polarization in small spin ensembles". In: *Physical Review Letters* 91.20 (2003), p. 207604.

[431] CC Speake and C Trenkel. "Forces between conducting surfaces due to spatial variations of surface potential". In: *Physical review letters* 90.16 (2003), p. 160403.

[432] G Zimmerli et al. "Noise in the Coulomb blockade electrometer". In: *Applied physics letters* 61.2 (1992), pp. 237–239.

[433] O Astafiev et al. "Quantum noise in the Josephson charge qubit". In: *Physical review letters* 93.26 (2004), p. 267007.

[434] Jiansong Gao et al. "Experimental evidence for a surface distribution of two-level systems in superconducting lithographed microwave resonators". In: *Applied Physics Letters* 92.15 (2008), pp. 152505–152505.

[435] Shwetank Kumar et al. "Temperature dependence of the frequency and noise of superconducting coplanar waveguide resonators". In: *Applied Physics Letters* 92.12 (2008), pp. 123503–123503.

[436] Aaron D OConnell et al. "Microwave dielectric loss at single photon energies and millikelvin temperatures". In: *Applied Physics Letters* 92.11 (2008), pp. 112903–112903.

[437] Toshiki Hayashi et al. "Coherent manipulation of electronic states in a double quantum dot". In: *Physical review letters* 91.22 (2003), p. 226804.

[438] J Gorman, DG Hasko, and DA Williams. "Charge-qubit operation of an isolated double quantum dot". In: *Physical review letters* 95.9 (2005), p. 090502.

[439] DM Lucas et al. "Isotope-selective photoionization for calcium ion trapping". In: *Physical Review A* 69.1 (2004), p. 012711.

[440] Desmond Kay and Vernon Ellis Cosslett. *Techniques for electron microscopy*. Blackwell Scientific Publications Oxford, 1965.

[441] RWP Drever et al. "Laser phase and frequency stabilization using an optical resonator". In: *Applied Physics B* 31.2 (1983), pp. 97–105.

[442] Hans G Dehmelt. "Proposed 1014$\delta\nu$¡ ν laser fluorescence spectroscopy on Tl+ monoion oscillator II (spontaneous quantum jumps)". In: *Bull. Am. Phys. Soc* 20 (1975), p. 60.

[443] H. Haeffner. "Ion trap quantum computing". In:

[444] Christian Roos. "Controlling the quantum state of trapped ions". In: (2000).

Chapter 6

Conclusion and Perspectives

Sub-wavelength light-matter interactions uses of surface science and engineering to create novel ways to experience and explain it. In this text, each chapter written was related to a totally different area with respect to the rest, local conclusions were based on very narrow scopes but related through the use of the same fundamental relationships, available mathematical tools used to describe them.

The main lesson learned is that for optical an infrared frequencies, nanostructure design of the interfaces plays a role in modifying coupling between neighboring films as we reduce thickness dimensions down to the 2D for flat surfaces. Effective responses, different from conventional add a different flavor given the reduction in thickness, allowing us to treat surfaces down to a 1-atom thick surface or interface as another material, different from its bulk or thin film relative. Possible tuning of electronic conditions allows for real time control of electronic boundaries and such as in each of the cases treated was feasible for high frequencies due the reduced impedance, directly related to the permittivity of the metal, as explained in the introductory chapter and possibly tuned with metamaterials. Not only light will play a role in nanophotonic integration but as we keep playing with the structure of interfaces it travels through, will continue to reveal unexpected aspects of its nature.

To complete the experience, Id like to review current reported research in order to try to make further connections among the research addressed here in order to allow for a perspective of the field in the near future. As described in Chapter 2 coupling efficiency was a challenge due to polarization sensitivity and control on the directionality of the SPPs in waveguides. In reference [445] polarized surface plasmons are generated in the direction uniquely defined by the polarization type of the incident light. Near-field interference allows for unidirectional surface plasmon propagation. The surface wave direction can be switched with polarization, resulting in the near field unidirectional excitation of guided electromagnetic modes. Polarization-controlled tunable directional coupling with polarization-invariant total conversion efficiency and preservation of incident polarization applied to radially convergent and divergent circular structures supporting SPPs [446].

With Metamaterials it is possible to design the interplay between spatial and temporal medium responses (important in the scattering response). As known, wavelength λ and

frequency f, are related via the phase velocity v, $v = f\lambda$. Near-zero relative permittivity metamaterials are called Epsilon-Near-Zero (ENZ) metamaterials [447]. Since ϵ and μ can be tuned by design, a relaxed dependance linking frequency and wavelength could allow for high frequencies with long wavelengths. Supercoupling is possible, as wave in one waveguide efficiently tunnel through an ENZ-spacer to another waveguide, regardless channel's characteristics and relative orientation among waveguides. The narrower the channel's height, the better the tunneling. Because of this intensity enhancement over an extended region, this effect has been used for nonlinear effects [448] and emitters embedded in ENZ structures [449] [450], acoustic and matter waves [451], shielding the displacement current [452] [453]. Since the wavelength is increased in ENZ media, random fluctuations of embedded scatterers may lead to decreased incoherence. Near zero refractive index; however, preserved wave impedance [454] [455] [456].

Despite decoherence gained due to collisions, electrons making up the plasmon wave carry the quantum bit which was encoded in the photon [457]. This nonclassical information survives the multiple conversion and can be recovered [458]. It is only matter of time for plasmons to play a role in nanoscale quantum information processing.

New metamaterials will pose novel quantum experiments, either by inserting artificial atoms into periodic nanostructures or localizing real atoms into artificial periodic lattices for new ways for collective light-matter behavior in which fundamental aspects related to quantum fluctuations could reveal the existence of non-trivial collective phenomena resulting from hybridization of internal and global states [459]. Quantum metamaterials as an artificial optical medium could be designed to maintain global quantum coherence over times longer than the traversal time of an electromagnetic signal and quantum states of can be externally controlled (quantum control). Possible realizations of a 3D quantum metamaterial based on a network on current-biased Josephson junctions (phase qubits) as studied [460].

Bibliography

[445] Francisco J. Rodrguez-Fortuo et al. "Near-Field Interference for the Unidirectional Excitation of Electromagnetic Guided Modes". In: *Science* 340.6130 (2013), pp. 328–330.

[446] Jiao Lin et al. "Polarization-Controlled Tunable Directional Coupling of Surface Plasmon Polaritons". In: *Science* 340.6130 (2013), pp. 331–334.

[447] Mário Silveirinha and Nader Engheta. "Tunneling of Electromagnetic Energy through Subwavelength Channels and Bends using epsilon-Near-Zero Materials". In: *Phys. Rev. Lett.* 97 (2006), p. 157403.

[448] Igor I. Smolyaninov et al. "Anisotropic Metamaterials Emulated by Tapered Waveguides: Application to Optical Cloaking". In: *Phys. Rev. Lett.* 102 (2009), p. 213901.

[449] Andrea Alù and Nader Engheta. "Boosting Molecular Fluorescence with a Plasmonic Nanolauncher". In: *Phys. Rev. Lett.* 103 (2009), p. 043902. URL: http://link.aps.org/doi/10.1103/PhysRevLett.103.043902.

[450] Ernst Jan R. Vesseur et al. "Experimental Verification of n=0 Structures for Visible Light". In: *Phys. Rev. Lett.* 110 (2013), p. 013902. URL: http://link.aps.org/doi/10.1103/PhysRevLett.110.013902.

[451] Romain Fleury and Andrea Alù. "Exotic properties and potential applications of quantum metamaterials". In: *Applied Physics A* 109.4 (2012), pp. 781–788.

[452] Andrea Alù and Nader Engheta. "All Optical Metamaterial Circuit Board at the Nanoscale". In: *Phys. Rev. Lett.* 103 (2009), p. 143902. URL: http://link.aps.org/doi/10.1103/PhysRevLett.103.143902.

[453] Brian Edwards and Nader Engheta. "Experimental Verification of Displacement-Current Conduits in Metamaterials-Inspired Optical Circuitry". In: *Phys. Rev. Lett.* 108 (2012), p. 193902. URL: http://link.aps.org/doi/10.1103/PhysRevLett.108.193902.

[454] Richard W. Ziolkowski. "Propagation in and scattering from a matched metamaterial having a zero index of refraction". In: *Phys. Rev. E* 70 (2004), p. 046608. URL: http://link.aps.org/doi/10.1103/PhysRevE.70.046608.

[455] Natalia M. Litchinitser et al. "Metamaterials: electromagnetic enhancement at zero-index transition". In: *Opt. Lett.* 33.20 (2008), pp. 2350–2352.

[456] Xueqin Huang et al. "Dirac cones induced by accidental degeneracy in photonic crystals and zero-refractive-index materials". In: *Nature materials* 10.8 (2011), pp. 582–586.

[457] E Altewischer, MP Van Exter, and JP Woerdman. "Plasmon-assisted transmission of entangled photons". In: *Nature* 418.6895 (2002), pp. 304–306.

[458] Alexander Huck et al. "Demonstration of quadrature-squeezed surface plasmons in a gold waveguide". In: *Physical review letters* 102.24 (2009).